
Conductance Anomalies in Quantum Point Contacts Functional Renormalization Group applied to a 2D Hubbard Model

Nikolai Ufer



München 2011

**Conductance Anomalies in Quantum
Point Contacts
Functional Renormalization Group
applied to a 2D Hubbard Model**

Nikolai Ufer

Diplomarbeit
an der Fakultät für Physik
der Ludwig-Maximilians-Universität
München

vorgelegt von
Nikolai Ufer
aus Nagold

München, den 16.5.2011

Erstgutachter: Prof. J. von Delft

Zweitgutachter: Prof. U. Schollwöck

Contents

1	Introduction	1
2	Functional renormalization group (fRG)	3
2.1	Introduction	3
2.2	Many-particle Green functions	4
2.2.1	Green functions - generating functionals	5
2.2.2	Dyson equation and self-energy	6
2.3	Functional renormalization group approach	8
2.3.1	General proceeding	8
2.3.2	fRG flow equations	9
2.4	Specification of the truncation and the cutoff	14
2.4.1	Truncation scheme	14
2.4.2	Cutoff insertion	16
2.4.3	Resulting flow equations	16
2.4.4	Modified initial conditions	17
2.5	Alternative RG schemes	18
3	fRG applied to a 2D Hubbard model	21
3.1	Introduction	21
3.2	2D Hubbard model	22
3.2.1	Method of finite differences	23
3.2.2	2D Hubbard model Hamiltonian	23
3.2.3	Green function of the contact - projection method	26
3.2.4	Infinite tight-binding chain	34
3.3	fRG flow equations	38
3.3.1	Resulting fRG flow equations	39
3.3.2	Efficient Computation of certain elements of the Green function	41
3.4	Physical observables	45
3.4.1	Computation of the conductance	46
3.4.2	Spin-resolved local density	55

4	Quantum point contacts	59
4.1	Introduction	59
4.2	Experimental setup	60
4.3	Conductance quantization	61
4.3.1	Adiabatic transport model	62
4.3.2	Saddle point model of the constriction	63
4.3.3	Magnetic field dependence	65
4.3.4	Temperature dependence	65
4.4	Conductance Anomalies	66
4.4.1	Experimental Observations	66
4.4.2	Higher conductance plateaus	69
4.4.3	Microscopic models	71
5	fRG studies of quantum point contacts	75
5.1	Introduction	75
5.2	Modelling a quantum point contact	76
5.3	Energy scale h_*	78
5.3.1	Non-interacting model	80
5.3.2	Nearest neighbour vertex flow	81
5.3.3	On-site vertex flow	88
5.3.4	Comparison on-site/nearest neighbour vertex flow	91
5.4	Two-dimensional system	95
6	Conclusion and outlook	103
A	Calculation details to the projected Green functions	107
B	Calculation details to the surface Green function \tilde{g}	109
C	Calculation details to the spectral function of a 2D tight-binding chain	111
D	Recursive Green function algorithm	113
	Acknowledgements	124

List of Figures

2.1	Graphical representation of the fRG flow equations for the self-energy Σ^Λ , the two-particle vertex γ_2^Λ and the three-particle vertex function γ_3^Λ [2].	12
2.2	Illustration of the sharp cutoff function $C^\Lambda(iw_n) = \Theta(w_n - \Lambda)$ and the direction of the fRG flow.	16
3.1	Illustration of the 2D Hubbard model.	24
3.2	Retarded and advanced Surface Green functions versus energy over half-bandwidth 2τ for a 1D semi-infinite chain.	31
3.3	Retarded and advanced surface Green functions versus energy over half-subbandwidth 2τ for a 2D semi-infinite chain.	32
3.4	Density of states versus energy over half-bandwidth 2τ for a 1D infinite tight-binding chain.	35
3.5	Normalized density of states versus energy over half-subbandwidth $2\tau_x$ for a 2D infinite tight-binding chain.	36
3.6	Normalized density of states as a function of energy over 1D half-bandwidth 2τ and transversal position n for an infinite tight-binding chain with a smooth potential applied to the contact region, compare [3].	38
3.7	Matrix structure of $(\tilde{\mathcal{G}}^\Lambda)^{-1}$, $H_{contact}^0 + \Sigma_{leads}$, for a one- and two-dimensional system.	42
3.8	Comparison of the running time of the FIND and RGF algorithms, where the width is fixed and the length is varied, taken from [27].	45
3.9	Diagrammatical representation of the two contributions $\Pi^{(a)}$ and $\Pi^{(b)}$ to the current-current correlation function $\Pi_{RL}(iq_n)$, compare [13].	49
3.10	Parted contour used for the Matsubara frequency summation in equation (3.98), compare [7].	51
4.1	Schematic cross-section of a split gate geometry modelling a QPC, taken from [52].	60
4.2	Point-contact conductance as a function of the gate voltage measured by van Wees et al. [53].	61
4.3	Influence of the ratio w_y/w_x on the linear conductance of a non-interacting saddle-point model, taken from [9].	64

4.4	Temperature and magnetic field dependence of the 0.7 anomaly, taken from [49].	66
4.5	Influence of the electron density of the 2DEG on the 0.7 anomaly, taken from [48].	67
4.6	Influence of a perpendicular magnetic field on the conductance and differential conductance of a hole QPC, taken from [24].	68
4.7	Energy splittings as a function of the magnetic field, taken from [26]	69
4.8	Transconductance traces and linear conductance as a function of the gate voltage, measured by Thomas et al. and taken from [48]	70
4.9	Linear conductance and transconductance traces as a function of the gate voltage, taken from [25].	71
4.10	Results of the conductance for the Kondo-related model of Meir et al., taken from [34].	72
4.11	Illustration of the momentum-non-conserving e-e scattering processes, taken from Lunde et al. [29].	73
5.1	Zero temperature linear conduction and shot noise obtained with the fRG approach, taken from [3].	76
5.2	Illustration of the one-dimensional potential barrier V_n^x for various potential heights and curvatures.	77
5.3	Illustration of the saddle point potential V^{sp} for different potential heights.	77
5.4	Energy scale h_* and conductance as a function of the potential height \tilde{V}_g	79
5.5	Magnetic field range of the well-definedness of the energy scale h_*	80
5.6	Energy scale h_* for a saddle-point constriction model in a non-interacting systems.	81
5.7	Three-dimensional graph of $\log(h_*/\tau)$ as a function of the potential height and the interaction for data generated with the fRG approach including nearest neighbour vertex flow [3] and $U' = U/10$	82
5.8	Three-dimensional graph of $\log(h_*/\tau)$ as a function of the potential height and the curvature for data generated with the fRG approach including nearest neighbour vertex flow [3] and $U' = U/10$	83
5.9	Analysis of the exponential growth $\exp(-f_1 V_g)$ for data generated with the fRG approach including nearest neighbour vertex flow [3] and $U' = U/10$	84
5.10	Analysis of the exponential growth $\exp(-f_2 \tilde{V}_g)$ for data generated with the fRG approach including nearest neighbour vertex flow [3] and $U' = U/10$	85
5.11	Analysis of the absolute value $h_*^{0.5G_0}$ for data generated with the fRG approach including nearest neighbour vertex flow [3] and $U' = U/10$	86
5.12	Analysis of the minimum h_*^{min} for data generated with the fRG approach including nearest neighbour vertex flow [3] and $U' = U/10$	87
5.13	Three-dimensional graph of $\log(h_*/\tau)$ as a function of the potential height and the interaction for data generated with the fRG approach including on-site vertex flow.	90

5.14	Three-dimensional graph of $\log(h_*/\tau)$ as a function $\Delta\tilde{V}_g/w$ and curvature for data generated with the fRG approach including on-site vertex flow. . .	90
5.15	Analysis of the exponential growth $\exp(-f_1\tilde{V}_g)$ for data generated with the fRG approach including on-site vertex flow.	92
5.16	Analysis of the exponential growth $\exp(-f_2\tilde{V}_g)$ for data generated with the fRG approach including on-site vertex flow.	92
5.17	Analysis of the absolute value $h_*^{0.5G_0}$ for data generated with the fRG approach including on-site vertex flow.	93
5.18	Analysis of the minimum h_*^{min} for data generated with the fRG approach including on-site vertex flow.	93
5.19	Comparison of the conductance and energy scale h_* between data generated with fRG including on-site and nearest neighbour vertex flow.	94
5.20	Three-dimensional graph of $\log(h_*/\tau)$ as a function of the potential height relative to $\tilde{V}_g^{0.5G_0}$ and the nearest-neighbour interaction U'	95
5.21	Influence of the potential curvatures and interaction strength on the first three conductance steps.	97
5.22	Influence of the interaction on the conductance and differential conductance $dG/d\tilde{V}_g$ for the first three conductance plateaus.	98
5.23	Effective g-factor for the first three submodes as a function of the interaction U and three different transversal confinements.	99
5.24	Comparison of the magnetic field behaviour of the conductance for the first three conductance plateaus.	101
5.25	Comparison of the magnetic field behaviour of the conductance for the first three conductance plateaus where the pinch-off region is rescaled for each mode.	102

List of Tables

5.1	Eigenenergies in terms of our energy scale and the scalar product of the component-wise squared eigenstates of a transversal confinement potential (5.2) at the center of the potential barrier for $w_y = 0.0, 0.5$ and 1.0τ	96
-----	--	----

Chapter 1

Introduction

The topic of this thesis is "the conduction anomalies in quantum point contacts" which can be assigned to the field of quantum transport. This branch of physics deals with the transport properties that can't be explained by classical physics and that are independent of the specific atomic structure. Previously, most of this research branch was attributed to mesoscopic physics which deals with quantum mechanical behaviours within the scope of semi-classical transport. The mesoscopic physics was named after its operating length-scale, the mesoscale. After extensive experimental research, results showed, that there is no strict borderline between the meso- and microscale. Therefore, the term *quantum transport* is more accurate. We refer to Nazarov & Blanter [38].

Quantum transport provides a vast amount of models and theories to successfully explain and predict experiments in nanophysics. But, experiments in nanophysics also provide many stimulations for further fields of study and also challenges existing theories in quantum transport by the discovery of new and unexpected phenomena. One of these phenomena are the unexplained conductance anomalies in quantum point contacts, which we are going to study in this thesis.

In 1988 the conductance quantization - probably the most important matter of fact within the scope of electron transport - was the first time experimentally confirmed by van Wees et al. [53] and Wharham et al. [54] using a constriction between two electron reservoirs within the nanometer regime, called *quantum point contact* (QPC). Besides this quantization, additional properties were found and further experiments revealed their generic nature. The most striking ones are an additional intermediate step at around $0.7 \times G_0$, the *0.7 anomaly*, an anomalous temperature and magnetic field dependence. These phenomena are highly in contrast to the non-interacting behaviour and, hence, we call them *conductance anomalies*, following [14]. Experimental and theoretical physicists made great effort to explain its physical origin. But until now, there exists no microscopic model which inherits all observable behaviour. The difficulties to explain these anomalies is in clear contrast to its structural simplicity and its meaning as a key element of more involved nanostructures. Therefore, it is adjusted to speak of a "Mesoscopic Mystery" [36]. At least, there is an scientific consensus that these conductance anomalies are caused by a many-body phenomena.

In 2008, Florian Bauer successfully managed use the functional Renormalization group (fRG) to study an one-dimensional extended interaction region for $T = 0K$ with a potential barrier modelling the QPC. He found several striking agreements with experiments, including the anomalous magnetic field behaviour.

In this thesis, we will proceed this promising approach and extend it towards two-dimensional systems. This will enable us to investigate additional submodes with higher energies. The extension is desirable, because the higher conductance steps reveal a quite different conductance behaviour in experiments compared to the first one. Our hope is not only to find a reason of this deviations but in fact to get useful hints of the physical origin of these anomalous conductance phenomena.

The outline of this thesis is a follows.

- In chapter 2, we give a brief introduction of fRG for an interacting Fermi system in the one-particle irreducible (1PI) scheme and state a static truncation approach for its practical implementation.
- In chapter 3, we show how the fRG approach can be applied to a 2D Hubbard model with a static potential applied to it. Therefore, we review basic features of tight-binding chains, and we introduce numerical methods to compute the required Green functions. Furthermore, we explain how the linear conductance can be computed within this fRG approach.
- In chapter 4, we discuss general features of quantum point contacts and go into its anomalous conduction behaviour occurring in experiments.
- In chapter 5, we investigate zero temperature linear conductance properties in interacting QPC geometries by using a saddle point constriction potential. We present a minute analysis of the functional dependence of the low energy scale h_* on potential curvatures and interaction energy within a 1D system. Furthermore, we give first results for magnetic field behaviour of higher conductance steps.
- In chapter 6, we conclude this thesis by giving a summary of the most important results and an outlook for further research possibilities.

Chapter 2

Functional renormalization group (fRG)

In this chapter we give a brief introduction of the functional renormalization group (fRG) for an interacting Fermi system in the one-particle irreducible (1PI) scheme, based on Meden [32] and Karrasch [20]. We derive the fRG flow equations for the vertex functions by introducing an infrared cutoff Λ in the free propagator and differentiating their generating functional with respect to this parameter. These equations are a hierarchy of infinitely many coupled differential equations, which describe the flow from a static to the full interacting system by successively including lower energy modes. For the practical implementation we discuss how to truncate this system. We will especially consider the case $T = 0$ and use a sharp cutoff to obtain the final form of the flow equations for the static self-energy and effective interaction. In the end we briefly introduce alternative fRG schemes, based on Enss [13].

2.1 Introduction

A lot of interesting effects exist in many-body physics which lead to divergencies in certain classes of Feynman diagrams or which are caused by processes acting on different energy scales. In general, these phenomena can't be treated using ordinary perturbation theory. An example is the Kondo effect where the energy scale T_K , the Kondo temperature, is exponentially small in the charging energy U and hence leads to a huge diversity of this energy scale. To encounter such problems one needs other methods besides standard perturbation theory.

The functional renormalization group (fRG) is such an alternative method. It is based on the idea of Wilson's renormalization group (RG). Within the RG approach of Wilson, the different energy scales are taken into account by successively integrating over certain energy degrees of freedom. For this purpose, a RG transformation is constructed which maps the original action of the microscopic model, by integrating over the corresponding modes, to an effective action. This leads to an effective theory for the remaining energy

scales and often provides an efficient description of the underlying physics.

The functional renormalization group is a variant of this renormalization group idea for interacting many-particle systems which is formulated in the language of functional integrals. In this implementation, low energy scales are excluded by inserting a parameter Λ in the free propagator, the so called infrared cutoff. Then the flow equation of a certain generating functional can be obtained by taking the derivative with respect to this parameter. In the one-particle irreducible (1PI) scheme, we consider the generating functional of the vertex functions Γ . Expanding the functional flow equation $d/d\Lambda \Gamma^\Lambda$ in the Λ -independent Grassmann fields leads to a hierarchy of infinitely many coupled differential equations for the expansion coefficients, the vertex functions. This hierarchy describes the evolution (flow) from the microscopic model to the effective action which is parametrized by the cutoff parameter Λ . The flow starts at the microscopic model and develops by successively including lower energy scales, to the effective action of the full interacting system which contains all physical relevant informations. This approach enables to control infrared singularities and competing instabilities. Furthermore, it often leads to non-divergent results due to appropriate resummation of Feynman diagrams. For practical implementation, one needs to introduce a suitable parametrization of the vertex functions and to introduce an appropriate truncation of this hierarchy of infinitely many coupled equations. This truncation proceeding will be justified by assuming weak renormalized interactions. But comparison with exact results shows that this perturbative truncation is remarkably accurate even for stronger interactions. And even in systems that don't suffer breakdown of perturbation theory, this method goes beyond a simple perturbative treatment. Because of this and the perturbative truncation with respect to the interaction, the fRG approach is also called *renormalization group enhanced perturbation theory* [32]. Also compare [1, 20, 2].

In the following we derive flow equations for the vertex functions describing an interacting system of fermions in the one-particle irreducible (1PI) scheme. We will follow the master thesis of Karrasch [20] which is based on the pedagogical introduction of Meden [32]. This proceeding can also be found in Bauer [3]. Therefore, we will keep the derivation rather sketchy and refer to these works for details of the calculations. A self-contained introduction of the functional integral formulation of the many-body theory, which is used throughout this chapter, can be found in Negele & Orland [39, chap. 1.5].

2.2 Many-particle Green functions

Our starting point is a system of interacting fermions described by the action functional

$$S[\bar{\psi}, \psi] = \left(\bar{\psi}, [\mathcal{G}^0]^{-1} \psi \right) - V[\bar{\psi}, \psi], \quad (2.1)$$

where $\bar{\psi} = \{\bar{\psi}_k\}$, $\psi = \{\psi_k\}$ denote Grassmann variables which are associated to creation and annihilation operators. Here, we used the abbreviation $(\bar{\psi}, \psi) := \sum_k \bar{\psi}_k \psi_k$ and $(\bar{\psi}, X\psi) := \sum_{k,k'} \bar{\psi}_k X_{k,k'} \psi_{k'}$ for the inner products. In the following, we denote by

$k := (iw_n, l)$ a multi-index which collects the Matsubara frequency w_n and the quantum number of a single-particle basis l . We assume that this basis diagonalizes the Hamiltonian of the non-interacting system. With respect to such a basis, the one-particle Green function of the non-interacting system G_1^0 reads

$$G_1^0(k) = \frac{1}{iw_n - \xi_l}, \quad (2.2)$$

where $\xi_l := \epsilon_l - \mu$ are the eigenenergies relative to the chemical potential. For the free propagator, we also use the notation $\mathcal{G}_l^0(iw_n) := G_1^0(k)$. The functional $V[\bar{\psi}, \psi]$ describes an arbitrary two-particle interaction

$$V[\bar{\psi}, \psi] = \frac{1}{4} \sum_{k'_1, k'_2, k_1, k_2} \bar{v}_{k'_1, k'_2; k_1, k_2} \bar{\psi}_{k'_1} \bar{\psi}_{k'_2} \psi_{k_2} \psi_{k_1}, \quad (2.3)$$

where we implicitly assume frequency conservation. Furthermore, we assume a factor β^{-1} to be absorbed in the anti-symmetrized tensor $\bar{v}_{k'_1, k'_2; k_2, k_1}$ of the two particle interaction. The grand canonical partition function of this interacting Fermi system is

$$\mathcal{Z} = \int \mathcal{D}\bar{\psi}\psi e^{S[\bar{\psi}, \psi]}, \quad (2.4)$$

where $\int \mathcal{D}\bar{\psi}\psi$ stands for $\int \prod_k d\psi_k d\bar{\psi}_k$.

2.2.1 Green functions - generating functionals

First of all, we introduce the generating functional $\mathcal{W}[\bar{\eta}, \eta]$ of the m-particle Green functions

$$\mathcal{W}[\bar{\eta}, \eta] = \frac{1}{\mathcal{Z}} \int \mathcal{D}\bar{\psi}\psi e^{S[\bar{\psi}, \psi] - (\bar{\psi}, \eta) - (\bar{\eta}, \psi)}, \quad (2.5)$$

where the partition function \mathcal{Z} acts as a normalization factor. It cancels out all non-interacting vacuum diagrams such that $\mathcal{W}[\bar{\eta} \equiv 0, \eta \equiv 0] = 1$. Using the functional $\mathcal{W}[\bar{\eta}, \eta]$, we can obtain the m-particle Green function G_m by taking m-times the derivative with respect to the source fields $\bar{\eta}, \eta$ evaluated at vanishing source fields, in explicit terms

$$\begin{aligned} G_m(k'_1, \dots, k'_m; k_1, \dots, k_m) &:= (-1)^m \langle \psi_{k'_1} \dots \psi_{k'_m} \bar{\psi}_{k_1} \dots \bar{\psi}_{k_m} \rangle \\ &= \frac{1}{\mathcal{Z}} \int \mathcal{D}\bar{\psi}\psi e^{S[\bar{\psi}, \psi]} \psi_{k'_1} \dots \psi_{k'_m} \bar{\psi}_{k_1} \dots \bar{\psi}_{k_m} \\ &= \frac{\delta^m}{\delta \bar{\eta}_{k'_1} \dots \delta \bar{\eta}_{k'_m}} \frac{\delta^m}{\delta \eta_{k_1} \dots \delta \eta_{k_m}} \mathcal{W}[\bar{\eta}, \eta] \Big|_{\bar{\eta}=\eta=0}. \end{aligned} \quad (2.6)$$

The generating functional of the connected m-particle Green function \mathcal{W}^c is given by the logarithm of \mathcal{W} [39]

$$\mathcal{W}^c[\bar{\eta}, \eta] = \ln(\mathcal{W}[\bar{\eta}, \eta]). \quad (2.7)$$

Analogously to (2.6), we can obtain the m -particle connected Green function G_m^c from \mathcal{W}^c via

$$\begin{aligned} G_m^c(k'_1, \dots, k'_m; k_1, \dots, k_m) &:= (-1)^m \langle \psi_{k'_1} \dots \psi_{k'_m} \bar{\psi}_{k_1} \dots \bar{\psi}_{k_m} \rangle_c \\ &= \frac{\delta^m}{\delta \bar{\eta}_{k'_1} \dots \delta \bar{\eta}_{k'_m}} \frac{\delta^m}{\delta \eta_{k_1} \dots \delta \eta_{k_m}} \mathcal{W}^c[\bar{\eta}, \eta] \Big|_{\bar{\eta}=\eta=0}, \end{aligned} \quad (2.8)$$

where $\langle \dots \rangle_c$ denotes the connected average of the product of Grassmann variables between the brackets.

Now we are going to introduce the m -particle vertex functions γ_m . They can be defined, in a diagrammatical way, as the sum of all one-particle irreducible diagrams with $2m$ amputated legs, where a one-particle irreducible diagram is a diagram that cannot be disconnected by removing a single internal propagator. In the following, we want to use an alternative definition by introducing their generating functional Γ , the so called *effective action*. This generating functional can be obtained by the modified Legendre transformation

$$\Gamma[\bar{\phi}, \phi] = -\mathcal{W}^c[\bar{\eta}, \eta] - (\bar{\phi}, \eta) - (\bar{\eta}, \phi) + (\bar{\phi}, [\mathcal{G}^0]^{-1}\phi), \quad (2.9)$$

where we define the independent Grassmann fields $\phi = \{\phi_k\}$, $\bar{\phi} = \{\bar{\phi}_k\}$ via

$$\bar{\phi}_k := \frac{\delta}{\delta \eta_k} \mathcal{W}^c[\bar{\eta}, \eta], \quad \phi_k := -\frac{\delta}{\delta \bar{\eta}_k} \mathcal{W}^c[\bar{\eta}, \eta]. \quad (2.10)$$

Compared to standard Legendre transformations, the additional term $(\bar{\phi}, [\mathcal{G}^0]^{-1}\phi)$ was added in the transformation (2.9). This term has no influence on the vertex functions but for neglecting this term it follows $\gamma_1 = G_1^{-1}$. Within this Legendre transformation the additional Therefore, we obtain a definition of the vertex functions γ_m analogously to the other Green functions, and within the functional integral formalism

$$\gamma_m(k'_1, \dots, k'_m; k_1, \dots, k_m) := \frac{\delta}{\delta \bar{\phi}_{k'_1} \dots \delta \bar{\phi}_{k'_m}} \frac{\delta}{\delta \phi_{k_1} \dots \phi_{k_m}} \Gamma[\bar{\phi}, \phi] \Big|_{\bar{\phi}=\phi=0}. \quad (2.11)$$

Using this definition, it can be shown that the vertex functions are indeed one-particle irreducible, and that the connected Green functions can be obtained from these functions by using only tree diagrams, compare Negele & Orland [39]. These are the two characteristic properties of the vertex functions. We are going to show this feature, at least for the one-particle vertex function γ_1 , which will lead to the Dyson equation and the identification of the one-particle vertex function with the self-energy.

2.2.2 Dyson equation and self-energy

To derive a relation between the connected Green functions and the vertex functions, we state

$$\begin{pmatrix} \frac{\delta^2 \Gamma}{\delta \phi \delta \phi} + [\mathcal{G}^0]^{-1} & \frac{\delta^2 \Gamma}{\delta \phi \delta \phi} \\ \frac{\delta^2 \Gamma}{\delta \phi \delta \phi} & \frac{\delta^2 \Gamma}{\delta \phi \delta \phi} - [[\mathcal{G}^0]^{-1}]^T \end{pmatrix} \begin{pmatrix} \frac{\delta^2 \mathcal{W}^c}{\delta \bar{\eta} \delta \eta} & -\frac{\delta^2 \mathcal{W}^c}{\delta \bar{\eta} \delta \eta} \\ -\frac{\delta^2 \mathcal{W}^c}{\delta \eta \delta \eta} & \frac{\delta^2 \mathcal{W}^c}{\delta \eta \delta \eta} \end{pmatrix} = \mathbf{1}, \quad (2.12)$$

see [32, p. 10], which connects the corresponding generating functionals \mathcal{W}^c and Γ . In this matrix equation, every entry itself is a matrix, for example $\frac{\delta^2\Gamma}{\delta\phi\delta\phi}$ is the Hessian matrix $\frac{\delta^2\Gamma}{\delta\phi_i\delta\phi_j}$. The derivation of this equation is long and rather straightforward. One has to keep in mind that $\phi, \bar{\phi}$ are independent variables, implying $\frac{\delta\phi_k}{\delta\phi_{k'}} = \frac{\delta\bar{\phi}_k}{\delta\phi_{k'}} = 0$, and that the derivatives with respect to Grassmann fields are anticommutative.

In the proceeding derivation of the fRG flow equations in section 2.3.2, we will need the equation (2.12) once again and especially the matrix

$$\mathcal{A}[\bar{\phi}, \phi] := \begin{pmatrix} \frac{\delta^2\Gamma}{\delta\phi\delta\phi} + [\mathcal{G}^0]^{-1} & \frac{\delta^2\Gamma}{\delta\phi\delta\bar{\phi}} \\ \frac{\delta^2\Gamma}{\delta\bar{\phi}\delta\phi} & \frac{\delta^2\Gamma}{\delta\bar{\phi}\delta\bar{\phi}} - [[\mathcal{G}^0]^{-1}]^T \end{pmatrix}^{-1}. \quad (2.13)$$

We assume that we are not in a phase of broken symmetry. Therefore, all Green functions with an unequal number of creation and annihilation operators vanish. Hence, the diagonal entries of \mathcal{A} are zero and we can derive

$$G_1(k'; k) = G_1^c(k'; k) := \frac{\delta^2\mathcal{W}^c}{\delta\bar{\eta}_{k'}\delta\eta_k} \Big|_{\bar{\eta}=\eta=0} = \left[\frac{\delta^2\Gamma}{\delta\bar{\phi}\delta\phi} \Big|_{\bar{\phi}=\phi=0} + [\mathcal{G}^0]^{-1} \right]_{k', k}^{-1}. \quad (2.14)$$

The equality $G_1 = G_1^c$ holds by the linked cluster theorem. The latter equation is equivalent to the well-known Dyson equation. The function G_1 is the one-particle Green function of the interacting system and we can identify the one-particle irreducible vertex function up to a sign with the self-energy Σ , in explicit terms

$$\gamma_1 := \frac{\delta^2\Gamma}{\delta\bar{\phi}\delta\phi} \Big|_{\bar{\phi}=\phi=0} = -\Sigma, \quad (2.15)$$

In the following, we will also use the notation

$$\mathcal{G} := \frac{1}{[\mathcal{G}^0]^{-1} + \gamma_1}, \quad (2.16)$$

in analogy to \mathcal{G}^0 for the one-particle propagator of the non-interacting system. It is well known that the self-energy is one-particle irreducible. Therefore, this also holds for the one-particle vertex function. The connected Green function of the full interacting system can be obtained by the Dyson equation. In Meden [32] the mentioned properties are also shown for the two-particle vertex function.

Physically, the vertex functions can be interpreted in a similar manner as the self-energy. It is well known that Σ specifies an effective one-body potential for a particle propagating in a many-particle system. The influence of all other particles is taken into account by this self-energy. Analogously the m-particle vertex function γ_m describes an effective m-particle interaction, which takes the many-particle medium into account. Therefore, we will call γ_2 also *effective two-particle interaction* or just *effective interaction*.

2.3 Functional renormalization group approach

In the previous section, we showed how the different Green functions of a fermionic many-body system can be defined via their generating functionals. Furthermore, we stated a matrix equation which connects \mathcal{W}^c and Γ . By this equation, we derived the Dyson equation for the one-particle vertex function. Using these preparations, we will continue in this section to determine the fRG flow equations for the vertex functions.

2.3.1 General proceeding

Before we delve into the details of the derivation, we give a sketch of the general proceeding, compare [20, chap. 2.2]. The first step is to introduce a parameter Λ in the bare propagator \mathcal{G}^0 , in explicit terms

$$\mathcal{G}^0 \longrightarrow \mathcal{G}^{0,\Lambda}, \quad (2.17)$$

where later we will always assume Λ to be an cut-off parameter. The exact Λ -dependence of the bare propagator is irrelevant for the derivation of the general form of the fRG flow equations. We just assume that for some value Λ_i the free propagator is zero ¹, and for another value Λ_f we obtain the ordinary free propagator, in explicit terms

$$\mathcal{G}^{0,\Lambda_i} = 0, \quad \mathcal{G}^{0,\Lambda_f} = \mathcal{G}^0. \quad (2.18)$$

Now the flow equation for any physical quantity $\mathcal{X}^\Lambda(x_1, \dots, x_n) := \mathcal{X}(\mathcal{G}^{0,\Lambda}, x_1, \dots, x_n)$ can be obtained by taking the derivative with respect to Λ

$$\frac{d}{d\Lambda} \mathcal{X}^\Lambda(x_1, \dots, x_n) = \mathcal{Y}^\Lambda(\mathcal{X}^\Lambda, x_1, \dots, x_n). \quad (2.19)$$

Because we claimed $\mathcal{G}^{0,\Lambda_i} = 0$, it is likely that $\mathcal{X}^{\Lambda_i}(x_1, \dots, x_n)$ can easily be calculated. Hence, we can integrate (2.19) from the initial $\Lambda = \Lambda_i$ to the final value $\Lambda = \Lambda_f$, and obtain the desired quantity $\mathcal{X}^{\Lambda_f}(x_1, \dots, x_n) = \mathcal{X}(\mathcal{G}^0, x_1, \dots, x_n)$ for the full interacting system. In general \mathcal{X} depends on some Λ -independent variables $\{x_1, \dots, x_n\}$. A Taylor expansion with respect to these variable is considerable if the corresponding coefficients are of physical interest. Because, this leads to a hierarchy of flow equations for the expansion coefficients. In the 1PI scheme $\mathcal{X} = \Gamma$ and it can be assumed that the fields $\bar{\phi}, \phi$ are Λ -independent. In this case the corresponding expansion coefficients are the vertex functions γ_m . Solving the differential equations for the coefficients is equivalent to solving the original functional flow equation (2.19). Unfortunately, the resulting differential equations are in general coupled and not finite. Therefore, it is necessary to truncate this hierarchy of infinitely many differential equations at some point. To be able to a physically motivated truncation, it is important to make a suitable choice of the quantity \mathcal{X} and the Λ -dependence.

¹It is sufficient to demand that $\mathcal{G}^{0,\Lambda_i}$ can easily be calculated.

2.3.2 fRG flow equations

Now we apply this general proceeding to the generating functional Γ and derive the fRG flow equations for the vertex functions γ_m , which reveal to be the expansion coefficients of the Grassmann fields $\bar{\phi}$ and ϕ .

We assume that we have inserted a cutoff parameter Λ with the properties (2.18) into the bare propagator. Therefore, all introduced functionals become also Λ -dependent and the single-particle propagator of the interacting system becomes

$$\mathcal{G}^\Lambda = \frac{1}{[\mathcal{G}^{0,\Lambda}]^{-1} + \gamma_1^\Lambda}. \quad (2.20)$$

Before we derive the functional flow equation of the generating functional of the vertex functions Γ , we recall their definition by the Legendre transformation (2.9). Because we want that the fields $\phi, \bar{\phi}$ to be Λ -independent and because the generating functional \mathcal{W}^c is Λ -dependent, the fields $\eta, \bar{\eta}$ must also be Λ -dependent, which follows from the definition (2.10). Therefore, the Legendre transformation reads

$$\Gamma^\Lambda[\bar{\phi}, \phi] = -\mathcal{W}^{c,\Lambda}[\bar{\eta}^\Lambda, \eta^\Lambda] - (\bar{\phi}, \eta^\Lambda) - (\eta^\Lambda, \phi) + (\bar{\phi}, [\mathcal{G}^{0,\Lambda}]^{-1} \phi) \quad (2.21)$$

after introducing the cutoff-parameter. Using this expression of $\Gamma^\Lambda[\bar{\phi}, \phi]$ it is easy to show that the effective action satisfies the following *functional flow equation* [32]

$$\begin{aligned} \frac{d}{d\Lambda} \Gamma^\Lambda[\bar{\phi}, \phi] &= \text{Tr} \left(\mathcal{G}^{0,\Lambda} \partial_\Lambda [\mathcal{G}^{0,\Lambda}]^{-1} \right) - \text{Tr} \left(\partial_\Lambda [\mathcal{G}^{0,\Lambda}]^{-1} \frac{\delta^2 \mathcal{W}^{c,\Lambda}}{\delta \bar{\eta} \delta \eta} \right) \\ &= \text{Tr} \left(\mathcal{G}^{0,\Lambda} \partial_\Lambda [\mathcal{G}^{0,\Lambda}]^{-1} \right) - \text{Tr} \left(\partial_\Lambda [\mathcal{G}^{0,\Lambda}]^{-1} \mathcal{A}_{1,1}^\Lambda [\bar{\phi}, \phi] \right). \end{aligned} \quad (2.22)$$

For this calculation, it is convenient to replace the grand canonical partition function of the interacting system \mathcal{Z} (2.4) in the definition of \mathcal{W}^c (2.7) by the partition function of the non-interacting system \mathcal{Z}^0 , where

$$\mathcal{Z}^0 := \int \mathcal{D}\bar{\psi}\psi e^{(\bar{\psi}, [\mathcal{G}^0]^{-1} \psi)}. \quad (2.23)$$

This replacement changes \mathcal{W}^c and Γ only by a constant. Therefore, it has no influence on the m -particle Green functions for $m \geq 1$. In the following, we want to concentrate on equation (2.22). We expand the left and right-hand side in the Λ -independent fields $\bar{\phi}$ and

ϕ . For this purpose we rewrite

$$\begin{aligned} \mathcal{A}^\Lambda [\bar{\phi}, \phi] &= \left(\begin{array}{cc} \frac{\delta^2 \Gamma^\Lambda}{\delta \bar{\phi} \delta \phi} + [\mathcal{G}^{0,\Lambda}]^{-1} & \frac{\delta^2 \Gamma^\Lambda}{\delta \bar{\phi} \delta \phi} \\ \frac{\delta^2 \Gamma^\Lambda}{\delta \phi \delta \phi} & \frac{\delta^2 \Gamma^\Lambda}{\delta \phi \delta \phi} - [[\mathcal{G}^{0,\Lambda}]^{-1}]^T \end{array} \right)^{-1} = \left(\begin{array}{cc} \mathcal{U}^\Lambda + [\mathcal{G}^\Lambda]^{-1} & \frac{\delta^2 \Gamma^\Lambda}{\delta \bar{\phi} \delta \phi} \\ \frac{\delta^2 \Gamma^\Lambda}{\delta \phi \delta \phi} & -\mathcal{U}^\Lambda - [[\mathcal{G}^\Lambda]^{-1}]^T \end{array} \right)^{-1} \\ &= \underbrace{\left[\mathbb{1} - \underbrace{\begin{pmatrix} -\mathcal{G}^\Lambda & 0 \\ 0 & [\mathcal{G}^\Lambda]^T \end{pmatrix} \cdot \begin{pmatrix} \mathcal{U}^\Lambda & \frac{\delta^2 \Gamma^\Lambda}{\delta \bar{\phi} \delta \phi} \\ \frac{\delta^2 \Gamma^\Lambda}{\delta \phi \delta \phi} & -\mathcal{U}^\Lambda \end{pmatrix}}_{=: A^\Lambda [\bar{\phi}, \phi]} \right]^{-1}}_{=: \tilde{\mathcal{A}}^\Lambda [\bar{\phi}, \phi]} \cdot \begin{pmatrix} \mathcal{G}^\Lambda & 0 \\ 0 & -[\mathcal{G}^\Lambda]^T \end{pmatrix}. \end{aligned} \quad (2.24)$$

Here, we defined

$$\mathcal{U}^\Lambda [\bar{\phi}, \phi] := \frac{\delta^2 \Gamma^\Lambda}{\delta \bar{\phi} \delta \phi} - \frac{\delta^2 \Gamma^\Lambda}{\delta \bar{\phi} \delta \phi} \Big|_{\bar{\phi}=\phi=0} = \frac{\delta^2 \Gamma^\Lambda}{\delta \bar{\phi} \delta \phi} - \gamma_1^\Lambda \quad (2.25)$$

as the difference between the second derivative of Γ and the one-particle vertex function. With this equation and the definition of $\tilde{\mathcal{A}}^\Lambda$, the identity $\mathcal{A}_{1,1}^\Lambda = \tilde{\mathcal{A}}_{1,1}^\Lambda \mathcal{G}^\Lambda$ holds. We insert this identity into the functional flow equation 2.22 of Γ^Λ and obtain

$$\frac{d}{d\Lambda} \Gamma^\Lambda [\bar{\phi}, \phi] = \text{Tr} \left(\mathcal{G}^{0,\Lambda} \partial_\Lambda [\mathcal{G}^{0,\Lambda}]^{-1} \right) - \text{Tr} \left(\mathcal{G}^\Lambda \partial_\Lambda [\mathcal{G}^{0,\Lambda}]^{-1} \tilde{\mathcal{A}}_{1,1}^\Lambda [\bar{\phi}, \phi] \right). \quad (2.26)$$

This new functional $\tilde{\mathcal{A}}^\Lambda [\bar{\phi}, \phi]$ can be expanded with respect to A^Λ

$$\tilde{\mathcal{A}}^\Lambda = [1 + A^\Lambda]^{-1} = \mathbb{1} + \sum_{k=1}^{\infty} (-A^\Lambda)^k. \quad (2.27)$$

After truncating at second order the entry (1, 1) of $\tilde{\mathcal{A}}^\Lambda$ reads

$$\tilde{\mathcal{A}}_{1,1}^\Lambda = 1 - \mathcal{G}^\Lambda \mathcal{U}^\Lambda + \mathcal{G}^\Lambda \mathcal{U}^\Lambda \mathcal{G}^\Lambda \mathcal{U}^\Lambda - \mathcal{G}^\Lambda \frac{\delta^2 \Gamma^\Lambda}{\delta \bar{\phi} \delta \phi} [\mathcal{G}^\Lambda]^T \frac{\delta^2 \Gamma^\Lambda}{\delta \phi \delta \phi} + \dots \quad (2.28)$$

Inserting $\tilde{\mathcal{A}}_{1,1}^\Lambda$ in (2.26), we are left to expand Γ^Λ and \mathcal{U}^Λ in the fields $\bar{\phi}, \phi$. By the definition of γ_m^Λ (2.11) the expansion of Γ^Λ reads

$$\Gamma^\Lambda [\bar{\phi}, \phi] = \sum_{m=0}^{\infty} \frac{(-1)^m}{(m!)^2} \sum_{k'_1, \dots, k'_m} \sum_{k_1, \dots, k_m} \gamma_m^\Lambda (k'_1, \dots, k'_m; k_1, \dots, k_m) \bar{\phi}_{k'_1} \dots \bar{\phi}_{k'_m} \phi_{k_1} \dots \phi_{k_m} \quad (2.29)$$

The minus sign emerges from the commutation of the derivatives with respect to the Grassmann fields. The expansion of \mathcal{U}^Λ which reads

$$[\mathcal{U}^\Lambda [\bar{\phi}, \phi]]_{q', q} = \sum_{m=1}^{\infty} \frac{(-1)^m}{(m!)^2} \sum_{k'_1, \dots, k'_m} \sum_{k_1, \dots, k_m} \gamma_{m+1}^\Lambda (k'_1, \dots, k'_m, q'; k_1, \dots, k_m, q) \bar{\phi}_{k'_1} \dots \bar{\phi}_{k'_m} \phi_{k_1} \dots \phi_{k_m}. \quad (2.30)$$

follows from equation (2.25). Using the equations (2.28), (2.29) and (2.30), we can finally obtain an expansion of the left and right-hand side of (2.26) with respect to $\bar{\phi}$, ϕ and acquire ordinary differential equations for the expansion coefficients γ_m^Λ .

Flow equations for γ_0

We collect all terms on the right and left-hand side of the flow equation of Γ^Λ (2.26) which don't depend on $\bar{\phi}$, ϕ and obtain the flow equations for γ_0 , given by

$$\frac{d}{d\Lambda}\gamma_0^\Lambda = \text{Tr}(\mathcal{G}^{0,\Lambda}\partial_\Lambda[\mathcal{G}^{0,\Lambda}]^{-1}) - \text{Tr}(\mathcal{G}^\Lambda\partial_\Lambda[\mathcal{G}^{0,\Lambda}]^{-1}). \quad (2.31)$$

Flow equations for γ_1

In order to derive the flow equations for the one-particle vertex function, we define, for notational simplicity, the so called *single-scale propagator*, which reads

$$\mathcal{S}^\Lambda := \mathcal{G}^\Lambda\partial_\Lambda[\mathcal{G}^{0,\Lambda}]^{-1}\mathcal{G}^\Lambda. \quad (2.32)$$

With this definition we obtain, by collecting all terms with equal powers in $\bar{\phi}\phi$, the differential equations which determine the one-particle vertex function

$$\frac{d}{d\Lambda}\gamma_1^\Lambda(k'; k) = \text{Tr}(\mathcal{S}^\Lambda\gamma_2^\Lambda(k', \cdot; k, \cdot)). \quad (2.33)$$

Here $\gamma_2^\Lambda(k', \cdot; k, \cdot)$ is an abbreviation for the matrix $[\gamma_2^\Lambda(k', \cdot; k, \cdot)]_{q,q'} := \gamma_2^\Lambda(k', q; k, q')$.

Flow equations for γ_2

The flow equations for the two-particle vertex function can be obtained by finding all terms on the left and right-hand side of (2.26) containing equal powers in $\bar{\phi}\bar{\phi}\phi\phi$. By comparison of coefficients we obtain

$$\begin{aligned} \frac{d}{d\Lambda}\gamma_2^\Lambda(k'_1, k'_2; k_1, k_2) = & \text{Tr}(\mathcal{S}^\Lambda\gamma_3^\Lambda(k'_1, k'_2, \cdot; k_1, k_2, \cdot)) \\ & - \text{Tr}(\mathcal{S}^\Lambda\gamma_2^\Lambda(\cdot, \cdot; k_1, k_2)[\mathcal{G}^\Lambda]^T\gamma_2^\Lambda(k'_1, k'_2; \cdot, \cdot)) \\ & - \text{Tr}(\mathcal{S}^\Lambda\gamma_2^\Lambda(k'_1, \cdot; k_1, \cdot)\mathcal{G}^\Lambda\gamma_2^\Lambda(k'_2, \cdot; k_2, \cdot)) \\ & - \text{Tr}(\mathcal{S}^\Lambda\gamma_2^\Lambda(k'_2, \cdot; k_2, \cdot)\mathcal{G}^\Lambda\gamma_2^\Lambda(k'_1, \cdot; k_1, \cdot)) \\ & + \text{Tr}(\mathcal{S}^\Lambda\gamma_2^\Lambda(k'_2, \cdot; k_1, \cdot)\mathcal{G}^\Lambda\gamma_2^\Lambda(k'_1, \cdot; k_2, \cdot)) \\ & + \text{Tr}(\mathcal{S}^\Lambda\gamma_2^\Lambda(k'_1, \cdot; k_2, \cdot)\mathcal{G}^\Lambda\gamma_2^\Lambda(k'_2, \cdot; k_1, \cdot)). \end{aligned} \quad (2.34)$$

At this point we stop writing down the flow equations for higher ordered vertex functions. But it should have become clear how we could obtain the differential equations for the m -particle vertex functions for $m > 2$.

Figure 2.1: Graphical representation of the fRG flow equations for the self-energy Σ^Λ , the two-particle vertex γ_2^Λ and the three-particle vertex function γ_3^Λ [2].

Diagrammatical representation

A rather efficient way of remembering and thinking of the fRG flow equations are to visualize them by diagrams. We follow the diagrammatical representation used in [13, 1]. A m -particle vertex function is symbolized by a big dot with $2m$ external lines, the single-scale propagator by a crossed out line and \mathcal{G}^Λ by a single line. Furthermore, the derivative is visualized by a partial derivative in front of the vertex function. Using these symbols the fRG flow equations in the 1PI scheme of the self-energy, the one-particle and two-particle vertex functions have the diagrammatic illustration shown in figure 2.1. Each of the connecting lines can represent a propagating particle or a propagating hole. For example the last diagram of the second equation and the second diagram of the right-hand side of the last equation includes, besides a particle-particle bubble, also a particle-hole bubble. For a more detailed diagrammatic representation, which is important for considerations about symmetries and spin conservation, we refer to [32] or [3]. But the diagrams in figure 2.1 are sufficient to exemplify the general structure of fRG flow equations.

Structure of the flow equations

First of all, let's have a look on the flow of γ_0 (2.31). This is a special case, because it's the vertex function with lowest order. The right-hand side of the differential equation only depends on the vertex function γ_1 via \mathcal{G} . This dependency on γ_1 holds for flow equations of all vertex functions, and hence we call this dependency natural. The right-hand side of the differential equation of the next higher vertex function, γ_1 , depends on the vertex function γ_2 , besides the natural dependency (2.33). Therefore, we say it's generated by γ_2 . The flow of the two-particle vertex function γ_2 is generated by γ_3 and γ_2 (2.34). Proceeding in this way, we could easily convince ourselves that γ_m is generated by γ_{m+1} and $\gamma_{m-1}, \gamma_{m-2}, \dots, \gamma_2$. We see that the fRG flow equations for the vertex functions define a hierarchy of infinitely many coupled ordinary differential equations. To solve this system of coupled differential equations, it is necessary to make a good approximation that reduces the hierarchy to a system of finitely many coupled differential equations. This approximation should be good in the sense that the solution of the resulting system is as close as possible to the exact solution. In this graphical representation of the flow equations, we can further observe that the right-hand side just consists of one-loop terms (no tree terms appear). During the fRG flow diagrams with a higher number of loops are generated.

Initial conditions

Up to now, we have managed to derive the fRG flow equations for the vertex functions. To obtain well defined solutions, we have to determine the initial conditions. They can be derived analytically [32] and read

$$\begin{aligned}\gamma_2^{\Lambda_i}(k'_1, k'_2; k_1, k_2) &= \bar{v}_{k'_1, k'_2; k_1, k_2} \\ \gamma_m^{\Lambda_i} &\equiv 0 \quad \text{for } m \neq 2.\end{aligned}\tag{2.35}$$

This from of the initial conditions can be understood by the following diagrammatically consideration. For the initial value of the cut-off parameter we set $\mathcal{G}^{0, \Lambda_i} = 0$ and hence, all diagrams with a bare propagator vanish and only the diagram that represents the bare interaction survives.

Symmetries within the flow equations

For a specific implementation of fRG, the flow equations can be greatly simplified using the following symmetries of the two-particle vertex function

$$\begin{aligned}\gamma_2(k'_1, k'_2; k_1, k_2) &= -\gamma_2(k'_2, k'_1; k_1, k_2) \\ &= -\gamma_2(k'_1, k'_2; k_2, k_1) \\ &= +\gamma_2(k_1, k_2; k'_1, k'_2).\end{aligned}\tag{2.36}$$

It is antisymmetric under change of the first and second two entries and symmetric under change of the first and the second two entries. This follows by the definition of the two-particle vertex function as the amputated two-particle connected Green function, in explicit

terms

$$\gamma_2(k'_1, k'_2; k_1, k_2) = - \sum_{q'_1, q'_2; q_1, q_2} [\mathcal{G}]_{k'_1, q'_1}^{-1} [\mathcal{G}]_{k'_2, q'_2}^{-1} [\mathcal{G}]_{q_2, k_2}^{-1} [\mathcal{G}]_{q_1, k_1}^{-1} G_2^c(q'_1, q'_2; q_1, q_2). \quad (2.37)$$

The latter equation can be derived by the generating functional of the vertex function (2.9) and the matrix equation (2.12).

In the following considerations the one-particle quantum numbers and hence k will also include a spin index. This leads to spin-conserving vertex functions for a spin-conserving bare interaction and a spin-conserving free propagator

2.4 Specification of the truncation and the cutoff

In the previous section we derived the fRG flow equations for the vertex functions in a very general way by inserting an unspecified cutoff parameter Λ in the bare propagator. We also observed the need to truncate this hierarchy of infinitely many coupled differential equations in order to obtain a solvable system. In this section we give a practical implementation of this general concept in the limit $T = 0$ and specify, in particular, the cutoff and the truncation scheme.

2.4.1 Truncation scheme

The flow equations for the vertex functions is a hierarchy of infinitely many coupled ordinary differential equations. For solving these differential equations numerically, we have to truncate this hierarchy at some point. In the 1PI scheme, this can be done in a perturbative sense under the condition that the interaction is small. In the following, we assume that this condition holds.

Since the m -particle vertex function consists of diagrams that are at least of order m in the interaction, the m -particle vertex is also at least of order m in the interaction. And we can perform a perturbative truncation by neglecting the flow of vertices of order higher than some critical value m_c , in explicit terms

$$\frac{d}{d\Lambda} \gamma_m = 0 \quad \text{for } m \geq m_c. \quad (2.38)$$

We emphasize that $\gamma_{m_c}^\Lambda \equiv \gamma_{m_c}^{\Lambda_i}$ and we are left with a system of coupled differential equations consisting of the vertices $\gamma_1, \dots, \gamma_{m_c-1}$. This approach, of setting small terms in a differential equation to zero, is of course not exact and might bias the results strongly. But, it can be justified in the following way using a fRG argument. At the beginning of the flow all vertex functions are zero, except γ_2 , which is equal to the bare two-particle interaction. Under the additional assumption that γ_2^Λ stays small during the fRG flow $\Lambda_i \rightarrow \Lambda_f$, we can argue that all higher vertices are initially generated in third or higher order by $\gamma_2^{\Lambda_i} = \bar{v}$ and therefore also stay small.

In the following we will set $m_c = 3$ and obtain a system of differential equations consisting of the one- and two-particle vertex functions and equations (2.33) and (2.34). We choose this critical value because of numerical reasons. The vertex function γ_m is a tensor of rank $2m$ in the variables $k = (iw_n, l)$ and even if we only take γ_1 and γ_2 into account, we have to perform additional approximations in chapter 3 to be able to solve the occurring differential equations.

Frequency independent vertex functions

We already mentioned, the vertex functions are complicated quantities depending on a huge set of variables. Beside the dependency on the one-particle quantum number, we also have to take infinitely many Matsubara frequencies into account.

At the beginning of the fRG flow the two-particle vertex function is the bare interaction, and its frequency dependency is the Matsubara frequency conservation. A non trivial dependency is generated during the fRG flow by the bare propagator. To be able to solve the differential flow equations at all, we have to reduce somehow the number of frequencies that the vertex functions depend on. We will do this by assuming that γ_2 is frequency-independent, despite Matsubara frequency conservation, in explicit terms

$$\gamma_2^\Lambda(k'_1, l'_1; k'_2, l'_2; k_1, l_1; k_2, l_2) \equiv \delta_{w_1+w_2, w'_1+w'_2} \gamma_2^\Lambda(l'_1, l'_2; l_1, l_2). \quad (2.39)$$

This approach immediately implies that we will only be able to calculate observable for zero Matsubara frequencies and hence for zero temperature. The extension to finite frequencies is very complicated and is a direction of proceeding studies.

Using this approximation the one-particle vertex function also becomes frequency independent. The whole influence of the interaction is contained in the frequency independent self-energy $\Sigma^{\Lambda_f} = -\gamma_1^{\Lambda_f}$. Besides the focus on zero frequency, we also perform the previously described truncation of neglecting all higher ordered vertices and hence we define this zero frequency self-energy as effective self-energy, in explicit terms

$$\Sigma_{eff} := \Sigma^{\Lambda_f} = -\gamma_1^{\Lambda_f} \quad (2.40)$$

that we obtain by solving the truncated fRG flow equations. Therefore, we end up with an *effective non-interacting model* described by the quadratic effective action

$$S_{eff}[\bar{\psi}, \psi] = (\bar{\psi}, [\mathcal{G}_{eff}]^{-1} \psi) \quad \text{with} \quad \mathcal{G}_{eff} = \frac{1}{\mathcal{G}^0 - \Sigma_{eff}}. \quad (2.41)$$

Because we can't control the influence of these approximations on the desired results, we hope that this effective model describes the exact fully interacting system well.

We summarize, by this truncation scheme, also called *static fRG*, the functional renormalization group method maps the interacting system to an effective non-interacting system. The whole influence of the interaction is taken into account by the static self-energy Σ_{eff} . This effective self-energy is obtained by solving the fRG flow equations, which is a coupled system of differential equations consisting of the one- and two-particle vertex functions.

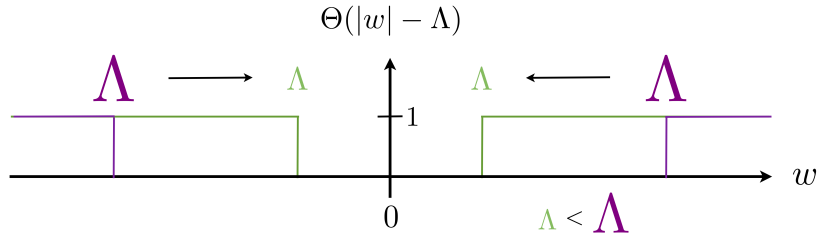


Figure 2.2: Illustration of the sharp cutoff function $C^\Lambda(iw_n) = \Theta(|w_n| - \Lambda)$ and the direction of the fRG flow.

2.4.2 Cutoff insertion

In the following, we focus on a physical system that is not translational invariant. Hence, the cutoff in momentum space is less efficient, and we choose an implementation in frequency space. This is done by multiplying the bare propagator in the action by a cutoff function $C^\Lambda(iw_n)$. For this cutoff function holds $C^{\Lambda_i} \equiv 0$, $C^{\Lambda_f} \equiv 1$ to fulfil (2.18) and in addition it should cut out the low-energy (soft) modes below Λ . The simplest implementation is a sharp cutoff function $C^\Lambda(iw_n) = \Theta(|w_n| - \Lambda)$, visualized in figure 2.2. This leads to the regularized bare propagator

$$\mathcal{G}^{0,\Lambda}(iw_n) = \Theta(|w_n| - \Lambda) \mathcal{G}^0(iw_n), \quad (2.42)$$

where

$$\Lambda_i := \infty \quad \text{and} \quad \Lambda_f := 0, \quad (2.43)$$

and Θ is the Heaviside step function. At this point it is not clear that such a discontinuous behaviour of the Green function in Λ provides well-defined results. But, we will see, in case $T = 0$, the sharp cutoff will greatly simplify the proceeding calculations. Therefore, this cutoff is the first choice in the case $T = 0$. Whereas, for treating finite temperatures, one has to use a smooth cutoff function [13].

2.4.3 Resulting flow equations

Using the specification of the infrared cutoff Λ and the truncation scheme, we can set up the final form of the functional renormalization group flow equations for the one and two-particle vertex functions. First of all, one can use that for the sharp cutoff (2.42) the scaling propagator becomes [20]

$$\mathcal{S}^\Lambda = \delta(|w| - \Lambda) \partial_\Theta \mathcal{G}^\Lambda. \quad (2.44)$$

This propagator is proportional to $\delta(|w| - \Lambda)$ and will simplify the summation over the Matsubara frequencies included in the trace of the flow equations (2.33) and (2.34). In the limit $T \rightarrow 0K$ the summation becomes an integral, in explicit terms $\sum_{iw_n} \rightarrow (2\pi)^{-1} \int dw$. Using Morris lemma [37], that states

$$\delta_\epsilon(x - \Lambda) f(\Theta_\epsilon(x - \Lambda)) \xrightarrow{\epsilon \rightarrow 0} \delta(x - \Lambda) \int_0^1 dt f(t),$$

where δ_ϵ , Θ_ϵ are sequences of functions $\delta_\epsilon(x) \xrightarrow{\epsilon \rightarrow 0} \delta(x)$ and $\Theta_\epsilon(x) \xrightarrow{\epsilon \rightarrow 0} \Theta(x)$, we can derive the final version of the flow equations for the one-particle vertex function. Which, for the one-particle vertex function, is given by

$$\frac{d}{d\Lambda} \gamma_1^\Lambda(k'; k) = \frac{1}{2\pi} \sum_{w=\pm\Lambda} \sum_{q,q'} \tilde{\mathcal{G}}_{q,q'}^\Lambda(iw) \gamma_2^\Lambda(k', q'; k, q) \quad (2.46)$$

and the two particle vertex function

$$\begin{aligned} \frac{d}{d\Lambda} \gamma_2^\Lambda(k'_1, k'_2; k_1, k_2) = & \\ \frac{1}{2\pi} \sum_{w=\pm\Lambda} \sum_{q,q';s,s'} & \left[-\frac{1}{2} \tilde{\mathcal{G}}_{q,q'}^\Lambda(iw) \gamma_2^\Lambda(q', s'; k_1, k_2) \tilde{\mathcal{G}}_{s,s'}^\Lambda(-iw) \gamma_2^\Lambda(k'_1, k'_2; s, q) \right. \\ & - \tilde{\mathcal{G}}_{q,q'}^\Lambda(iw) \gamma_2^\Lambda(k'_1, q'; k_1, s) \tilde{\mathcal{G}}_{s,s'}^\Lambda(iw) \gamma_2^\Lambda(k'_2, s'; k_2, q) \\ & \left. + \tilde{\mathcal{G}}_{q,q'}^\Lambda(iw) \gamma_2^\Lambda(k'_2, q'; k_1, s) \tilde{\mathcal{G}}_{s,s'}^\Lambda(iw) \gamma_2^\Lambda(k'_1, s'; k_2, q) \right]. \end{aligned} \quad (2.47)$$

Here, we introduced the modified Green function which is defined by

$$\tilde{\mathcal{G}}^\Lambda := \frac{1}{[\mathcal{G}^0]^{-1} + \gamma_1^\Lambda} \quad (2.48)$$

and depends on Λ only via γ_1^Λ . Hence, it has no step in $w = \pm\Lambda$, opposed to \mathcal{G}^Λ (2.20). The detailed derivation of the fRG flow equations can be found in Karrasch [20] or Bauer [3]. These two equations are the starting point of our further calculations and after introducing a specific model, we will come back to these equations.

2.4.4 Modified initial conditions

We return to the initial conditions of section 2.3.2, where we stated that all vertex functions are zero for Λ_i , despite the two-particle vertex that is given by the bare two-particle interaction. This is still true. But the problem is that we neglected all convergence factors e^{iw0^+} that occur in a precise derivation, starting with the partition function in the continuous version of the functional integral. Such a derivation would show that the quadratic action S^0 , describing the non-interacting system, has the form

$$S^0 = \sum_l \sum_{iw_n} e^{iw_n 0^+} \bar{\psi}(iw_n) [\mathcal{G}_l^0(iw_n)]^{-1} \psi_l(iw_n), \quad (2.49)$$

in contrast to (2.1), where we have neglected the convergence factor. The influence is taken into account by calculating the contribution of the convergence factor e^{iw0^+} in the limit $\Lambda \rightarrow \infty$. This can be done by calculating

$$\frac{1}{2\pi} \lim_{\Lambda_0 \rightarrow \infty} \lim_{\epsilon \rightarrow 0} \int_0^{\Lambda_0} d\Lambda \sum_{w=\pm\Lambda} \sum_{q,q'} e^{iw\epsilon} \tilde{\mathcal{G}}^\Lambda(iw) \gamma_2^\Lambda(l', q'; l, q) = -\frac{1}{2} \sum_q \bar{v}_{l',q,l,q}, \quad (2.50)$$

compare [20], which is the difference in the flow equation for the one-particle vertex function, if we perform the limit $0+$ before $\Lambda_0 \rightarrow \infty$. Therefore, neglecting this convergence factor in our numerical implementation leads to a modification of the initial conditions

$$\gamma_1^{\tilde{\Lambda}_i}(l'; l) = -\frac{1}{2} \sum_q \bar{v}_{l', q; l, q} \quad (2.51)$$

$$\gamma_2^{\tilde{\Lambda}_i}(l'_1, l'_2; l_1, l_2) = \bar{v}_{l'_1, l'_2; l_1, l_2} \quad (2.52)$$

$$\gamma_m^{\tilde{\Lambda}_i} \equiv 0 \quad \text{for } m > 2, \quad (2.53)$$

where $\tilde{\Lambda}_i$ is a very high number, greater than all energy scales.

2.5 Alternative RG schemes

In the previous derivations, we restricted ourselves to the one-particle irreducible (1PI) scheme of the fRG method with a regularization parameter Λ that cuts out low-energy modes in the Matsubara frequency space. To get a deeper understanding of this proceeding and an overview over alternative methods, we want to give a brief introduction to other RG schemes, namely the Polchinski and the Wick-ordered scheme. This overview will be based on the pedagogic introduction of Enss [13].

In some physical systems perturbation theory leads to infrared divergences, as a consequence of phase transitions, or as an artefact of the perturbative treatment. This divergences can be regularized by an infrared cutoff Λ in the bare propagator \mathcal{G}^0 , which excludes all low-energy modes. This cutoff can be performed in the momentum or frequency space. Alternative regularization parameters are the temperature, the coupling strength or the system size. They are inserted into the action in such a way, that only the quadratic part of the action depends on the regularization parameter.

In the *temperature flow* approach, where the quadratic and the quartic part depend on T ($S_{quad} \propto T$, $S_{quar} \propto T^4$), the fields are rescaled as $\tilde{\psi} := T^{3/4}\psi$ to eliminate the temperature dependence in the quartic part. Performing the fRG flow on the resulting action \tilde{S} leads to a flow equation of the Green function G_m^T in terms of the new fields. At the end of the flow, G_m^T is rescaled to obtain the usual Green function.

The *interaction flow* is based on rescaling the bare propagator just by a number g , in explicit $\mathcal{G}^0 \rightarrow g\mathcal{G}^0$, with $g \in [0, 1]$. Hence the weight of all Feynman diagrams are shifted by the global factor g^m , where m is the number of internal lines in this particular diagram. Including $g\mathcal{G}^0$ into the action, we can set up a fRG flow of the Green functions G_m^g starting from $g = 0$ to $g = 1$. By rescaling the fields $\tilde{\psi} = g^{-1/2}\psi$, one can show that this proceeding is equivalent to performing a flow in the bare two-particle interaction $g^2V \xrightarrow{g \rightarrow 0} V$. Therefore, this RG approach is called interaction flow approach.

Starting from such an insertion of a regularization parameter into the quadratic part of the action, different flow schemes can be obtained by considering the functional differential flow equations of different generating functionals. In the 1PI scheme, we described in

the previous sections, we differentiated the generating functional of the vertex function Γ^Λ with respect to our regularization parameter Λ and obtained the renormalization group flow equations for the one-particle irreducible connected amputated Green functions, the vertex functions. In the *Polchinski scheme*, the same proceeding for the generating functional of the connected amputated Green function, which are defined by

$$\mathcal{V}[\bar{\chi}, \chi] = \mathcal{W}^c[\bar{\eta}, \eta] - (\bar{\eta}, \mathcal{G}^0 \eta), \quad (2.54)$$

where $\chi := \mathcal{G}^0 \eta$ and $\bar{\chi} := [\mathcal{G}^0]^T \bar{\eta}$, provides a fRG flow of the connected amputated m-particle Green functions

$$V_m(k'_1, \dots, k'_m; k_1, \dots, k_m) := \frac{\delta^m}{\delta \bar{\chi}_{k'_1} \dots \delta \bar{\chi}_{k'_m}} \frac{\delta^m}{\delta \chi_{k_1} \dots \delta \chi_{k_m}} \mathcal{V}[\bar{\chi}, \chi]. \quad (2.55)$$

The resulting flow equations have the same structure as the connected Green functions \mathcal{G}^Λ and contain tadpole and tree diagrams. They are obtained by expanding the generating functional $\mathcal{V}^\Lambda[\bar{\chi}, \chi]$ with respect to the Λ -independent source fields $\bar{\chi}, \chi$.

An alternative ansatz is the expansion of $\mathcal{V}^\Lambda[\bar{\chi}, \chi]$ with respect to Wick-ordered polynomials of the source fields χ and $\bar{\chi}$, leading to flow equations for different expansion coefficients, the Wick-ordered m-particle Green functions W_m . Therefore, this approach is called *Wick-ordered Green function flow*. The right-hand side of this flow equation is bilinear in the vertices W_m and consists either of tree diagrams or loop diagrams. The higher loop diagrams are build by the soft-mode propagator that includes all energy modes below Λ . Therefore, the coupling function can be parametrized, for a cutoff in momentum space, by the momenta projected onto the Fermi surface.

The 1PI scheme has the advantage that the internal propagators are full propagators \mathcal{G}^Λ , including the influence of the self-energy up to the energy-scale Λ . Therefore, the most appropriately way to take the corrections of the self-energy into account is this 1PI approach.

Solving the exact renormalization group flow equations for the different fRG schemes lead to the same and exact results of the full interacting model. The different implementations come into play if we perform a certain truncation of these flow equations. If we compare, for example, the Polchinski with the Wick-ordered scheme, the only difference is that the generating functional $\mathcal{V}^\Lambda[\bar{\chi}, \chi]$ is expanded in different orthogonal polynomial sets. Truncating these expansions above a certain coefficient may lead to a drastic discrepancy of the resulting approximations of \mathcal{V}^Λ for each polynomial set. Therefore, the quality of the approximated results depend on the fRG scheme for a certain truncation. In addition, the possibility of an efficient parametrization of the generating functional by a manageable set of variables depends on this choice. We conclude that the appropriate fRG scheme depends on the physical system we want to describe.

Chapter 3

fRG applied to a 2D Hubbard model

In this chapter we derive the static flow equations of the self-energy and the effective interaction for a two-dimensional Hubbard model, representing a contact/interaction region coupled to two semi-infinite leads. This derivation is based on chapter 2 and is analogue to the 1D approach of Bauer [3]. Assuming a quasi-1D system, we use the recursive Green function (RGF) algorithm [47] to compute the diagonal elements of the modified Green functions, which are needed to solve the differential system. By extending the calculation of Karrasch [20], we show that the vertex correction of the linear conductance for the resulting effective system also disappears in 2D, and that the famous non-interacting Landauer formula [11] is applicable. At the end we show how to calculate the local density formulated as an energy integral of the Green function over the imaginary axis.

3.1 Introduction

In the previous chapter we have introduced the functional renormalization group in the 1PI scheme for an interacting Fermi system and derived a closed system of coupled differential equations for the static self-energy and static effective interaction under the physical assumption of vanishing temperature and weak interaction. The solution of this differential system provides a static self-energy for the fully interacting system, which leads to an effective non-interacting system.

In the proceeding chapter we want to use this fRG method to study low-temperature electron transport phenomena in interacting two-dimensional nanostructures. We focus on constrained structures that exhibit only a few open transport channels. In these systems, the charge tends to accumulate at the sample, and the flow of electrons become strongly correlated due to Coulomb interaction and spin-dependent correlations. Hence, the interaction plays a crucial role in the transport behaviour and the Landauer-Büttiker formalism is no longer applicable. In the low-temperature limit, many of these systems cross over to a strong coupling regime where perturbation theory breaks down. A parade example is the Kondo effect in quantum dots or magnetic impurities, where the conductance diverges logarithmically for temperatures below the Kondo temperature T_K . For this example, the

functional renormalization group theory provides good results for equilibrium properties in Anderson models [20, 2]. In the proceeding text, we use this very successful method to study alternative low-dimensional systems, although it is not clear whether these system suffer from a break down of perturbation theory or not.

For this purpose, we use a standard model of transport studies in mesoscopic physics, namely an interacting sample connected to the left and right through non-interacting leads to extended electron reservoirs. To be able to handle this system numerically, we discretise the continuous two-dimensional space using the *method of finite differences* [11] and restrict ourselves to on-site interaction. This leads to a 2D Hubbard model. The resulting fRG flow equations can be derived from the differential system $d/d\Lambda \gamma_1^\Lambda$ and $d/d\Lambda \gamma_2^\Lambda$ of section 2.4.3, where we parametrize the vertex functions by the site indices of the discrete space and the spin of the electrons. An example of an alternative parametrization proceeding in momentum space for a one-dimensional system modelling a single impurity can be found in Andergassen [1]. Due to the complex structure of the vertex functions with respect to the site indices and the resulting computational costs, we have to reduce the dependencies of the vertex functions in the differential flow equations and consider only on-site elements. Therefore, we neglect all long range effects of the interaction in the system, for example Friedel oscillations. For solving these flow equations, we have to compute the diagonal elements of the modified Green function $\tilde{\mathcal{G}}^\Lambda$ of the contact region. In our discrete space and by using the *projection method* [11], this task is equivalent to compute the diagonal of the inverse of a huge sparse matrix. We compute these elements with the *recursive Green function (RGF) algorithm* [47]. Finally, the solution of this static fRG approach provides an effective non-interacting system with $T = 0$. Therefore, we can show that the vertex correction of the linear conductance is zero, and thus it can be calculated with the Landauer-Büttiker formula. At the end of this chapter we show how another interesting physical observable, the local density of the electrons, can be computed in an efficient way.

3.2 2D Hubbard model

At first, we introduce our theoretical model which we want to use for our transport studies. We already mentioned that we consider a contact/interaction region coupled to the left and right to two extended electron reservoirs, which are connected to the sample through non-interacting leads. The purpose of these reservoirs are to provide the system with electrons in equilibrium. Meaning, if an electron enters one of them, it thermalizes at the temperature and chemical potential of the reservoir before it returns to the sample. This is equivalent to the requirement that the electron reservoirs are reflectionless. Therefore, an alternative approach is to dismiss the extended reservoirs at all and just to make the leads reflectionless. We do this by extending the unconnected ends of the leads to infinity, and we obtain semi-infinite leads.

We implement this setup with a two-dimensional Hubbard model, defined on a lattice space, and compute it's Green function on the contact region with the projection method and the surface Green function of the semi-infinite leads. The connection between

this discrete model and a real nanostructure should be revealed by the method of finite differences.

3.2.1 Method of finite differences

The Hamiltonian of a spinless electron in an one-dimensional system, with an arbitrary potential $V(x)$, reads

$$H = -\frac{\hbar^2}{2m} \frac{d^2}{dx^2} + V(x), \quad (3.1)$$

We discretize this model by replacing the continuous one-dimensional space \mathbb{R} by a lattice, which is isomorphic to \mathbb{Z} . Every grid point n of this lattice corresponds to a position x of continuous space. We choose an equidistant discretisation with a lattice parameter a , which has the unit of length, and $x = na$ with $n \in \mathbb{Z}$. Now, we obtain the discretised model by projecting the operators and functions onto this lattice $\{x = na | n \in \mathbb{Z}\}$. The derivation operator d/dx becomes

$$\frac{df(x)}{dx} = \frac{f(x + a/2) - f(x - a/2)}{a}, \quad (3.2)$$

where f is an arbitrary differentiable \mathbb{R} -function. An equation for the second derivative d^2/d^2x follows directly from the first derivative, and we obtain [11, 3.5.5, 3.5.6]

$$(Hf)|_{x=ia} = (2\tau + V_i) f_i - \tau f_{i-1} - \tau f_{i+1} \quad \text{with} \quad \tau = \frac{\hbar^2}{2ma^2}, \quad (3.3)$$

where $f_i = f(x = ia)$ and analogous V_i . This is equivalent, see [11, 3.5.7], to $(Hf)|_{x=ia} = \sum_j H_{i,j} f_j$ with

$$(Hf) \Big|_{x=ia} = \sum_j H_{i,j} f_j \quad \text{with} \quad H_{i,j} := (V_i + 2\tau) \delta_{i,j} - \tau (\delta_{i,j+1} + \delta_{i,j-1}). \quad (3.4)$$

The extension to a higher-dimensional space or to a N -particle Hamiltonian for spinful electrons, including a particle-particle interaction, is straightforward.

In the following, we start straightaway with such a discretised model, namely a two-dimensional Hubbard model. For comparison between our results and approaches in continuous space it is important to keep this translation, especially the formula for τ , in mind. We will always assume that the units in our discretised model are chosen in such a way that $a = 1$.

3.2.2 2D Hubbard model Hamiltonian

We want to model a contact region coupled to the left and right to semi-infinite leads using a two-dimensional Hubbard model in second quantisation. Therefore, our Hamiltonian consists of three main parts

$$\mathcal{H} = \mathcal{H}_{\text{contact}} + \mathcal{H}_{\text{contact-leads}} + \mathcal{H}_{\text{leads}}, \quad (3.5)$$

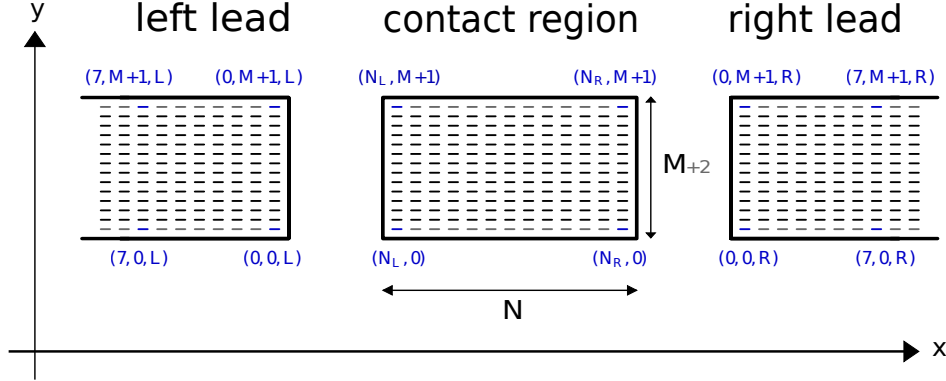


Figure 3.1: Illustration of the 2D Hubbard model. The contact/interaction region is connected to the left and right to semi-infinite leads. The contact region consists of $N = |N_R - N_L|$ sites in x -direction and $M+2$ sites in y -direction. We consider fixed boundary conditions. Hence, the sites $(n, 0)$, $(n, M+1)$ of the contact and $(n, 0, s)$, $(n, M+1, s)$ of the leads are fixed, and the effective width of our system, and the number of transversal modes is M . In blue, we illustrated our notation for some characteristic sites.

where $\mathcal{H}_{contact}$ describes the contact region, \mathcal{H}_{leads} the left and right semi-infinite leads and $\mathcal{H}_{contact-leads}$ the tunneling Hamiltonian between these two subsystems, see figure 3.1. The Hamiltonian of the contact region can itself be separated into three parts

$$\mathcal{H}_{contact} = \mathcal{H}_{contact}^0 + \mathcal{H}_{contact}^{int} = \mathcal{H}_{contact}^{1P} + \mathcal{H}_{contact}^{hop} + \mathcal{H}_{contact}^{int}, \quad (3.6)$$

where $\mathcal{H}_{contact}^{1P}$ is the one-particle part, $\mathcal{H}_{contact}^{hop}$ the hopping between different sites in the contact and $\mathcal{H}_{contact}^{int}$ the interaction within the contact region. Furthermore, the one-particle and hopping part can be summarized to a non-interacting Hamiltonian $\mathcal{H}_{contact}^0$. The quadratic part of the contact Hamiltonian is

$$\mathcal{H}_{contact}^{1P} = \sum_{\sigma=\uparrow,\downarrow} \sum_{n=N_L}^{N_R} \sum_{m=0}^{M+1} \epsilon_{n,m,\sigma} d_{n,m,\sigma}^+ d_{n,m,\sigma}, \quad (3.7)$$

where $d_{n,m,\sigma}^+$, $d_{n,m,\sigma}$ denote respectively the creation and annihilation operators of an electron localized at site (n, m) in the contact region with spin σ and the one-particle energy $\epsilon_{n,m,\sigma}$. In the following, we consider the one-particle energies to be

$$\epsilon_{n,m,\sigma} = -\mu + V_{n,m} + g \frac{\sigma}{2} h_{n,m}, \quad (3.8)$$

where μ is the chemical potential and $V_{n,m}$, $h_{n,m}$ the site-dependent potential, magnetic field evaluated at site (n, m) . The last term in (3.8), the *Zeeman term*, describes the influence of a magnetic field applied to the contact region in direction of the electron current flow. Here g is the dimensionless g -factor and σ the spin projection with respect to the magnetic field, where $\sigma = +/- 1$ denotes a parallel/antiparallel orientation. We also

use the notation $\sigma = \uparrow/\downarrow$ for $\sigma = +/ - 1$. Because the concrete numbering of the sites is arbitrary, we denote the right and left end of the contact as N_R, N_L (we assume $N_L < N_R$), which provides a very compact form of writing down the Hamiltonian. For more details we refer to figure 3.1. The hopping between sites in the contact region is taken into account by the hopping term

$$\mathcal{H}_{contact}^{hop} = - \sum_{\sigma=\uparrow,\downarrow} \left[\begin{aligned} & \tau_x \sum_{n=N_L}^{N_R-1} \sum_{m=0}^{M+1} (d_{n+1,m,\sigma}^+ d_{n,m,\sigma} + d_{n,m,\sigma}^+ d_{n+1,m,\sigma}) \\ & + \tau_y \sum_{n=N_L}^{N_R} \sum_{m=0}^M (d_{n,m+1,\sigma}^+ d_{n,m,\sigma} + d_{n,m,\sigma}^+ d_{n,m+1,\sigma}) \end{aligned} \right], \quad (3.9)$$

where τ_x, τ_y are hopping-matrix elements with respect to longitudinal and transversal transitions. In the following we assume τ_x and τ_y to be real numbers. We implement the Coulomb interaction in the model by inserting a repulsive on-site density-density-interaction

$$\mathcal{H}_{contact}^{int} = \sum_{n=N_L}^{N_R} \sum_{m=0}^{M+1} U_{n,m} n_{n,m,\uparrow} n_{n,m,\downarrow}, \quad (3.10)$$

where $n_{n,m,\sigma} = d_{n,m,\sigma}^+ d_{n,m,\sigma}$ is the spin-resolved local density operator and $U_{n,m}$ the on-site interaction energy. The contact/interaction region is coupled to the non-interacting leads by the tunneling Hamiltonian

$$\mathcal{H}_{contact-leads} = - \sum_{s=L,R} \sum_{\sigma=\uparrow,\downarrow} \sum_{m=0}^{M+1} \tau_x (c_{0,m,\sigma,s}^+ d_{N_s,m,\sigma} + d_{N_s,m,\sigma}^+ c_{0,m,\sigma,s}), \quad (3.11)$$

where the operators $c_{n,m,\sigma,s}^+, c_{n,m,\sigma,s}$ are respectively creation and annihilation operators of an electron localized at site (n, m) of the right or left lead ($s = R, L$) with spin σ . The sites $(0, m, R/L)$ describe the first sites of the right/left lead with respect to the longitudinal direction. Now we are left with the Hamiltonian of the leads, which reads

$$\mathcal{H}_{leads} = - \sum_{s=L,R} \sum_{\sigma=\uparrow,\downarrow} \sum_{n=0}^{\infty} \sum_{m=0}^{M+1} \left[\begin{aligned} & \mu c_{n,m,\sigma,s}^+ c_{n,m,\sigma,s} + \tau_x (c_{n+1,m,\sigma,s}^+ c_{n,m,\sigma,s} + c_{n,m,\sigma,s}^+ c_{n+1,m,\sigma,s}) \\ & + \tau_y (c_{n,m+1,\sigma,s}^+ c_{n,m,\sigma,s} + c_{n,m,\sigma,s}^+ c_{n,m+1,\sigma,s}) \end{aligned} \right]. \quad (3.12)$$

The first term is the one-particle term of the lead Hamiltonian, with the chemical potential of the leads μ , and the second and third term describes the hopping in longitudinal and transversal direction. Here we assume that the hopping elements in the leads are equivalent to the hopping elements in the contact.

Up to now, we formulated the Hamiltonian including the sites $(n, M+1, s)$, $(n, 0, s)$ and $(n, M+1)$, $(n, 0)$. In the following, we assume fixed boundary conditions, in particular that the local electron density of these site is zero. Therefore, no dynamical processes takes place on these site and we will neglect those sites in the proceeding calculations.

3.2.3 Green function of the contact - projection method

The different Green functions of the contact region are important in two ways. First, for solving the fRG flow equations the modified Green function of the contact region $\tilde{\mathcal{G}}^A$ is a central quantity. Here, we only have to consider the restriction to the contact region, because the interaction between the electrons is limited to this area. Second, after we obtain the solution, we still have to compute the desired physical observables, for example the conductance or the local density, of our new effective system. Conceptually, there exists no difference between the calculation of these two classes of Green functions, because only the Hamiltonian of the interaction region changes.

In this subsection we want to derive a numeric evaluable formula for the Green function of the contact region by using the projection method. This approach culminates in the analytically computation of the self-energy Σ_{leads} , which describes the influence of the leads on the contact region.

For a finite-dimensional non-interacting Hubbard model, the corresponding Green function can be calculated under the assumption of a finite dimensional Hilbert space with

$$\mathcal{G}(z) = [z\mathbb{1} - H]^{-1}, \quad (3.13)$$

where z is a complex number and H the corresponding matrix representation, compare [11, chap. 3.3.8]. For our model (3.5), this approach is not directly applicable, because of the infinite dimension of the underlying Hilbert space. Recall, we want to describe a mesoscopic sample coupled to semi-infinite leads. However, we are only interested in the Green function of the contact region, and hence we can use the *projection method* [11, chap. 3.5] to project the influence of the infinite dimensional leads onto the contact region. The result is an effective Hamiltonian of the finite interaction region which takes the influence of the leads into account. And finally the desired Green function can be calculated using (3.13).

To derive this effective Hamiltonian, we define the projection operators P and Q via

$$P = \sum_{n=N_L}^{N_R} \sum_{m=1}^M \sum_{\sigma=\uparrow,\downarrow} |n, m, \sigma\rangle \langle n, m, \sigma|, \quad (3.14)$$

$$Q = \sum_{s=L,R} \sum_{n=1}^{\infty} \sum_{m=1}^M \sum_{\sigma=\uparrow,\downarrow} |n, m, \sigma, s\rangle \langle n, m, \sigma, s|. \quad (3.15)$$

These operators project the states onto the subspace of Hilbert space which describes electrons localized at sites in the contact region or in the leads. The following formulas for the projection operators

$$P^2 = P, \quad Q^2 = Q, \quad P + Q = \mathbb{1}, \quad PQ = QP = 0 \quad (3.16)$$

hold. We introduce the useful abbreviation $A_{XY} := XAY$ and $A_X := XAX$ with A, X, Y arbitrary operators. Now we can split the Hamiltonian into the following parts

$$H_P = H_{contact}, \quad H_Q = H_{leads} \quad \text{and} \quad H_{contact-leads} = H_{PQ} + H_{QP}, \quad (3.17)$$

where H_{PQ} , H_{QP} describes the lead-contact, contact-lead hopping. Furthermore, we used the notation H_{\dots} for the corresponding single-particle Hamiltonian of \mathcal{H}_{\dots} , which was formulated in second quantisation. Using these definitions, equation (3.13) is equivalent to

$$\mathcal{G}(z) = \left[z\mathbb{1} - \begin{pmatrix} H_P & H_{PQ} \\ H_{QP} & H_Q \end{pmatrix} \right]^{-1}. \quad (3.18)$$

Analogously, we can split the Green function $\mathcal{G}(z)$ and rearrange the formula in the following way

$$\begin{pmatrix} zP - H_P & -H_{PQ} \\ -H_{QP} & zQ - H_Q \end{pmatrix} \begin{pmatrix} \mathcal{G}_P(z) & \mathcal{G}_{PQ}(z) \\ \mathcal{G}_{QP}(z) & \mathcal{G}_Q(z) \end{pmatrix} = \mathbb{1}. \quad (3.19)$$

This matrix equation includes, among others,

$$(zP - H_P)\mathcal{G}_P(z) - H_{PQ}\mathcal{G}_{QP}(z) = \mathbb{1}, \quad (3.20)$$

and

$$-H_{QP}\mathcal{G}_P(z) + (zQ - H_Q)\mathcal{G}_{QP}(z) = 0. \quad (3.21)$$

By using equation (3.21) follows

$$\mathcal{G}_{QP} = \frac{1}{zQ - H_Q} H_{QP}\mathcal{G}_P(z), \quad (3.22)$$

and with equation (3.20) we already get our main result, the Green function of the contact region

$$\begin{aligned} \mathcal{G}_P(z) &= \frac{1}{zP - H_P - H_{PQ} \frac{1}{zQ - H_Q} H_{QP}} \\ &= \frac{1}{zP - H_P - \Sigma_{leads}}, \end{aligned} \quad (3.23)$$

where we defined the self-energy as follows

$$\Sigma_{leads}(z) := H_{PQ} \frac{1}{zQ - H_Q} H_{QP}. \quad (3.24)$$

If we compare this result with the naive approach of just neglecting the leads, we can observe that the whole influence of the leads is given by the replacement of the contact Hamiltonian $H_P \rightarrow H_P + \Sigma_{leads}$. Because we still have to compute the inverse of an infinite-dimensional matrix to obtain Σ_{leads} , the question might occur what benefit we have gained with this reformulation. Fortunately, we can derive an analytical formula for $\Sigma_{leads}(z)$ for most of the commonly used lead geometries, including the leads of our model.

For the computation of the conduction in section 3.4.1, we need analogous equations for $\mathcal{G}_{PQ}(z)$ and $\mathcal{G}_Q(z)$. We don't present this tedious derivation at this point and refer to appendix A instead. The results are

$$\mathcal{G}_{PQ}(z) = \mathcal{G}_P(z) H_{PQ} \frac{1}{zQ - H_Q}, \quad (3.25)$$

and

$$\mathcal{G}_Q(z) = \frac{1}{zQ - H_Q} + \frac{1}{zQ - H_Q} H_{QP} \mathcal{G}_P(z) H_{PQ} \frac{1}{zQ - H_Q}. \quad (3.26)$$

Now we want to derive an analytical formula of the self-energy Σ_{leads} for our model. At first we express the self energy in a more suitable form by using the equation (3.14), (3.15),

$$\begin{aligned} \Sigma_{leads}(z) &= H_{PQ} \frac{1}{zQ - H_Q} H_{QP} \\ &= \sum_{s,s'} \sum_{n,n'} \sum_{m,m'} \sum_{\sigma,\sigma'} (\tau_x^2 |N_s, m, \sigma\rangle \langle 1, m, \sigma, s| (zQ - H_Q)^{-1} |1, m', \sigma', s'\rangle \langle N_{s'}, m', \sigma'|) \\ &= \sum_s \sum_{n,n'} \sum_{m,m'} \sum_{\sigma} (\tau_x^2 |N_s, m, \sigma\rangle \langle 1, m, \sigma, s| (zQ - H_Q)^{-1} |1, m', \sigma, s\rangle \langle N_s, m', \sigma|). \end{aligned} \quad (3.27)$$

The last equation holds, because the two leads are not connected and the Hamiltonian is diagonal in spin space, therefore $\langle n, m, \sigma, s|H|n', m', \sigma', s'\rangle \propto \delta_{s,s'} \delta_{\sigma,\sigma'}$. We can identify the surface Green function of the right and left lead respectively, which are defined by

$$g_{1,m,1,m'}^{\sigma,s}(z) := \langle 1, m, \sigma, s| (zQ - H_Q)^{-1} |1, m', \sigma, s\rangle, \quad (3.28)$$

where we use the abbreviation $g_{m,m'}^{\sigma,s}(z) := g_{1,m,1,m'}^{\sigma,s}(z)$. The corresponding matrix elements of Σ_{leads} are as follows

$$\begin{aligned} [\Sigma_{leads}]_{n,m;n',m'}^{\sigma}(z) &:= \langle n, m, \sigma | \Sigma_{leads}(z) | n', m', \sigma \rangle \\ &= \sum_s \delta_{n,N_s} \delta_{n',N_s} \langle N_s, m, \sigma | \Sigma_{leads}(z) | N_s, m', \sigma \rangle \\ &= \sum_s \delta_{n,N_s} \delta_{n',N_s} \tau_x^2 g_{m,m'}^{\sigma,s}(z) \end{aligned} \quad (3.29)$$

and we define

$$[\Sigma_{lead}]_{n,m;n',m'}^{\sigma,s}(z) := \delta_{n,N_s} \delta_{n',N_s} \tau_x^2 g_{m,m'}^{\sigma,s}(z). \quad (3.30)$$

This is the main result of the projection method. This enables us to eliminate the infinite leads and expressed the Green function in terms of quantities that are defined inside the contact region. Even the self-energy Σ_{leads} , describing the effect of the leads, is evaluated at the points (N_s, m) , (N_s, m') that are located inside the contact region. Therefore, we are left to calculate the surface Green functions of the leads to determine the Green function of the contact region.

Calculation of the surface Green function of the leads

In the following, we want to derive an explicit expression for the surface Green function of the leads, which is the Green function of the leads evaluated at the sites that connect

the leads with the contact region. For this purpose, we use the well known fact that every Green function can be expanded in a set of complete eigenfunctions, compare [11, equ. 3.3.17, 3.3.20],

$$\mathcal{G}(\mathbf{r}, \mathbf{r}'; z) = \sum_{\alpha} \frac{\psi_{\alpha}(\mathbf{r})\psi_{\alpha}^*(\mathbf{r}')}{z - E_{\alpha}}, \quad (3.31)$$

where $H\psi_{\alpha} = E_{\alpha}\psi_{\alpha}$ and z is a complex number. In our case, treating a discrete space, the continuous variables \mathbf{r}, \mathbf{r}' are integers describing certain grid points in our lattice. This ansatz is very useful to derive a formula of the desired Green function, because the leads are assumed to be non-interacting and the geometry is well treatable. Hence, the eigenfunctions of the leads are easily accessible, and we are left to perform the summation in the latter equation.

For our system the leads are wires with a constant width. As a consequence the x - and y -direction are independent and the eigenfunctions are separable. This comes from the fact, that the Hamiltonian H_{leads} can be expressed as a tensor product $H_{leads} = H_{leads}^x \otimes H_{leads}^y$, where $H_{leads}^{x/y}$ describes the x/y -direction of the leads separately. So we have to provide the eigenfunctions of a tight-binding chain with semi-infinite and finite extension, in explicit terms, we have to solve $H_{leads}^x\psi_{x,\alpha} = E_{x,\alpha}\psi_{x,\alpha}$ and $H_{leads}^y\psi_{y,\beta} = E_{y,\beta}\psi_{y,\beta}$. Then

$$g_{n,m,n',m'}^{\sigma,s}(z) = \sum_{\alpha} \sum_{\beta} \frac{\psi_{x,\alpha}(n)\psi_{y,\beta}(m)\psi_{x,\alpha}^*(n')\psi_{y,\beta}^*(m')}{z - E_{x,\alpha} - E_{y,\beta}} \quad (3.32)$$

evaluated at $n = n' = 1$ gives the desired result for the Green function of the leads on the surface to the contact region $g_{m,m'}^{\sigma,s}$ ¹. In our model, the left and right leads are identical, and hence, the index s is meaningless for the surface Green function. The same holds for the spin index σ , because we apply a magnetic field only to the contact region, and hence, the self-energy/surface Green functions of the leads for spin up and spin down electrons are equivalent. Therefore, we skip these two indexes in the following.

First of all, we solve this problem for a semi-infinite tight-binding chain that leads to the Green function of a one dimensional semi-infinite tight-binding chain, denoted \tilde{g} , evaluated at the last site. This Green function can be obtained very fast by a vague symmetry argument which exploits the infinite extension of the chain, see for example [13, p. 55 ff.]. In this thesis, we will stick to the general proceeding and use the expansion of the Green function in eigenfunctions (3.31), compare [31, app. 1c] and [12, ch. 5.3.1]. Therefore, we use that the eigenvalues of a tight-binding chain of the form

$$H_{TB} = -\mu \sum_{n=0}^{N+1} |n\rangle\langle n| - \tau \sum_{n=0}^N (|n\rangle\langle n+1| + |n+1\rangle\langle n|) \quad (3.33)$$

with length $N + 1$ are given by

$$E_{k_{\alpha}} = -\mu - 2\tau \cos(k_{\alpha}) \quad \text{with} \quad k_{\alpha} = \frac{\alpha\pi}{N+1}, \quad (3.34)$$

¹At this point we would like to remind of the abbreviation $g_{m,m'}^{\sigma,s} := g_{1,m;1m'}^{\sigma,s}$ for the surface Green function of the leads.

see [22, equ. 5.11, 5.12], and the associated eigenfunctions are given by

$$\psi_{k_\alpha}(n) = \sqrt{\frac{2}{N+1}} \sin(k_\alpha n), \quad \alpha \in \{1, \dots, N\} \quad (3.35)$$

for fixed boundary conditions, in explicit terms $\psi_{k_\alpha}(0) = \psi_{k_\alpha}(N+1) = 0$. We choose fixed boundary conditions, because we can argue that the concrete values of the eigenfunctions at the boundary of a chain with infinite length shouldn't influence the physics and, hence, the Green function of this chain at all. By this choice, the arising integrals become easier to solve. In the limit $N \rightarrow \infty$ the wave vector k_α becomes a continuous variable and the summation (3.31) an integral

$$\begin{aligned} \tilde{g}_{n,n'}(z) &= \frac{2}{\pi} \int_0^\pi dk \frac{\sin(kn) \sin(kn')}{z + 2\tau \cos(k) + \mu} \\ &\stackrel{n=n'=1}{=} \frac{1}{4\pi\tau} \int_{-\pi}^\pi d\xi \frac{1 - e^{2i\xi}}{\chi + \cos(\xi)}, \end{aligned} \quad (3.36)$$

where $\xi = kn$ and $\chi = (z + \mu)/2\tau$. Here we restricted ourselves to the case $n = n' = 1$, because we are only interested in the values at the boundary, hence at the first site of the chain. The arising integral can be solved by its transformation to a contour integral in the complex plain along the unit circle \mathcal{S}_1

$$\tilde{g}(z) = \frac{1}{4\pi\tau} \int_{\mathcal{S}_1} \frac{dv}{iv} \frac{1 - v^2}{\chi + \frac{1}{2} \left(v + \frac{1}{v}\right)}, \quad (3.37)$$

where we used the substitution $v = e^{i\xi}$. The resulting integrand has simple poles at $v_{1/2} = -\chi \pm \sqrt{\chi^2 - 1}$, where the square root sign is chosen in such a way that the sign of $\text{Im}\{\sqrt{\chi^2 - 1}\}$ is equivalent to the sign of $\text{Im}\{\chi\}$. The poles fulfil the relation $v_1 \cdot v_2 = 1$ and it can quite easily be shown, we refer to appendix B, that in the case $\text{Im}\{z\} \neq 0$ the inequalities $|v_1| < 1$ and $|v_2| > 1$ hold. Therefore, the poles $v_{1/2}$ don't lie on the contour \mathcal{S}_1 , and we can apply the residue theorem. For a vanishing imaginary part $\text{Im}\{\chi\}$, we can evaluate the integral by performing a limit $z + i0^\pm$. A short calculation shows that the residues of $f(z) := (1 - v^2)/2\pi\tau i (v^2 + 2\chi v + 1)$ are

$$\text{Res}_{z=v_{1/2}} [f(z)] = \frac{1}{2\pi i \tau} \left(\chi \mp \sqrt{\chi^2 - 1} \right), \quad (3.38)$$

and the residue theorem provides

$$\tilde{g}(z) = \frac{1}{\tau} \left(\chi - \sqrt{\chi^2 - 1} \right), \quad (3.39)$$

where we emphasize that the square root sign depends on $\text{Im}\{\chi\}$. An equivalent expression for $\tilde{g}(z)$, if $\text{Im}\{\chi\} \neq 0$, can be obtained by defining the poles $v_\pm := -\chi \pm \sqrt{\chi^2 - 1}$, and the

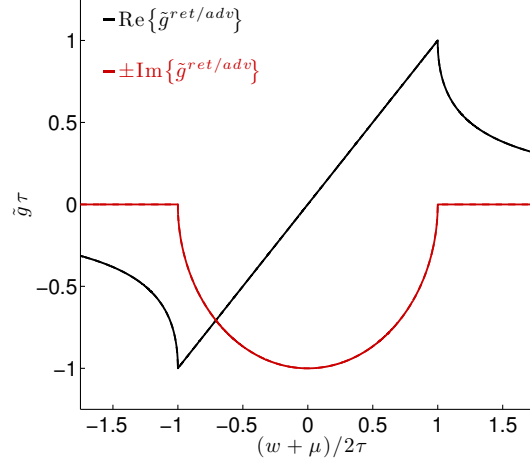


Figure 3.2: Retarded and advanced surface Green functions versus energy over half-bandwidth 2τ for a 1D semi-infinite chain.

residue theorem provides ²

$$\tilde{g}(z) = \frac{1}{\tau} \left(\chi \mp \sqrt{\chi^2 - 1} \right) \quad \text{if } |-\chi \pm \sqrt{\chi^2 - 1}| < 1, \quad (3.40)$$

where $\sqrt{}$ denotes the positive square root. Another widely used formula for the surface Green function of the 1D semi-infinite leads is

$$\tilde{g}(z) = \begin{cases} \frac{1}{\tau} \left(\chi - i\sqrt{1 - \chi^2} \right), & \text{if } \text{Im}\{\chi\} > 0 \\ \frac{1}{\tau} \left(\chi + i\sqrt{1 - \chi^2} \right), & \text{if } \text{Im}\{\chi\} < 0 \end{cases}, \quad (3.41)$$

compare [13, 20, equ. 4.2, 3.17], where $\sqrt{}$ denotes the positive square root. The equivalence between (3.41) and (3.39) is shown in appendix B.

For the computation of the retarded and advanced Green function, formula (3.39) is more useful. We can use $\text{Im}\{\sqrt{\chi^2 - 1}\} = 2 \text{Im}\{\chi\} \text{Re}\{\chi\}$ for the positive square root and the representation of the square root in cartesian coordinates [50, chap. 1.2.2 formula 9], to write \tilde{g} into the following form

$$\tilde{g}(z) = \frac{1}{\tau} \left(\chi - \frac{\chi_r}{|\chi_r|} \sqrt{1/2(\chi_r + |\chi|)} - i \frac{\chi_i}{|\chi_i|} \sqrt{1/2(-\chi_r + |\chi|)} \right), \quad (3.42)$$

where $\chi = \chi_r + i\chi_i$ with $\chi_r, \chi_i \in \mathbb{R}$. After performing the limit $\tilde{g}(w + i0^\pm)$, we obtain the retarded and advanced surface Green functions of the 1D semi-infinite leads

$$\tilde{g}^{ret/adv}(w) = \frac{1}{\tau} \left(\chi_r - \frac{\chi_r}{|\chi_r|} \sqrt{\chi_r^2 - 1} \Theta(\chi_r^2 - 1) \mp i \sqrt{1 - \chi_r^2} \Theta(1 - \chi_r^2) \right), \quad (3.43)$$

where $\chi_r = (w + \mu)/2\tau$. Figure 3.2 shows the imaginary and real part of the retarded and advanced Green functions.

²Under the assumption $\text{Im}\chi \neq 0$, the inequalities $|v_+| \leq 1$ and $|v_-| \geq 1$ follows directly from $|v_1| < 1$ and $|v_2| > 1$.

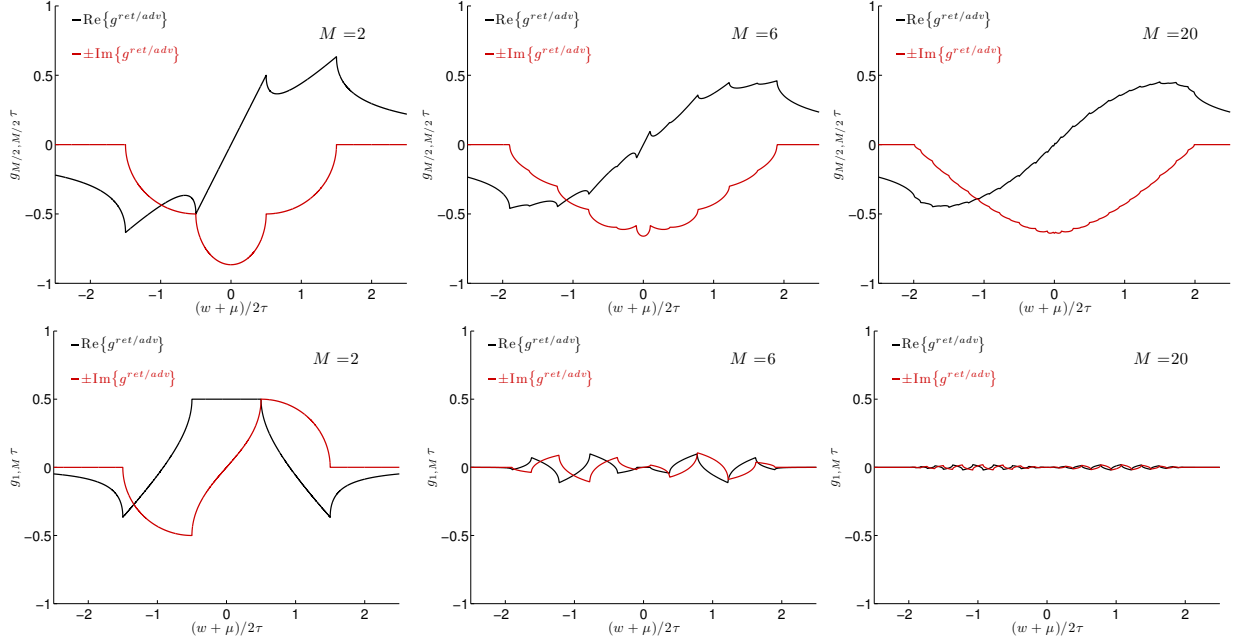


Figure 3.3: Retarded and advanced surface Green functions versus energy over half-subbandwidth 2τ for a 2D semi-infinite chain. The constant effective width M of the chain changes from left to right, where $M = 2, 6$ and 20 . In the upper panels we plotted the element $(M/2, M/2)$ and in the bottom panels $(1, M)$.

With this result the main goal, namely to calculate the surface Green function of the 2D semi-infinite leads with finite effective width M , is easily attainable. We have to perform the summation

$$g_{m,m'}(z) = \sum_{\beta} \underbrace{\sum_{\alpha} \frac{\psi_{x,\alpha}(1)\psi_{x,\alpha}^*(1)}{z - E_{x,\alpha} - E_{y,\beta}}}_{\tilde{g}(\tilde{z}_{\beta})} \psi_{\beta,y}(m)\psi_{y,\beta}^*(m'), \quad (3.44)$$

over the transversal eigenfunctions $\psi_{y,\beta}(m) = \psi_{k_{\beta}}(m)$ of a finite tight-binding chain with fixed boundary conditions and its corresponding eigenvalues $E_{y,\beta} = E_{k_{\beta}}$ ³, see equation (3.35) and (3.34). Here, we defined $\tilde{z}_{\beta} := z - E_{y,\beta} = z + \mu + 2\tau \cos(k_{\beta})$. Finally, this leads to

$$g_{m,m'}(z) = \frac{2}{M+1} \sum_{\beta=1}^M \tilde{g}(z + 2\tau_y \cos(k_{\beta})) \sin(k_{\beta}m) \sin(k_{\beta}m'). \quad (3.45)$$

With the result of the retarded and advanced Green functions $\tilde{g}^{ret/adv}$, we immediately

³For alternative boundary conditions or transversal confinements, instead of the hard-wall potential, we have to perform the sum in equation (3.44) with respect to the corresponding $\psi_{\beta,y}$ and $E_{y,\beta}$.

obtain the corresponding retarded and advanced Green functions

$$g_{m,m'}^{ret/adv}(w) = \frac{2}{M+1} \sum_{\beta=1}^M \tilde{g}^{ret/adv}(w + 2\tau_y \cos(k_\beta)) \sin(k_\beta m) \sin(k_\beta m'). \quad (3.46)$$

In figure 3.3, we plotted the retarded and advanced Green function $g_{m,m'}$ for various effective widths M , in each case for a diagonal and an off-diagonal element.

We conclude this part by giving the final formula of the matrix elements for the self-energy of the two semi-infinite leads with finite effective width M

$$\begin{aligned} [\Sigma_{leads}]_{m,m'}^\sigma(z) &= \sum_s [\Sigma_{lead}]_{m,m'}^{\sigma,s}(z) = \sum_s \delta_{n,N_s} \delta_{n',N_s} \tau_x^2 g_{m,m'}^{\sigma,s}(z) \\ &= \sum_s \delta_{n,N_s} \delta_{n',N_s} \tau_x^2 \frac{2}{M+1} \sum_{\beta=1}^M \tilde{g}(z + 2\tau_y \cos(k_\beta)) \sin(k_\beta m) \sin(k_\beta m'), \end{aligned} \quad (3.47)$$

compare equation (3.29) and (3.30). Using this result, we can easily compute the Green function of the contact region by applying the projection method and equation (3.23).

Physical interpretation of the self-energy

Before we conclude this section, we want to give a short physical interpretation of the self-energy based on [11, chap. 3.6] and [7, chap. 9.2].

By using the projection method, we mapped the influence of the leads onto the contact region and obtained a modified contact Hamiltonian $H_{contact} + \Sigma_{leads}$, where the self-energy Σ_{leads} describes the influence of the leads. This self-energy is in general not hermitian, and therefore the eigenvalues in general not real, which is in contrast to the contact Hamiltonian. We denote the eigenstates of the modified contact Hamiltonian $|\psi_\alpha\rangle$ and the corresponding eigenvalues $\epsilon_\alpha, \varsigma_\alpha$ by

$$H_{contact}|\psi_\alpha\rangle = \epsilon_\alpha|\psi_\alpha\rangle \quad \text{and} \quad \Sigma_{leads}|\psi_\alpha\rangle = -\varsigma_\alpha|\psi_\alpha\rangle. \quad (3.47)$$

By using the definition $\varsigma_\alpha = \varsigma_\alpha^r + i\varsigma_\alpha^i$ with $\varsigma_\alpha^r, \varsigma_\alpha^i \in \mathbb{R}$, the Green function of the contact region becomes

$$\mathcal{G}_{\alpha,\alpha}(z) = \frac{1}{z - (\epsilon_\alpha - \varsigma_\alpha^r) + i\varsigma_\alpha^i}, \quad (3.48)$$

and the spectral function [11, equ. 3.6.3]

$$\mathcal{A}_{\alpha,\alpha}(w) = -2 \text{Im}\{G_{\alpha,\alpha}^{ret}(w)\} = \frac{2\varsigma_\alpha^i}{(w - \epsilon_\alpha + \varsigma_\alpha^r)^2 + (\varsigma_\alpha^i)^2}. \quad (3.49)$$

We observe, the poles z_α^p of the Green function change $z_\alpha^p \rightarrow z_\alpha^p - \varsigma_\alpha$ and may become considerable imaginary. Therefore, the energy levels are shifted by $-\varsigma_\alpha^r$ and the spectral

function broadens, where the width of this broadening is ς_α^i . It is common to describe this broadening with the matrix Γ_{lead} , defined as follows

$$[\Gamma_{lead}]_{n,m;n',m'}^{\sigma,s}(z) := i \left([\Sigma_{lead}]_{n,m;n',m'}^{\sigma,s}(z) - [\Sigma_{lead}^\dagger]_{n,m;n',m'}^{\sigma,s}(z) \right), \quad (3.50)$$

which we will use in section 3.4.1 more extensively. In the time domain, we can determine the time evolution of the eigenstate $|\psi_\alpha\rangle$, that yields

$$|\psi_\alpha(t)\rangle = e^{-i/h(\epsilon_\alpha - \varsigma_\alpha^r)t} e^{-\varsigma_\alpha^i/ht} |\psi_\alpha(0)\rangle \quad (3.51)$$

under the assumption of a time-independent Hamiltonian. The imaginary part of ς_α leads to an exponential decrease of the probability density $|\psi_\alpha|^2$ and, hence, reflects a finite lifetime of this eigenstate. In a more vivid sense, this can be understood as the possibility of an electron in the contact region to escape into one of the leads. In the case of an effective width $M > 1$, the self-energy has off-diagonal entries with respect to the sites on the surface to the left or right lead. This can be understood by the possibility of an electron to propagate through a lead from one site of the surface to another.

3.2.4 Infinite tight-binding chain

Before we explain how the fRG approach can be implemented to study the influence of a repulsive interaction in a two-dimensional system, we want to discuss the non-interacting case. Our main concern is to understand the band structure of our model, which shouldn't change too much for small interaction strengths and which is essential for all electronic transport properties.

In the following, we set $U_{n,m}$ to zero and neglect the Zeeman term in our Hamiltonian (3.5). Therefore, the spin-up and spin-down electrons are degenerated and we dismiss this quantum number in the further calculations of the spectral function and the density of states. Including the spin would only lead to an overall factor of two. In the last section we have calculated the surface Green function/self-energy of a semi-infinite lead with finite width, see equation (3.46), and discussed the projection method to calculate the Green function of the contact region. Starting from this point, it is easy to obtain the spectral function by using [11, equ. 3.6.3]

$$\mathcal{A}(w) = i [G^{ret}(w) - G^{adv}(w)] = -2 \text{Im}\{G^{ret}(w)\}, \quad (3.52)$$

where the retarded Green function of the contact region is denoted G^{ret} , and the density of states (DOS) by using [11, equ. 3.6.12]

$$D(w) = \frac{1}{2\pi} \text{Tr}\{\mathcal{A}(w)\}. \quad (3.53)$$

At first we want to consider a translational invariant infinite tight-binding chain with no external potential applied to it and discuss the influence of a potential on the density of states and the conductance afterwards.

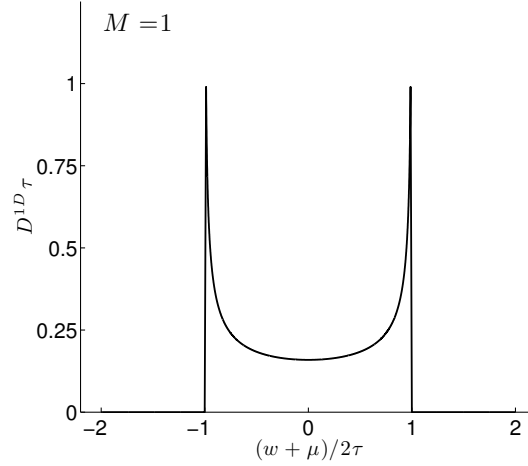


Figure 3.4: Density of states versus energy over half-bandwidth 2τ for a 1D infinite translational invariant tight-binding chain.

Translational invariant infinite tight-binding chain

In the case of a translational invariant infinite tight-binding chain with no external potential applied to it, we can easily calculate an analytical formula for the spectral function and the density of states. Due to the translational invariance of the system, we can define any subsystem as the contact region and choose the smallest invariant part, which is for $M = 1$ a single site and for $M > 1$ a stripe of transversal oriented sites. For $M = 1$ the retarded Green function of an arbitrary site reads

$$G^{ret}(w) = \frac{1}{w + i0^+ + \mu - \underbrace{2\tau^2 \tilde{g}^{ret}(w)}_{\Sigma_{leads}(w+i0^+)}}. \quad (3.54)$$

After a short calculation we obtain the spectral function of an one-dimensional infinite translational invariant tight-binding chain

$$\mathcal{A}^{1D}(w) = \frac{1}{\tau} \frac{1}{\sqrt{1 - \chi_r^2}} \Theta(1 - \chi_r^2) \quad \text{with} \quad \chi_r = \frac{w + \mu}{2\tau}. \quad (3.55)$$

The corresponding density of states $D^{1D} = 1/2\pi \mathcal{A}^{1D}$ can be seen in figure 3.4, and its structure can be understood as follows. With equation (3.35) we have already calculated the eigenvalues of a finite tight-binding chain with N sites, where the corresponding N eigenvalues are discrete and located between $-\mu - 2\tau$ and $-\mu + 2\tau$. For an increasing number of sites, the eigenvalues become more and more dense in this interval, and, in the limit $N \rightarrow \infty$ we end up with the continuous spectrum $[-\mu - 2\tau, -\mu + 2\tau]$, as can be seen in the latter figure.

For a tight-binding chain with an effective width $M > 1$, we choose a stripe of transver-

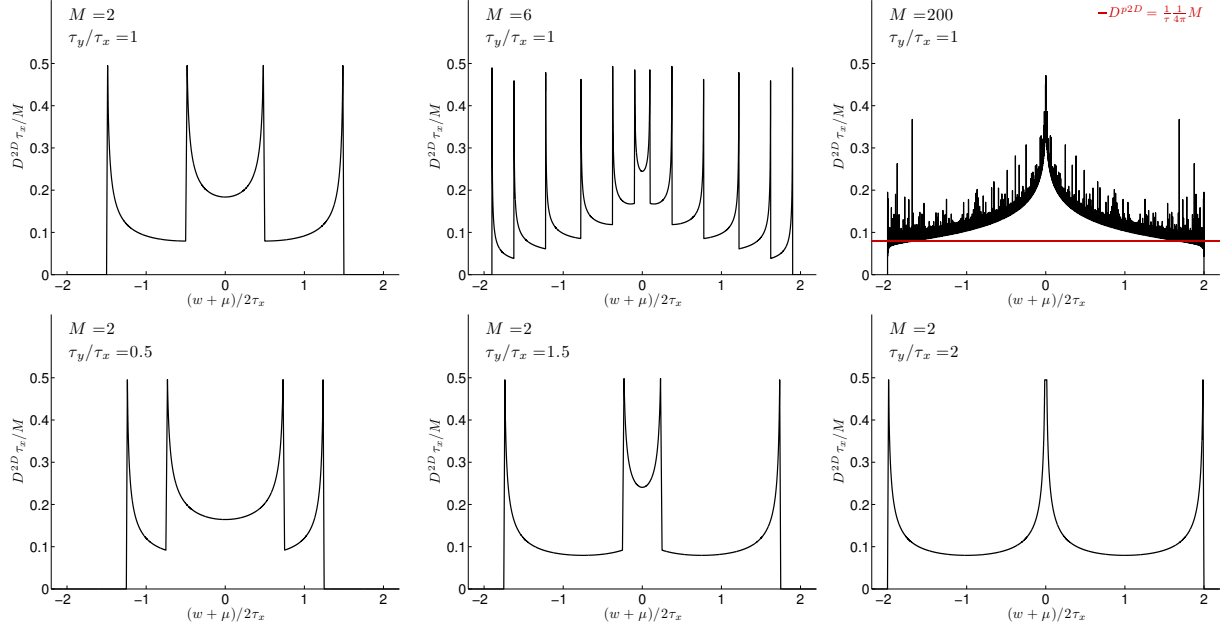


Figure 3.5: Normalized density of states versus energy over half-subbandwidth $2\tau_x$ for a 2D infinite tight-binding chain. Here the longitudinal hopping is always one, $\tau_x = 1$. Upper panels: the effective width M increases from left to right, with $M = 2, 6$ and 50 , for fixed ratio $\tau_y/\tau_x = 1$. The red line in the right panel is the DOS for a pure two-dimensional system, compare [18, equ. 7.10]. Bottom panels: the effective width $M = 2$ is fixed and the ratio τ_y/τ_x increases from left to right, with $\tau_y/\tau_x = 0.5, 1.5$ and 2.0 .

sal oriented sites, represented by the Hamiltonian

$$H^{stripe} = \begin{pmatrix} -\mu & -\tau_y & & & \\ -\tau_y & \ddots & \ddots & & \\ & \ddots & \ddots & -\tau_y & \\ & & & -\tau_y & -\mu \end{pmatrix}. \quad (3.56)$$

The retarded Green function of such a cross-section of the chain yields

$$G^{ret}(w) = \frac{1}{(w + i0^+) \mathbb{1} - H^{stripe} - \underbrace{2\tau_x^2 g^{ret}(w)}_{\Sigma_{leads}(w+i0^+)}} \quad (3.57)$$

and, with the spectral function of a one-dimensional chain, we can easily calculate the spectral function of the two-dimensional system by performing a simple basis transformation to the transversal eigenfunctions, we refer to appendix C. Thereby we obtain the spectral function of an infinite translational invariant tight-binding chain with finite effective width

M , which reads

$$\mathcal{A}_{m,m'}^{2D}(w) = \frac{1}{\tau_x} \frac{2}{M+1} \sum_{\beta=1}^M \frac{1}{\sqrt{1 - \tilde{\chi}_{r,\beta}^2}} \Theta(1 - \tilde{\chi}_{r,\beta}^2) \sin(k_\beta m) \sin(k_\beta m'), \quad (3.58)$$

where

$$\tilde{\chi}_{r,\beta} := \frac{w + \mu}{2\tau_x} + \frac{\tau_y}{\tau_x} \cos(k_\beta) \quad \text{and} \quad k_\beta = \frac{\beta\pi}{M+1}. \quad (3.59)$$

The corresponding normalized density of states, for various widths and changing ratios of hopping elements, can be seen in figure 3.5. The effective width, and hence the number of transversal modes is obviously equivalent to the number of occurring subbands. These subbands are ranging from $-\mu - 2\tau_y \cos(k_\beta) - 2\tau_x$ to $-\mu - 2\tau_y \cos(k_\beta) + 2\tau_x$, where the subband bandwidth is $4\tau_x$ and $\beta \in \{1, \dots, M\}$. Whether those are overlapping or not depends on the relative subband-index $\beta/(M+1)$ and the ratio τ_y/τ_x .

In the limit $\tau_y/\tau_x \rightarrow 0$, the single one-dimensional infinite tight-binding chains are completely decoupled, no transversal hopping occurs, and each subband provides the one-dimensional spectral function \mathcal{A}^{1D} . In the other limit, $\tau_y/\tau_x \rightarrow \infty$, the difference of eigenenergies of the transversal modes is so huge, that the bandwidth $4\tau_x$ becomes infinitesimal small with respect to the energy splitting and we end up with an effective discrete spectrum. This limit corresponds to the case of decoupled transversal finite tight-binding chains. For a rather wide chain $M \gg 1$, see the upper right panel of figure 3.5 for $M = 200$, we are far away from a pure two-dimensional system with a constant DOS, this even holds for $M > 1000$. For implementing such a system, we would have to add additional leads in transversal direction.

Non-translational invariant tight-binding chain

Now, we apply an external smooth potential with a hard-wall potential in transversal direction to the contact region of our infinite tight-binding chain. In this case, it is much more involved to derive an analytical expression of the spectral function, and hence we compute it only numerically. Due to the potential, the bandstructure of the contact region bands along the direction of the potential. For an one-dimensional chain the bandstructure along the contact region becomes just a tube where the DOS of every site n has the form $1/2\pi \mathcal{A}^{1D}$ centered around $\mu + V_n$, see the upper panels a) - c) of figure 3.6 or [3, fig. 4.3]. For finite widths $M > 1$, the behaviour of the bandstructure is the same, see the bottom panels d) - f) of figure 3.6. The two overlapping bands are just following the smooth potential, and every cross-section n of the chain has the same DOS, D^{2D} , shifted by the local potential V_n .

With these bandstructures, we can easily understand the influence of an external potential on the conductance, compare [3, chap. 4.1.1]. We restrict ourselves to the case of zero temperature, zero bias voltage and no other excitations. Therefore, the band is filled up to the Fermi energy $-\mu$, and only electrons with $w = -\mu$ contribute to the conductance. By applying a potential to the contact region, the bandstructure curves along the

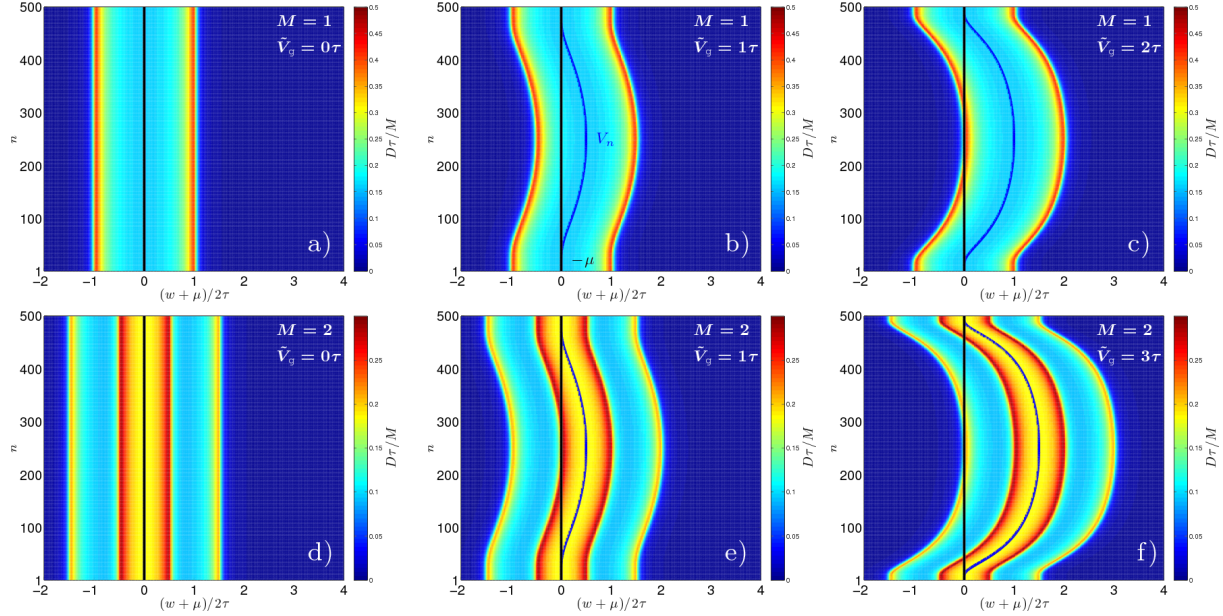


Figure 3.6: Normalized density of states as a function of energy over 1D half-bandwidth 2τ and transversal position n for an infinite tight-binding chain with a smooth potential applied to the contact region, compare [3, fig. 4.3]. The black line denotes the chemical potential $-\mu$ and the blue line the potential V_n applied to the contact region, which spreads over $n = 1$ to $n = 500$. In the upper, bottom panels the width $M = 1, 2$ is fixed and the potential height \tilde{V}_g varies. The hopping elements in transversal and longitudinal direction are equivalent $\tau := \tau_x = \tau_y = 1$.

potential, and, for a certain height $\tilde{V}_g^{0,(\beta)}$, the lower band edge of the subband β gets over the Fermi energy, such that no states are left to mediate the electron current flow in this region and the subband doesn't contribute any longer to the conductance. Because the bandstructure has this nice property with respect to the potential, we explained above, the critical height, where the band β doesn't contribute any longer to the conductance, is the half-subbandwidth

$$\tilde{V}_g^{0,(\beta)} = \mu + 2\tau_x + 2\tau_y \cos(k_\beta), \quad (3.60)$$

which becomes $2\tau_x$ for $M = 1$. In the panels c), e) and f) of figure 3.6, we plotted the DOS at the corresponding critical values $\tilde{V}_g^{0,(\beta)}$ for $M = 1$ and $M = 2$. But be careful, in the panels d) - f) represents the red, orange region in the middle not a subband. It is only the region, where the two subbands overlap. But, the end of this region is also the end of one of the overlapping subbands.

3.3 fRG flow equations

In this section we want to apply the functional Renormalization group to take the repulsive interaction between electrons in the contact region of our two-dimensional Hubbard model into account. Therefore, the main goal is to set up the fRG flow equations for our special

problem and to show how these equations can be solved in a numerically efficient way. In these equations the Green functions of the contact region, we discussed how to calculate them in the last section, and its numerical computation plays a central role.

The differential equations for an one-dimensional extended Hubbard model was already derived in the master thesis of Bauer [3]. We will follow this derivation and show how this approach can be modulated for a two-dimensional system. To be able to treat a system with a great number of grid points, we restrict ourselves to on-site interaction in our model. But we will go even further and demand, by neglecting all other vertex functions, that the effective two-particle interaction between two electrons propagating in our many-body system is also just an on-site interaction. In other words, we will neglect all long range effects of the interaction that are mediated by other electrons in the system, for example Friedel oscillations. This approximation will greatly simplify the structure of the flow equations and strongly reduce the computational costs.

To solve the arising differential equations we need to compute the diagonal parts of the modified Green function of the contact region in an efficient way. We will show how this can be done using the recursive Green function technique.

3.3.1 Resulting fRG flow equations

With the differential equations (2.46), (2.47) and the initial conditions (2.51), (2.52) in chapter 2, we have derived general expressions for the zero-frequency fRG flow equations in the 1PI scheme for an arbitrary two-particle interaction. To obtain these results, we have assumed that the interaction is small and neglected all vertex functions that are of order three or higher in the interaction.

To apply our fRG approach to the 2D Hubbard model, we have to substantiate the parametrization of the vertex functions. We choose, analogously to [3], $l = (j, \sigma)$ for the single-particle quantum number of the resulting flow equations, see section 2.4.3, where $j := (n, m)$ denotes the position of the sites and σ the spin orientation. By using this parametrization, we have to perform additional simplifications, because we want to describe an interacting system with a huge extension. Consequently, the vertex functions depend on a huge set of variables. The vertex functions γ_1, γ_2 are tensors of rank two and four, where each index has $2NM$ different values. This leads to a system of differential equations of order one and dimension $\mathcal{O}(N^4M^4)$ (neglecting symmetries). To be able to solve the occurring differential equations in an acceptable time period, we need to make more approximations. Therefore, we consider only on-site contributions of the two-particle vertex function, in explicit elements with the structure $\gamma_2(j\sigma, j\bar{\sigma}; j\sigma, j\bar{\sigma})$, and set all other parts to zero. The structure of the spin indices are just reflecting the spin conservation of the interacting electrons and the Pauli-principle. This can also be derived by the general symmetry relation of the two-particle vertex function, compare section 2.3.2, which is in general very useful for setting up the fRG flow equations. From this relation it also follows immediately that $\gamma_2(j \uparrow, j \downarrow; j \uparrow, j \downarrow) = \gamma_2(j \downarrow, j \uparrow; j \downarrow, j \uparrow)$ and, hence, we are left with only NM non-zero element of the two-particle vertex function. By using (2.46), for the

one-particle vertex function we obtain the following equation

$$\frac{d}{d\Lambda}\gamma_1^\Lambda(j, \sigma; j, \sigma) = \frac{1}{2\pi} \sum_{w=\pm\Lambda} \left[\tilde{\mathcal{G}}_{j,j;\bar{\sigma}}^\Lambda(iw) \gamma_2^\Lambda(j \uparrow, j \downarrow; j \uparrow, j \downarrow) \right], \quad (3.61)$$

And using $\mathcal{G}(-iw) = [\mathcal{G}(iw)]^*$, this can be rewritten into the final form of the differential flow equation for the one-particle vertex function

$$\frac{d}{d\Lambda}\gamma_1^\Lambda(j \uparrow, j \uparrow) = \frac{1}{\pi} \operatorname{Re}\{\tilde{\mathcal{G}}_{jj;\downarrow}^\Lambda(i\Lambda)\} \gamma_2^\Lambda(j \uparrow, j \downarrow; j \uparrow, j \downarrow), \quad (3.62)$$

$$\frac{d}{d\Lambda}\gamma_1^\Lambda(j, \downarrow; j \downarrow) = \frac{1}{\pi} \operatorname{Re}\{\tilde{\mathcal{G}}_{jj;\uparrow}^\Lambda(i\Lambda)\} \gamma_2^\Lambda(j \uparrow, j \downarrow; j \uparrow, j \downarrow). \quad (3.63)$$

For the two-particle vertex function we get, after a short calculation by using (2.47), the following final form of the differential flow equation

$$\begin{aligned} \frac{d}{d\Lambda}\gamma_2^\Lambda(j \uparrow, j \downarrow; j \uparrow, j \downarrow) \\ = \frac{1}{\pi} \left[\operatorname{Re}\{\tilde{\mathcal{G}}_{jj;\downarrow}^\Lambda(i\Lambda)\tilde{\mathcal{G}}_{jj;\downarrow}^\Lambda(i\Lambda)^*\} + \operatorname{Re}\{\tilde{\mathcal{G}}_{jj;\uparrow}^\Lambda(i\Lambda)\tilde{\mathcal{G}}_{jj;\downarrow}^\Lambda(i\Lambda)\} \right] \gamma_2^\Lambda(j \uparrow, j \downarrow; j \uparrow, j \downarrow)^2. \end{aligned} \quad (3.64)$$

Using equations (3.62), (3.63) and (3.64), we reduced the system of differential equations to the dimension $3NM$. Here the index j denotes the site position (n, m) in our two-dimensional lattice, but the structure of the flow equations reveal that this approach is also applicable to a one-dimensional or three-dimensional systems ⁴.

Due to technical reasons, we don't implement these equations, but rather reformulate them, analogously to [3], by defining

$$H_{eff}^\Lambda = H_{contact}^0 - \gamma_1^\Lambda \quad (3.65)$$

and setting up the differential equations with respect to this effective Λ -dependent Hamiltonian. Consequently, the flow equation for γ_1 slightly changes to

$$\frac{d}{d\Lambda}H_{eff}^\Lambda = -\frac{d}{d\Lambda}\gamma_1(\Lambda), \quad (3.66)$$

and the initial condition, compare (2.51), becomes

$$H_{eff}^{\Lambda_{initial}} = H_{contact}^0 + \frac{1}{2} \sum_q \bar{v}_{\cdot, q; \cdot, q}. \quad (3.67)$$

After the fRG flow, we obtain

$$H_{eff}^{\Lambda_{final}} = H_{contact}^0 - \gamma_1^{\Lambda_{final}} = H_{eff}, \quad (3.68)$$

⁴These flow equations were already implemented for a one-dimensional system by Florian Bauer within the framework of his master thesis [3].

which is the desired effective non-interacting Hamiltonian of the contact region which takes the interaction into account. With this solution the corresponding Green function of the interacting region reads

$$\mathcal{G}_{eff}(iw) = \frac{1}{iw\mathbb{1} - \underbrace{H_{contact}^0 + \gamma_1^{\Lambda_{final}}}_{=-H_{eff}} - \Sigma_{leads}}, \quad (3.69)$$

which we use in section 3.4 to calculate the desired physical quantities, especially the conductance.

3.3.2 Efficient Computation of certain elements of the Green function

In the latter subsection we derived the fRG flow equations for our two-dimensional model with some far reaching approximations. Now we want to come to a special problem for solving these equations in higher dimensions, namely, the problem to compute the modified Green functions $\tilde{\mathcal{G}}^\Lambda(i\Lambda)$ in an efficient way. This is a crucial part in dealing with the system of differential equations, because we use a standard Runge-Kutta algorithm [42, chap. 17.1] to find it's solution. And this algorithm evaluates the right hand side of the differential equations and therefore the Green function for different Λ about a thousand of times to obtain a satisfying accuracy.

To bring this problem into a mathematical context, we recapitulate that calculating the modified Green function of the contact region is, in our discrete lattice space, nothing else as computing the inverse of the huge matrix

$$\left[\tilde{\mathcal{G}}^\Lambda(i\Lambda)\right]^{-1} = i\Lambda\mathbb{1} - H_{contact}^0 - \Sigma_{leads} + \gamma_1^\Lambda. \quad (3.70)$$

We visualize the structure of this matrix, which is equivalent to the structure of $H_{contact}^0 + \Sigma_{leads}$, in figure 3.7 . It is dominated by the non-interacting Hamiltonian of the contact region. The one-particle vertex function γ_1 lives only on the diagonal part, because we just take on-site contributions of the vertex functions into account. The self-energy of the leads gives a contribution to the first and last diagonal-block of the matrix and provides hopping between arbitrary sites on the surface to the leads. For a one-dimensional systems is $H_{contact}^0 + \Sigma_{leads}$ just tridiagonal and becomes block-tridiagonal for $M > 1$, where the blocks are $M \times M$ matrices.

As we already said, this matrix is huge. For example, $[\tilde{\mathcal{G}}^\Lambda]^{-1}$ is a 20000×20000 matrix with about 10^8 entries for a system with $N = 1000$ and $M = 20$. But most of the elements are zero. If we consider a typical system we are dealing with, including $M \ll N$, then the number of non-trivial entries is of order $\mathcal{O}(NM)$, in contrast to $(NM)^2$ elements of the matrix. This means for our example, only 0.02% of the elements are non-zero. Such matrices where almost all elements are zero are called *sparse matrices*. Unfortunately, the inverse of such a sparse matrix is in general a full matrix. The naive approach to compute

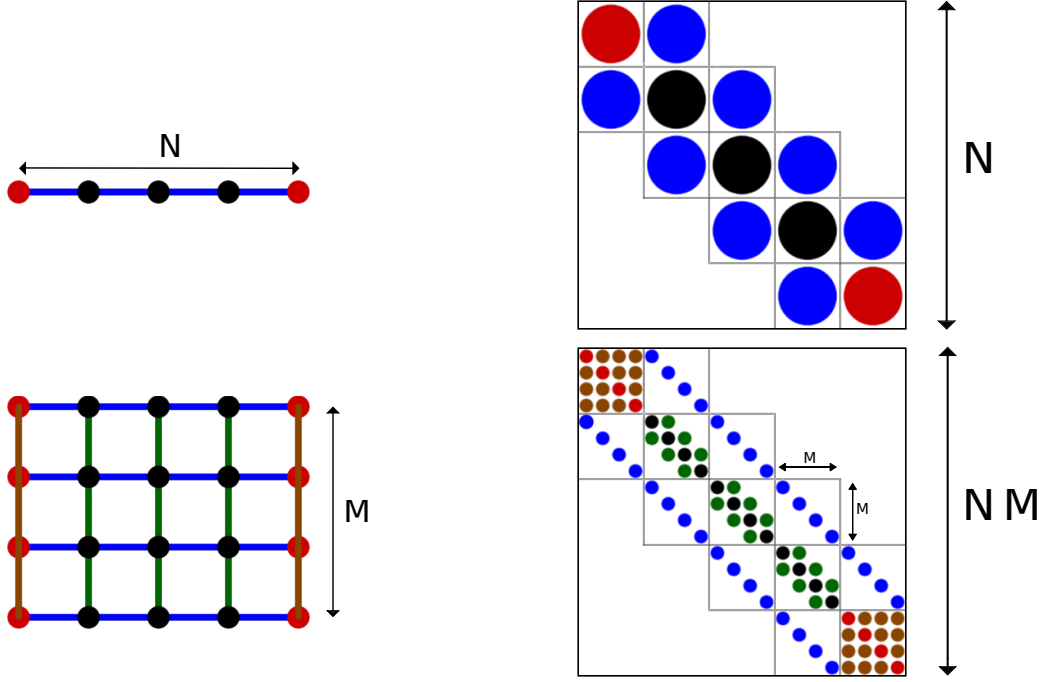


Figure 3.7: Matrix structure of $[\tilde{\mathcal{G}}^\Lambda]^{-1}$, $H_{contact}^0 + \Sigma_{leads}$, for a one- and two-dimensional system with $N = 5$, $M = 1$ (upper panels) and $N = 5$, $M = 4$ (bottom panels). The black and red dots represent the diagonal elements, where the reds are modified due to Σ_{leads} . The blue lines/dots represent the hopping elements in x-direction and the green and brown lines/dots the hopping elements in y-direction, where the browns are modified or generated due to Σ_{leads} . In the left panels we use a mesh for the graphical representation of the matrix, where the lines describe off-diagonal elements, and in the right panels a standard matrix representation.

the whole inverse using Gaussian elimination method is far to slow and requires a huge amount of memory. All this data is just unnecessary, having a look on the differential equations (3.62), (3.63) and (3.64), we can observe that we don't need the whole modified Green function. In fact, we only have to compute the diagonal elements, because we restricted ourself to an on-site effective interaction. We conclude that we need a fast algorithm to compute the diagonal elements of a sparse matrix.

In the following we want to introduce two algorithms for this purpose, the recursive Green function (RGF) algorithm, that is the state-of art method to tackle quasi one-dimensional systems, and the algorithm, called Fast Inverse using Nested Dissection (FIND), that is a new and efficient approach for 2D and 3D systems. Due to computational costs, we will restrict ourselves to systems with small widths and implement the RGF approach. At first, we give a short introduction of the RGF algorithm and state the prime results, for more details and explicit derivations we refer to appendix D. Afterwards, we also give a short introduction of FIND, to show how our approach could be extended to vast 2D problems.

Recursive Green function algorithm

The recursive Green function algorithm was developed by Klimeck and Svinzhenko et al. [47, 27]. It's an efficient method to compute certain elements of the inverse of a sparse matrix. It can be shown that this algorithm is the most efficient algorithm for quasi one-dimensional systems [27], where a quasi one-dimensional system is a system whose extension is vast in one direction and thin in the other direction. The running time of this algorithm is $\mathcal{O}(NM^3)$ and the memory cost $\mathcal{O}(NM^2)$ [28], where N and M are the grid points in the transverse and longitudinal direction. Therefore, this approach is favourable if M is very small.

To show how to compute certain elements of an inverse with this approach, we consider the following matrix

$$A = \begin{pmatrix} A_1 & B_{1,2} & & & \\ B_{2,1} & A_2 & \ddots & & \\ & \ddots & \ddots & & \\ & & & B_{N-1,N} & \\ & & & & A_N \end{pmatrix}, \quad (3.71)$$

where the diagonal and off-diagonal elements A_i , $B_{i,j}$ are complex numbers or complex quadratic matrices and the remaining elements are just zero. Then the recursive Green function method enables us to compute the diagonal elements of $D := A^{-1}$ by computing recursively two sequences. The *forward recursion* calculates the quantities $d_{i,i}^L$ with $i = 1, \dots, N$ via

$$\begin{aligned} d_{1,1}^L &= (A_1)^{-1} \\ d_{2,2}^L &= (A_2 - B_{2,1}d_{1,1}^L B_{1,2})^{-1} \\ &\vdots \\ d_{N,N}^L &= (A_N - B_{N,N-1}d_{N-1,N-1}^L B_{N-1,N})^{-1}. \end{aligned} \quad (3.72)$$

The quantities d^L are also called left connected Green functions, if the desired inverse D is a Green function. The last element/block $d_{N,N}^L$ is special, because it's the exact solution of the last diagonal element/block of the inverse

$$d_{N,N}^L \equiv D_{N,N}. \quad (3.73)$$

The second sequence, the *backward recursion* is defined in decreasing order as follows

$$\begin{aligned} D_{N,N} &= d_{N,N}^L \\ D_{N-1,N-1} &= d_{N-1,N-1}^L (1 + B_{N-1,N} D_{N,N} B_{N,N-1} d_{N-1,N-1}^L) \\ &\vdots \\ D_{1,1} &= d_{1,1}^L (1 + B_{1,2} D_{2,2} B_{2,1} d_{1,1}^L) \end{aligned} \quad (3.74)$$

and provides us with the desired diagonal elements $D_{i,i}$. To analyse this recursion relations, we consider our application, where the elements A_i and $B_{i,j}$ of the matrix A are $M \times M$

matrices. The forward recursion includes N -times the inverse of these blocks and hence, the running time scales as $\mathcal{O}(NM^3)$. This is in contrast to the backward recursion, which includes only simple block multiplications and scales as $\mathcal{O}(NM^2)$. Therefore, the forward recursion is slower by a factor of M .

Although, we need only the diagonal elements of the modified Green functions for solving the fRG flow equations, we also show how to calculate the off-diagonal element $D_{1,N}$ with the RGF approach. For our purposes this becomes important in section 3.4.1, where we will see that the conductance of our sample can be calculated via the block $[\mathcal{G}_{eff}]_{1,N}$ of the final Green function after the fRG flow. It can be shown that the following relations hold

$$D_{i,j}|_{i < j} = -d_{i,i}^L B_{i,i+1} D_{i+1,j}, \quad (3.75)$$

$$D_{i,j}|_{j < i} = -D_{j,i+1} B_{i+1,i} d_{i,i}^L. \quad (3.76)$$

Using 3.75 and the forward recursion, we can compute the $D_{1,N}$ element/block by

$$D_{1,N} = (-1)^{N+1} \left(\prod_{i=1}^{N-1} d_{i,i}^L B_{i,i+1} \right) D_{N,N}. \quad (3.77)$$

For the computation of the conductance we have to perform the forward recursion and then we are left with some simple multiplications, see (3.77). Therefore, this computation scales similar to the forward recursion. But, all together, the computational costs of the conductance is negligible, because this includes just the computation of $[\mathcal{G}_{eff}]_{1,N}$ once after solving the flow equations. In contrast to thousand of times computing $\tilde{\mathcal{G}}^\Lambda(i\Lambda)$ needed to solve the flow equations.

FIND algorithm

The Fast Inverse algorithm using Nested Dissection (FIND) was developed by Li and Klimeck et al. [27, 28]. This algorithm is much more involved compared to RGF and we will restrict ourselves to a very short description based on [27, sec. 4] and [28, chap. 2].

The FIND algorithm is based on computing certain elements of the inverse by successively performing LU factorizations⁵ and reusing them in an efficient manner. It can be used for any 2D or 3D device with arbitrary geometry and boundary condition. The only requirement is that the matrix is the result of a discretization procedure and hence the sites are only connected to neighbouring sites within a certain radius. With every single LU factorization it is possible to compute one diagonal element via $D_{NN} = 1/U_{NN}$, where U is the upper-triangular matrix. After the computation of one diagonal element of the inverse, the matrix is reordered and another LU factorization is performed to obtain another element. These factorizations can be made faster by reordering the matrix in such a way that most of the sparsity of the original matrix is preserved. To minimize unwanted

⁵For an introduction of the method of LU decomposition for computing the inverse of a matrix we refer to [42, chap. 2.3].

fill-ins, the method of nested dissection of George et al. is used. It is obvious that the computation of these factorizations significantly overlap. Therefore, partial LU factorizations are determined, which can be computed independently and are used for the factorization of several different orders of the matrix. With this approach the running time and memory costs can be reduced considerably. For an optimal implementation the running time scales as $\mathcal{O}(NM^2)$ and the memory cost $\mathcal{O}(NM \log(M))$.

Therefore, the running time and memory cost of the FIND algorithm scales a lot better as the RGF algorithm. But this scaling of the FIND algorithm only pays off for extended two-dimensional systems. For quasi-one-dimensional system the RGF algorithm is still favourable, as can be seen in figure 3.8.

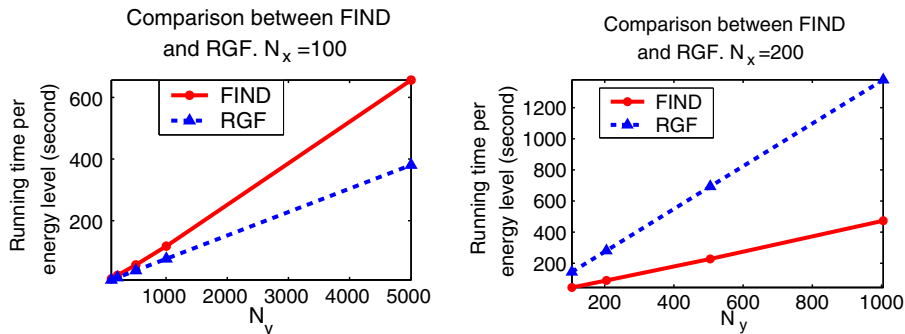


Figure 3.8: Comparison of the running time of the FIND and RGF algorithms, where the width is fixed and the length is varied, taken from [27]. In this figure the width of the system is $M = N_x$ and the length is $N = N_y$. The data come from the computation of non-equilibrium Green's functions (NEGF) for a system modelling a metal-oxide-semiconductor field-effect transistor (MOSFET).

3.4 Physical observables

In the previous section we showed how the functional Renormalization Group can be used to take a repulsive two-particle interaction in a 2D Hubbard model into account. In this section, we will discuss how the linear conductance and the spin-resolved local density of electrons can be derived in this static fRG approach. This will be based on the effective Green function G_{eff} of the non-interacting effective Hamiltonian H_{eff} , which we obtain after the fRG flow. We will show that for the conductance the vertex correction vanishes and, therefore, the conductance can be calculated by using the non-interacting Landauer formula. For the computation of the local density, we derive an modified energy integral over the Green function along the imaginary axis, which is numerically favourable.

In the following section, we will neglect the label *eff* and define the alternative notation $\mathcal{G}_{j,j}^\sigma := \mathcal{G}_{j,j,\sigma}$ to save space and improve the overview.

3.4.1 Computation of the conductance

The main goal of this thesis is to study low-temperature electron transport phenomena in interacting nanostructures. Hence, the conductance is the most important physical quantity throughout this thesis. We investigate the conductance in the limit of zero bias voltage with linear response theory. The generalization to finite bias voltages, by using Keldysh formalism, is a direction of proceeding studies. In the following section, we want to define this quantity and derive an evaluable expression for the linear response conductance in terms of our fRG approach.

The linear response conductance G of a sample is defined as the proportionality coefficient between the infinitesimal current dI when an infinitesimal voltage dV is applied to it,

$$dI = G \cdot dV. \quad (3.78)$$

Therefore, the conductance is in contrast to the conductivity, which is an intrinsic property of the material, a sample specific quantity. The conductance in a non-interacting mesoscopic system can be calculated with the Landauer-Büttiker formalism, see for example [7, chap. 7.1 & 7.2]. The main idea of this approach is to understand the conductance as a scattering process of quantum mechanical waves. This concept culminates, for $T = 0$, in the famous Landauer formula [7, equ. 7.33]

$$G = G_0 \sum_n \mathcal{T}_{nn}(\mu), \quad (3.79)$$

where $G_0 = 2e^2/h$ is the conductance quantum and $\mathcal{T}_{nn}(\mu)$ the eigenvalues of the transmission matrix at Fermi energy μ . Here, we assumed that the spin quantum number is degenerate. We want to study the linear conductance in an interacting system. Thus it's not clear, whether we can apply the Landauer-Büttiker formalism or not. But closer look shows that in our static fRG scheme the interacting system is mapped onto an effective non-interacting system we refer to section 2.4.1 and 3.3.1, where the static flow equations provide us with a frequency-independent self-energy, describing the influence of the interaction. Therefore, we should be able to compute the conductance of this effective non-interacting system with equation (3.79). For reasons of consistency, we don't just apply it, but rather compute G in linear response by using the Kubo formalism. We show that the vertex correction vanishes and the resulting conduction formula is equivalent to the Landauer formula applied to our effective non-interacting system.

This was already proven in the case of a one dimensional system in [13, chap. 4.4] and [20, chap. 3.2.2]. We follow these works, especially [20], and extend it to our two dimensional approach. But before we go into the details of this calculation, we want to recapitulate the Kubo formula for conductance based on [7, chap. 6].

Kubo formula for conductance

The fundamental concept of linear response theory is the assumption that the response of a system to a weak external perturbation is proportional to this perturbation itself.

Neglecting all higher orders of the external perturbation in the response of the system leads to the main result, the well known Kubo formula [7, equ. 6.7]

$$\langle A(t) \rangle = \langle A(t) \rangle_0 - \int_{t_0}^{\infty} dt' C_{AH'}^{ret}(t, t'), \quad (3.80)$$

which gives the linear response in terms of the retarded response function

$$C_{AH'}^{ret}(t, t') := -i\theta(t - t') \langle [A(t), H'(t')] \rangle_0, \quad (3.81)$$

where A is the operator describing the desired physical quantity, $\langle \dots \rangle_0$ the equilibrium average with respect to non-perturbed time-independent Hamiltonian H_0 and $\langle \dots \rangle$ the equilibrium average with respect to the perturbed Hamiltonian $H(t) = H_0 + \Theta(t - t_0)H'$.

This formalism applied to a system of charged particles with an electromagnetic field as perturbation leads to the retarded response function

$$\sigma_{\alpha\beta}(\mathbf{r}, \mathbf{r}', w) = \frac{ie^2}{w} C_{j_\alpha(\mathbf{r})j_\beta(\mathbf{r}')}^{ret}(w), \quad (3.82)$$

the conductivity tensor (here in frequency domain). In this equation the quantity $j_\alpha(\mathbf{r})$ is the component α of the current density operator $\mathbf{j}(\mathbf{r})$ for the perturbed system, where the contribution of the term proportional to the product $\mathbf{E}_{ext} \cdot \mathbf{A}_{ext}$ of external fields is neglected. In the latter formula (3.82) we just stated the so called paramagnetic term, because we are only interested in the dissipative effect of the electromagnetic field. The conductivity tensor describes the current response in direction \mathbf{e}_α with respect to an electric field component parallel to \mathbf{e}_β , which reads

$$j_\alpha(\mathbf{r}, w) = \int d\mathbf{r}' \sum_{\beta} \sigma_{\alpha,\beta}(\mathbf{r}, \mathbf{r}', w) E_\beta(\mathbf{r}', w). \quad (3.83)$$

The current operator J through the sample is obtained by the current density in terms of the conductivity tensor along a cross section of the sample. The precise implementation of this integration is arbitrary, due to current conservation. Although, the smartest way to perform it is to integrate along an equipotential cross section. The voltage enters by integrating orthogonal to the equipotential lines over the electrical field. It can be shown that this leads to the desired and well-known Kubo formula for the DC conductance

$$G = \frac{e^2}{\hbar} \lim_{w \rightarrow 0} \text{Re} \left\{ \frac{ie^2 C_{JJ}^{ret}(w)}{w} \right\}, \quad (3.84)$$

compare [7, equ. 6.34]. At this point we introduced the retarded current-current correlation function, which reads

$$C_{JJ}^{ret}(t - t') = -i\Theta(t - t') \langle [J(t), J(t')] \rangle. \quad (3.85)$$

in time domain. Therefore, the computation of the conductance is reduced to the calculation of the w -linear imaginary part of the current-current correlation function. We perform

this calculation in Matsubara frequency space and obtain $\Pi^{ret}(w)$ via the analytical continuation $iq_n \rightarrow w + i0^+$ to the real axis. The retarded current-current correlation function in Matsubara formalism is

$$C_{JJ}(iq_n) = - \int_0^\beta d\tau e^{iq_n\tau} \langle T_\tau J(\tau) J(0) \rangle. \quad (3.86)$$

We adopt the notation of Bruus & Flensberg [7] and denote q_n for bosonic Matsubara frequencies $w_n = 2n\pi/\beta$, and k_n for fermionic frequencies $w_n = (2n + 1)\pi/\beta$. We choose $J(\tau) = J_R(\tau)$, and $J(0) = J_L(0)$ for the evaluation of the current-current correlation function and introduce the abbreviation $\Pi := -C_{J_R, J_L}$, which simplifies the comparison to [13, 20]. Here, the current operators J_α with $\alpha = L, R$ are equivalent to the change of particle numbers $\mathcal{N}_L, \mathcal{N}_R$ in the left, right lead

$$J_L := -\dot{\mathcal{N}}_L = -i \sum_\sigma \sum_m \left[\tau_x c_{0,m,\sigma,L}^\dagger d_{N_L,m,\sigma} - \tau_x^* d_{N_L,m,\sigma}^\dagger c_{0,m,\sigma,L} \right], \quad (3.87)$$

$$J_R := \dot{\mathcal{N}}_R = i \sum_\sigma \sum_m \left[\tau_x c_{0,m,\sigma,R}^\dagger d_{N_R,m,\sigma} - \tau_x^* d_{N_R,m,\sigma}^\dagger c_{0,m,\sigma,R} \right]. \quad (3.88)$$

The operator J_L describes the current flowing from the left lead into the contact region and J_R the current flowing from the contact region into the right lead. The order of L and R is arbitrary, due to the time-reversal symmetry of H . In the following, we use that the hopping matrix elements are real, we assumed this in 3.2.2, and don't distinguish between $\tau_{x/y}$ and $\tau_{x/y}^*$ in the proceeding calculations.

The Matsubara retarded current-current correlation function can be separated into two parts [13, chap. 4.4.1]

$$\Pi(iq_n) = \Pi^{(a)}(iq_n) + \Pi^{(b)}(iq_n), \quad (3.89)$$

illustrated diagrammatically in figure 3.9. This can be seen in the following way. If we think of evaluating the thermal average $\langle \dots \rangle = \text{Tr} [\dots e^{-\beta H}] / \text{Tr} [e^{-\beta H}]$ in a perturbation series, then the first part $\Pi^{(a)}$ includes all diagrams that consist of two separated diagrams and the second part $\Pi^{(b)}$ includes all other diagrams, which form an overall connected diagram.

Calculation of $\Pi^{(a)}$

At first, we want to calculate the contribution $\Pi^{(a)}$ and show that this leads to a conductance formula which is equivalent to the Landauer formula for non-interacting systems. We have already mentioned that $\Pi^{(a)}$ includes all diagrams consisting of two unconnected subdiagrams. We can obtain all these diagrams by treating the possible pairings of creation and annihilation operators emerging in the four point function $J_R(\tau)J_L(0)$ as uncorrelated. And we perform the thermal average for each of these two possible pairings separately. We can now easily convince ourselves that this proceeding produces all diagrams consisting of two unconnected parts. And knowing, that all contractions at equal times vanish, due to

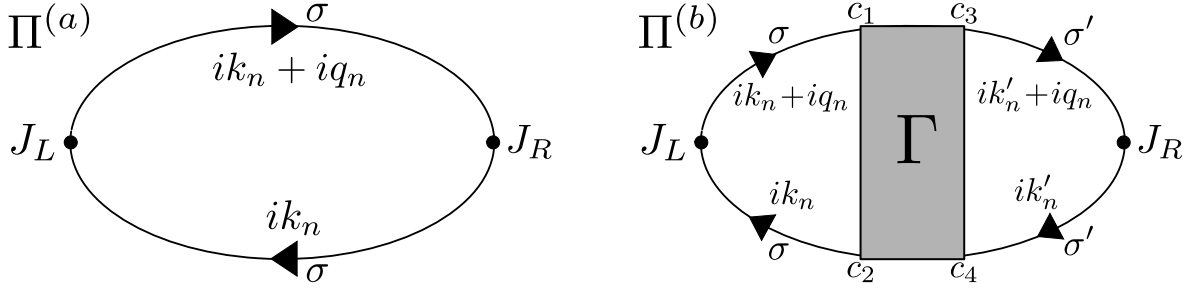


Figure 3.9: Diagrammatic representation of the two contributions $\Pi^{(a)}$ and $\Pi^{(b)}$ to the current-current correlation function $\Pi_{RL}(iq_n)$, compare [13, fig. 4.3]. In the left diagram of the vertex correction the shaded box represents the two-particle vertex function $\Gamma_{c_2, c_3; c_1, c_4}^{\sigma, \sigma'}(ik_n, ik'_n + iq_n; ik_n + iq_n, ik'_n)$.

time-translation invariance of the Hamiltonian, we obtain the following equation

$$\begin{aligned} \Pi^{(a)}(iq_n) = \sum_{\substack{m, m' \\ \sigma, \sigma'}} \int_0^\beta d\tau e^{iq_n \tau} \tau_x^2 \Big[& - \langle T_\tau d_{N_R, m', \sigma'}(\tau) c_{0, m, \sigma, L}^\dagger(0) \rangle \langle T_\tau d_{N_L, m, \sigma}(0) c_{0, m', \sigma', R}^\dagger(\tau) \rangle \\ & + \langle T_\tau c_{0, m', \sigma', R}(\tau) c_{0, m, \sigma, L}^\dagger(0) \rangle \langle T_\tau d_{N_L, m, \sigma}(0) d_{N_R, m', \sigma'}^\dagger(\tau) \rangle \\ & + \langle T_\tau d_{N_R, m', \sigma'}(\tau) d_{N_L, m, \sigma}^\dagger(0) \rangle \langle T_\tau c_{0, m, \sigma, L}(0) c_{0, m', \sigma', R}^\dagger(\tau) \rangle \\ & - \langle T_\tau c_{0, m', \sigma', R}(\tau) d_{N_L, m, \sigma}^\dagger(0) \rangle \langle T_\tau c_{0, m, \sigma, L}(0) d_{N_R, m', \sigma'}(\tau) \rangle \Big]. \end{aligned} \quad (3.90)$$

Because of the time invariance and consequential the conservation of Matsubara frequencies, switching to frequency space via the Fourier transformation

$$\mathcal{G}^\sigma(\tau, \tau') = \frac{1}{\beta} \sum_{ik_n} \mathcal{G}^\sigma(ik_n) e^{-ik_n(\tau - \tau')} \quad (3.91)$$

is favourable. In this representation one Matsubara summation becomes trivial, the same holds for one spin index, and we obtain

$$\begin{aligned} \Pi^{(a)}(iq_n) = \sum_{\sigma} \sum_{m, m'} \sum_{ik_n} \frac{1}{\beta} \tau_x^2 \Big[& - \mathcal{G}_{N_R, m; 0, m', L}^\sigma(ik_n + iq_n) \mathcal{G}_{N_L, m'; 0, m, R}^\sigma(ik_n) \\ & + \mathcal{G}_{0, m, R; 0, m', L}^\sigma(ik_n + iq_n) \mathcal{G}_{N_L, m'; N_R, m}^\sigma(ik_n) \\ & + \mathcal{G}_{N_R, m; N_L, m'}^\sigma(ik_n + iq_n) \mathcal{G}_{0, m', L; 0, m, R}^\sigma(ik_n) \\ & - \mathcal{G}_{0, m, R; N_L, m'}^\sigma(ik_n + iq_n) \mathcal{G}_{0, m', L; N_R, m}^\sigma(ik_n) \Big]. \end{aligned} \quad (3.92)$$

The projection method, especially equation (3.25) and (3.26), enables us to express the Green functions with indexes of the leads through Green functions with indexes of the

contact region

$$\mathcal{G}_{0,m,L;0,m',R}^\sigma(z) = \sum_{m'',m'''} \tau_x^2 g_{m,m''}^{\sigma,L}(z) \mathcal{G}_{N_L,m'';N_R,m'''}^\sigma(z) g_{m''',m'}^{\sigma,R}(z), \quad (3.93)$$

$$\mathcal{G}_{0,m,R;c}^\sigma(z) = - \sum_{m'} \tau_x g_{m,m'}^{\sigma,R}(z) \mathcal{G}_{N_R,m';c}^\sigma(z), \quad (3.94)$$

$$\mathcal{G}_{c;0,m,L}^\sigma(z) = - \sum_{m'} \tau_x \mathcal{G}_{c;N_L,m'}^\sigma(z) g_{m',m}^{\sigma,L}(z), \quad (3.95)$$

where c denotes an arbitrary site of the contact region. The other Green functions in (3.92) can be obtained by interchanging $L \leftrightarrow R$ in these equations. This leads to the following formula

$$\begin{aligned} \Pi^{(a)}(iq_n) = & \sum_{\sigma} \sum_{m,\dots,m'''} \sum_{ik_n} \frac{1}{\beta} \tau_x^4 \left[\right. \\ & - \mathcal{G}_{N_R,m;N_L,m'}^\sigma(ik_n+iq_n) g_{m',m''}^{\sigma,L}(ik_n+iq_n) \mathcal{G}_{N_L,m'';N_R,m'''}^\sigma(ik_n) g_{m''',m}^{\sigma,R}(ik_n) \\ & + g_{m,m'}^{\sigma,R}(ik_n+iq_n) \mathcal{G}_{N_R,m';N_L,m''}^\sigma(ik_n+iq_n) g_{m'',m'''}^{\sigma,L}(ik_n+iq_n) \mathcal{G}_{N_L,m''';N_R,m}^\sigma(ik_n) \\ & + \mathcal{G}_{N_R,m;N_L,m'}^\sigma(ik_n+iq_n) g_{m',m''}^{\sigma,L}(ik_n) \mathcal{G}_{N_L,m'';N_R,m'''}^\sigma(ik_n) g_{m''',m}^{\sigma,R}(ik_n) \\ & \left. - g_{m,m'}^{\sigma,R}(ik_n+iq_n) \mathcal{G}_{N_R,m';N_L,m''}^\sigma(ik_n+iq_n) g_{m'',m'''}^{\sigma,L}(ik_n) \mathcal{G}_{N_L,m''';N_R,m}^\sigma(ik_n) \right], \end{aligned} \quad (3.96)$$

which can be greatly simplified using the abbreviation

$$f_{m,m'}^{\sigma,s}(iw_n, iw'_n) := i\tau_x^2 (g_{m,m'}^{\sigma,s}(iw_n) - g_{m,m'}^{\sigma,s}(iw'_n)), \quad (3.97)$$

and we obtain the compact relation

$$\begin{aligned} \Pi^{(a)}(iq_n) = & - \sum_{\sigma} \sum_{m,\dots,m'''} \sum_{ik_n} \frac{1}{\beta} \left[\right. \\ & \left. \mathcal{G}_{N_R,m;N_L,m'}^\sigma(ik_n+iq_n) f_{m',m''}^{\sigma,L}(ik_n, ik_n+iq_n) \mathcal{G}_{N_L,m'';N_R,m'''}^\sigma(ik_n) f_{m''',m}^{\sigma,R}(ik_n, ik_n+iq_n) \right]. \end{aligned} \quad (3.98)$$

The summation over the Matsubara frequencies are preformed by using contour integration and the residue theorem, explained in [7, chap. 11.4]. This procedure can be summarized by the replacement

$$\frac{1}{\beta} \sum_{ik_n} F(ik_n) \rightarrow -\frac{1}{2\pi i} \int_{\mathcal{C}} dz F(z) n_F(z), \quad (3.99)$$

where the function $F(z)$ should have a number of simple poles ⁶ and vanishes for $|z| \rightarrow \infty$. Here $n_F(z) = 1/(e^{\beta z} + 1)$ is the Fermi function, which has simple poles at the fermionic Matsubara frequencies and residues $\text{Res}[n_F(z)]_{z=ik_n} = -1/\beta$.

⁶Therefore, the function $F(z)$ is analytical elsewhere in the complex plain \mathbb{C} .

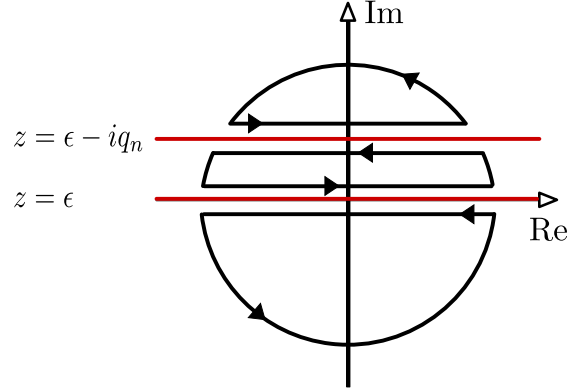


Figure 3.10: Parted contour used for the Matsubara frequency summation in equation (3.98), compare [7, fig. 16.1]. The red lines denote the branch cuts at $z = \epsilon$ and $z = \epsilon - iq_n$ of the integrand.

In our case, the two Green functions, which are evaluated at different frequencies, lead to two branch cuts of the integrand. One branch cut goes along the horizontal line $z = \epsilon$ and the other along $z = \epsilon - iq_n$ with $\epsilon \in \mathbb{R}$. Therefore, we have to separate the contour into three parts, illustrated in figure 3.10. Because the Fermi function goes to zero exponentially for $\text{Re}\{z\} \rightarrow \infty$ and to 1 for $\text{Re}\{z\} \rightarrow -\infty$ and the Green function decays $\mathcal{G}(z) \rightarrow 1/z$ for $|z| \rightarrow \infty$, the circular parts of the contour \mathcal{C} doesn't contribute, and we are left with the integration parallel to the branch cuts and obtain a summation over the following four terms

$$\begin{aligned} \Pi^{(a)}(iq_n) = & \sum_{\sigma} \sum_{m, \dots, m'''} \int_{-\infty}^{\infty} d\epsilon \frac{n_F(\epsilon)}{2\pi i} \left[\right. \\ & + \mathcal{G}_{N_R, m; N_L, m'}^{\sigma}(\epsilon + iq_n) f_{m', m''}^{\sigma, L}(\epsilon + i0^+, \epsilon + iq_n) \mathcal{G}_{N_L, m''; N_R, m'''}^{\sigma}(\epsilon + i0^+) f_{m''', m}^{\sigma, R}(\epsilon + i0^+, \epsilon + iq_n) \\ & - \mathcal{G}_{N_R, m; N_L, m'}^{\sigma}(\epsilon + iq_n) f_{m', m''}^{\sigma, L}(\epsilon - i0^+, \epsilon + iq_n) \mathcal{G}_{N_L, m''; N_R, m'''}^{\sigma}(\epsilon - i0^+) f_{m''', m}^{\sigma, R}(\epsilon - i0^+, \epsilon + iq_n) \\ & + \mathcal{G}_{N_R, m; N_L, m'}^{\sigma}(\epsilon + i0^+) f_{m', m''}^{\sigma, L}(\epsilon - iq_n, \epsilon + i0^+) \mathcal{G}_{N_L, m''; N_R, m'''}^{\sigma}(\epsilon - iq_n) f_{m''', m}^{\sigma, R}(\epsilon - iq_n, \epsilon + i0^+) \\ & \left. - \mathcal{G}_{N_R, m; N_L, m'}^{\sigma}(\epsilon - i0^+) f_{m', m''}^{\sigma, L}(\epsilon - iq_n, \epsilon - i0^+) \mathcal{G}_{N_L, m''; N_R, m'''}^{\sigma}(\epsilon - iq_n) f_{m''', m}^{\sigma, R}(\epsilon - iq_n, \epsilon - i0^+) \right]. \end{aligned} \quad (3.100)$$

We have already stated, that only the imaginary w -linear part of Π contributes to the conductance. Following the argument of [20, p. 38 ff.], we can show that the terms containing the functions $f^{R/L}$ evaluated at frequencies on the same side of a brunch cut are of order $\mathcal{O}(w^2)$ and, hence, don't contribute to G . This can be seen by having a closer look on the surface Green function for an one-dimensional semi-infinite lead $\tilde{g}(z)$. We can show that for an infinitesimal number $\delta \in \mathbb{R}$ the equality

$$\tilde{g}(\epsilon \pm i\delta) = \tilde{g}(\epsilon \pm i0^+) + \mathcal{O}(\delta) \quad (3.101)$$

holds. Because the corresponding Green function for a semi-infinite lead $g^{\sigma, s}$ with finite

width is just a superposition of \tilde{g} , see equation (3.45), it immediately follows that

$$g^{\sigma,s}(\epsilon \pm i\delta) = g^{\sigma,s}(\epsilon \pm i0^+) + \mathcal{O}(\delta). \quad (3.102)$$

To determine the w -linear contribution, we perform the limit $\delta \rightarrow 0$, that provides

$$f^{\sigma,s}(\epsilon \pm i\delta, \epsilon \pm i0^+) = \mathcal{O}(\delta), \quad (3.103)$$

and

$$f^{\sigma,s}(\epsilon - i0^+, \epsilon + i\delta) = f^{\sigma,s}(\epsilon \pm i0^+, \epsilon \mp i0^+) + \mathcal{O}(\delta). \quad (3.104)$$

We can conclude, the first and fourth term of integral (3.100) are of order $\mathcal{O}(w^2)$, hence they don't contribute to the conductance and we neglect them in the proceeding calculations. Now, we perform the analytical continuation $iq_n \rightarrow w + i0^+$ and, after shifting the integration variable $\epsilon \rightarrow \epsilon + w$ of one of the terms, we obtain

$$\begin{aligned} \Pi^{(a)}(w) &= \sum_{\sigma} \sum_{m,\dots,m'''} \int_{-\infty}^{\infty} d\epsilon \frac{1}{2\pi i} (n_F(\epsilon+w) - n_F(\epsilon)) \left[\mathcal{G}_{N_R,m;N_L,m'}^{\sigma}(\epsilon+w+i0^+) \right. \\ &\quad \times \left. f_{m',m''}^{\sigma,L}(\epsilon-i0^+, \epsilon+w+i0^+) \mathcal{G}_{N_L,m'';N_R,m'''}^{\sigma}(\epsilon-i0^+) f_{m''',m}^{\sigma,R}(\epsilon-i0^+, \epsilon+w+i0^+) \right]. \end{aligned} \quad (3.105)$$

Thus the conductance $G^{(a)}$, which arises from the first part of the retarded current-current correlation function, yields

$$\begin{aligned} G^{(a)}(\mu) &:= \frac{e^2}{\hbar} \lim_{w \rightarrow 0} \text{Im} \left\{ \frac{\Pi^{(a)}(w)}{w} \right\} = -\frac{e^2}{\hbar} \sum_{\sigma} \sum_{m,\dots,m'''} \int_{-\infty}^{\infty} d\epsilon n'_F(\epsilon) \left[\right. \\ &\quad \left. \mathcal{G}_{N_R,m;N_L,m'}^{\sigma}(\epsilon+i0^+) f_{m',m''}^{\sigma,L}(\epsilon-i0^+, \epsilon+i0^+) \mathcal{G}_{N_L,m'';N_R,m'''}^{\sigma}(\epsilon-i0^+) f_{m''',m}^{\sigma,R}(\epsilon-i0^+, \epsilon+i0^+) \right]. \end{aligned} \quad (3.106)$$

In the limit of vanishing temperature, the Fermi function is equivalent to the delta function with opposite sign, $n'_F(\epsilon) = -\delta(\mu)$, and the energy integral becomes trivial. In this case, we can rewrite the conductance into the following form

$$G^{(a)}(\mu) = \frac{e^2}{\hbar} \sum_{\sigma} \text{Tr} \left\{ \mathcal{G}^{\sigma,ret}(\mu) \Gamma_{lead}^{\sigma,R}(\mu) \mathcal{G}^{\sigma,adv}(\mu) \Gamma_{lead}^{\sigma,L}(\mu) \right\}, \quad (3.107)$$

where we defined

$$[\Gamma_{lead}^{\sigma,s}]_{n,m;n',m'}(z) := [\Gamma_{lead}]_{n,m;n',m'}^{\sigma,s}(z), \quad (3.108)$$

compare equation (3.50), and used the relation

$$[\Gamma_{lead}]_{n,m;n',m'}^{\sigma,s}(\epsilon) = \delta_{n,N_s} \delta_{n',N_s} \underbrace{i\tau_x^2 \left([g^{ret}]_{m,m'}^{\sigma,s}(\epsilon) - [g^{adv}]_{m,m'}^{\sigma,s}(\epsilon) \right)}_{=f_{m,m'}^{\sigma,s}(\epsilon+i0^+, \epsilon-i0^+)}. \quad (3.109)$$

The formula (3.107) for the conductance is an alternative representation of the Landauer formula for $T = 0$ and is more convenient for numerical calculations. For an alternative derivation of equation (3.107) we refer to [11, chap. 3.5].

Vertex Correction

In the following subsection, we want to calculate the contribution of the second part $\Pi^{(b)}$ of the current-current correlation function. This can be done by performing the same steps as we did for the calculation of $\Pi^{(a)}$. First of all, we can convince ourselves, for example by expanding (3.86) in a perturbation series, that the line-crossing diagrams are given by the formula

$$\begin{aligned} \Pi^{(b)}(iq_n) = & \frac{1}{\beta^2} \sum_{\sigma, \sigma'} \sum_{m, m'} \sum_{c_1, \dots, c_4} \sum_{ik_n, ik'_n} \left[\right. \\ & \left(\mathcal{G}_{c_1; N_L, m}^{\sigma'}(ik_n + iq_n) \mathcal{G}_{0, m, L; c_2}^{\sigma'}(ik_n) - \mathcal{G}_{c_1; 0, m, L}^{\sigma'}(ik_n + iq_n) \mathcal{G}_{N_L, m; c_2}^{\sigma'}(ik_n) \right) \\ & \times \Gamma_{c_2, c_3; c_1, c_4}^{\sigma, \sigma'}(ik_n, ik'_n + iq_n; ik_n + iq_n, ik'_n) \\ & \left. \times \left(\mathcal{G}_{N_R, m'; c_3}^{\sigma}(ik'_n + iq_n) \mathcal{G}_{c_4; 0, m', R}^{\sigma}(ik'_n) - \mathcal{G}_{0, m', R; c_3}^{\sigma}(ik'_n + iq_n) \mathcal{G}_{c_4; N_R, m'}^{\sigma}(ik'_n) \right) \right], \end{aligned} \quad (3.110)$$

where the indices c_1, \dots, c_4 denote sites of the contact region. For this derivation we used that Γ conserves Matsubara frequencies. This truncated line-crossing diagram Γ is obviously equivalent to the two-particle vertex function γ_2 , defined in equation (2.11), where the correspondence

$$\Gamma_{c_1, c_2; c_3, c_4}^{\sigma, \sigma'}(iw_1, iw_2; iw_3, iw_4) = \gamma_2(\{k_1, \sigma\}, \{k_2, \sigma'\}; \{k_3, \sigma'\}, \{k_4, \sigma\}) \quad (3.111)$$

with $k_l = \{c_l, iw_l\}$ holds. We choose this modified notation for the vertex corrections of G , because it is much more commonly used throughout the literature, see for example [13, chap. 4.4] or [7, chap. 16]. Once again, we apply the projection method, especially equations (3.25) and (3.26), to rewrite the Green functions with indices on the leads in the latter equation and obtain

$$\begin{aligned} \Pi^{(b)}(iq_n) = & \frac{1}{\beta^2} \sum_{\sigma, \sigma'} \sum_{ik_n, ik'_n} \sum_{m, \dots, m'''} \sum_{c_1, \dots, c_4} \tau_x^4 \left[\right. \\ & \left(- \mathcal{G}_{c_1; N_L, m}^{\sigma'}(ik_n + iq_n) g_{m, m''}^{\sigma, L}(ik_n) \mathcal{G}_{N_L, m''; c_2}^{\sigma'}(ik_n) \right. \\ & \quad \left. + \mathcal{G}_{c_1; N_L, m''}^{\sigma'}(ik_n + iq_n) g_{m'', m}^{\sigma, L}(ik_n + iq_n) \mathcal{G}_{N_L, m; c_2}^{\sigma'}(ik_n) \right) \\ & \times \Gamma_{c_2, c_3; c_1, c_4}^{\sigma, \sigma'}(ik_n, ik'_n + iq_n; ik_n + iq_n, ik'_n) \\ & \left. \times \left(- \mathcal{G}_{N_R, m'; c_3}^{\sigma}(ik'_n + iq_n) \mathcal{G}_{c_4; N_R, m'''}^{\sigma}(ik'_n) g_{m''', m'}^{\sigma, R}(ik'_n) \right. \right. \\ & \quad \left. \left. + g_{m', m'''}^{\sigma, R}(ik'_n + iq_n) \mathcal{G}_{N_R, m'''; c_3}^{\sigma}(ik'_n + iq_n) \mathcal{G}_{c_4; N_R, m'}^{\sigma}(ik'_n) \right) \right]. \end{aligned} \quad (3.112)$$

Using the definition of $f^{\sigma,s}$, see equation (3.97), we can rewrite this equation in a more compact way

$$\begin{aligned} \Pi^{(b)}(iq_n) = \frac{1}{\beta^2} \sum_{\sigma,\sigma'} \sum_{ik_n, ik'_n} \sum_{m, \dots, m'''} \left[\right. & \mathcal{G}_{c_1; N_L, m}^{\sigma'}(ik_n + iq_n) f_{m, m''}^{\sigma', R}(ik_n + iq_n, ik_n) \mathcal{G}_{N_L, m''; c_2}^{\sigma'}(ik_n) \\ & \times \Gamma_{c_2, c_3; c_1, c_4}^{\sigma, \sigma'}(ik_n, ik'_n + iq_n; ik_n + iq_n, ik'_n) \\ & \left. \times \mathcal{G}_{c_4; N_R, m'}^{\sigma}(ik'_n) f_{m', m'''}^{\sigma', L}(ik'_n + iq_n, ik'_n) \mathcal{G}_{N_R, m'''; c_3}^{\sigma}(ik_n + iq_n) \right]. \end{aligned} \quad (3.113)$$

Now we define the quantity

$$\begin{aligned} \Lambda_{c_1, c_2}^{\sigma}(ik_n, iq_n) := \sum_{\sigma'} \sum_{ik'_n} \sum_{m', m'''} \sum_{c_3, c_4} \Gamma_{c_2, c_3; c_1, c_4}^{\sigma, \sigma'}(ik_n, ik'_n + iq_n; ik_n + iq_n, ik'_n) & (3.114) \\ \times \mathcal{G}_{c_4; N_R, m'}^{\sigma}(ik'_n) f_{m', m'''}^{\sigma', L}(ik'_n + iq_n, ik'_n) \mathcal{G}_{N_R, m'''; c_3}^{\sigma}(ik'_n + iq_n), & \end{aligned}$$

where $\Pi^{(b)}$ becomes

$$\begin{aligned} \Pi^{(b)}(iq_n) = \frac{1}{\beta^2} \sum_{\sigma} \sum_{ik_n} \sum_{m, m''} \sum_{c_1, c_2} & (3.115) \\ \mathcal{G}_{c_1; N_L, m}^{\sigma'}(ik_n + iq_n) f_{m, m''}^{\sigma, R}(ik_n + iq_n, ik_n) \mathcal{G}_{N_L, m''; c_2}^{\sigma}(ik_n) \Lambda_{c_1, c_2}^{\sigma'}(ik_n, iq_n). & \end{aligned}$$

This equation for the vertex correction to the linear conductance is generally valid, but unfortunately its evaluation is very complicated for interacting systems. At this point, the properties of our static fRG approach come into play. The solution of the flow equations provides us with a frequency-independent two-particle vertex Γ and, hence, the Matsubara summations can be evaluated similar to $\Pi^{(a)}$, compare [13, 20].

In the following we focus on $\Lambda_{c_1, c_2}^{\sigma}$ and replace its Matsubara summation by a contour integral analogue to equation (3.100), we obtain

$$\begin{aligned} \Lambda_{c_1, c_2}^{\sigma}(ik_n, iq_n) = - \sum_{\sigma'} \sum_{m, m''} \sum_{c_3, c_4} \Gamma_{c_2, c_3; c_1, c_4}^{\sigma, \sigma'} T_x^2 \int_{-\infty}^{\infty} d\epsilon \frac{n_F(\epsilon)}{2\pi i} \left[\right. & \\ + \mathcal{G}_{c_4; N_R, m}^{\sigma}(\epsilon + i0^+) f_{m, m''}^{\sigma, R}(\epsilon + iq_n, \epsilon + i0^+) \mathcal{G}_{N_R, m''; c_3}^{\sigma}(\epsilon + iq_n) & \\ - \mathcal{G}_{c_4; N_R, m}^{\sigma}(\epsilon - i0^+) f_{m, m''}^{\sigma, R}(\epsilon + iq_n, \epsilon - i0^+) \mathcal{G}_{N_R, m''; c_3}^{\sigma}(\epsilon + iq_n) & (3.116) \\ + \mathcal{G}_{c_4; N_R, m}^{\sigma}(\epsilon - iq_n) f_{m, m''}^{\sigma, R}(\epsilon + i0^+, \epsilon - iq_n) \mathcal{G}_{N_R, m''; c_3}^{\sigma}(\epsilon + i0^+) & \\ - \mathcal{G}_{c_4; N_R, m}^{\sigma}(\epsilon - iq_n) f_{m, m''}^{\sigma, R}(\epsilon - i0^+, \epsilon - iq_n) \mathcal{G}_{N_R, m''; c_3}^{\sigma}(\epsilon - i0^+) & \left. \right]. \end{aligned}$$

Again we can use that $f^{\sigma,s}$ evaluated at the same side of a branch cut is of order $\mathcal{O}(w)$ and evaluated at different sides of order $\mathcal{O}(1)$. Therefore, it is sufficient to show that $\Pi^{(b)}$ vanishes for the second and third term of (3.116), and we can neglect the other terms in the following. After performing the analytical continuation $iq_n \rightarrow w + i0^+$ and shifting the

integration variable of one term, we obtain the formula

$$\begin{aligned} \Lambda_{c_1, c_2}^\sigma(ik_n, w+i0^+) &= - \sum_{\sigma'} \sum_{m, m''} \sum_{c_3, c_4} \Gamma_{c_2, c_3; c_1, c_4}^{\sigma, \sigma'} \tau_x^2 \int_{-\infty}^{\infty} d\epsilon \frac{1}{2\pi i} [n_F(\epsilon+w) - n_F(\epsilon)] \\ &\times \mathcal{G}_{c_4; N_R, m}^\sigma(\epsilon-i0^+) f_{m''', m'}^{\sigma, R}(\epsilon+w+i0^+, \epsilon-i0^+) \mathcal{G}_{N_R, m'''; c_3}^\sigma(\epsilon+w+i0^+). \end{aligned} \quad (3.117)$$

Using $n_F(\epsilon + \delta) - n_F(\epsilon) = \mathcal{O}(\delta)$, we conclude that (3.117) is of order $\mathcal{O}(w)$. It is also independent of the Matsubara frequency k_n and we can exclude this factor in the frequency summation of (3.115). In the addend (3.115), $f^{\sigma, s}$ occurs with arguments on the same side of a branch cut and, hence, provides an additional order of w . Therefore, $\Pi^{(b)}(w)$ is of order $\mathcal{O}(w^2)$, if w tends to zero, and we finally obtain

$$G^{(b)} = \frac{e^2}{h} \lim_{w \rightarrow 0} \frac{\mathcal{O}(w^2)}{w} = 0. \quad (3.118)$$

We conclude, the vertex correction of the linear conductance vanishes in the fRG approach of frequency-independent vertex functions, and we can apply the conductance formula (3.107) for zero temperatures.

3.4.2 Spin-resolved local density

Another interesting quantity in our system is the spin-resolved local density within the contact region. It is defined as the average of the occupation number operator

$$\bar{n}_{j, \sigma} := \langle n_{j, \sigma} \rangle = \langle c_{j, \sigma}^\dagger c_{j, \sigma} \rangle, \quad (3.119)$$

where $j = (n, m)$ collects the site indexes. At first, we want to express the local density in the standard form as an energy integral of the spectral function, where we follow [7, chap. 11.4.2]. For the derivation we use the Matsubara formalism. In this approach the average of the number operator over the grand canonical ensembles can be calculated as follows

$$\bar{n}_{j, \sigma} = \langle c_{j, \sigma} c_{j, \sigma}^\dagger \rangle = - \langle T_\tau c_{j, \sigma}^\dagger(0) c_{j, \sigma}(0^-) \rangle = \mathcal{G}_{j; j}^\sigma(0^-), \quad (3.120)$$

where we inserted the convergence factor 0^- , which enables us to insert the complex time ordering operator T_τ and express $\bar{n}_{j, \sigma}$ via the complex Green function \mathcal{G} . The corresponding Fourier transformation reads

$$\bar{n}_{j, \sigma} = \mathcal{G}_{j; j}^\sigma(0^-) = \frac{1}{\beta} \sum_{ik_n} \mathcal{G}_{j; j}^\sigma(ik_n) e^{-ik_n 0^-}, \quad (3.121)$$

where k_n are the fermionic Matsubara frequencies. The evaluation of the Matsubara summation is performed by using a contour integral and the residue theorem. The standard

contour with a closed half-circle in the upper half-plane and bottom half-plane, see [7, fig. 11.3], provides

$$\begin{aligned}
\bar{n}_{j,\sigma} &= -\frac{1}{2\pi i} \int_{\mathcal{C}_1+\mathcal{C}_2} dz n_F(z) \mathcal{G}_{j;j}^\sigma(z) e^{z0^+} \\
&= -\frac{1}{2\pi i} \int_{-\infty}^{\infty} dw n_F(w) [\mathcal{G}_{j;j}^\sigma(w+i0^+) - \mathcal{G}_{j;j}^\sigma(w+i0^-)] e^{w0^+} \\
&= -\frac{1}{2\pi} \int_{-\infty}^{\infty} dw n_F(w) 2 \operatorname{Im}\{\mathcal{G}_{j;j}^{\sigma,ret}(w)\},
\end{aligned} \tag{3.122}$$

where we used that the contribution of the circular parts goes to zero as $|z| \rightarrow 0$, which can be seen by

$$e^{z0^+} n_F(z) = \frac{e^{z0^+}}{1+e^{\beta z}} \propto \begin{cases} e^{(0^+-\beta)\operatorname{Re}\{z\}} \xrightarrow{|z|\rightarrow\infty} 0 & \text{if } \operatorname{Re}\{z\} > 0 \\ e^{0^+\operatorname{Re}\{z\}} \xrightarrow{|z|\rightarrow\infty} 0 & \text{if } \operatorname{Re}\{z\} < 0 \end{cases}, \tag{3.123}$$

and only the parts parallel to the real axis contribute. Furthermore, we used $G^{ret}(w) = [G^{adv}(w)]^*$. Using the relation between the Green function and the spectral function

$$\mathcal{A}_{j;j}^\sigma(w) = -2\operatorname{Im}\{\mathcal{G}_{j;j}^{\sigma,ret}(w)\}, \tag{3.124}$$

we finally obtain the well-known equation

$$\begin{aligned}
\bar{n}_{j,\sigma} &= \frac{1}{2\pi} \int_{-\infty}^{\infty} dw n_F(w) \mathcal{A}_{j;j}^\sigma(w) \\
&\stackrel{T=0}{=} \frac{1}{2\pi} \int_{-\infty}^{\mu} dw \mathcal{A}_{j;j}^\sigma(w).
\end{aligned} \tag{3.125}$$

In this formula, the spin-resolved local density, which is equivalent to the occupation of the single-particle quantum state $|j; \sigma\rangle$, is the energy integral over the spectral density for this state weighted by the Fermi function.

The functional Renormalization group provides us with the Green function \mathcal{G}_{eff} of the effective system, which hopefully describes the interacting system well, and we could use equation (3.125) and (3.124) for the numerical calculation of the local density. But this proceeding has the disadvantage that we would have to integrate along the real axis over a function which has many poles near the real axis. These poles are especially close, if excitations with long lifetimes exist. Hence, we can expect that the Green function has a restless analytical structure for real values and, therefore, the numerical calculation along the imaginary axis in the sense of (3.121) is favourable. So let's go back to this equation. In the limit $T = 0$ the Matsubara summation $1/\beta \sum_{k_n}$ becomes the integral $1/2\pi \int dw$ over all real frequencies, and we are left with an integral along the imaginary axis. We want to evaluate this equation numerically and, therefore, we have to deal with the convergence factor e^{-w0^-} similar to section 2.4.4. But, neglecting the convergence

factor of the right hand side of equation (3.121) modifies the equation only slightly, as we will see in the following. We can calculate the occurring summation analogously to (3.122), but we see from (3.123) that by setting $e^{ik_n 0^-}$ to zero the circular part with $\text{Re}\{w\} < 0$ now contributes, and we obtain

$$\begin{aligned} \frac{1}{\beta} \sum_{ik_n} \mathcal{G}_{j;j}^\sigma(ik_n) &= -\frac{1}{2\pi i} \int_{\mathcal{C}_1 + \mathcal{C}_2} dz n_F(z) \mathcal{G}_{j;j}^\sigma(z) \\ &= \underbrace{-\frac{1}{2\pi i} \int_{\mathcal{C}_1 + \mathcal{C}_2} dz n_F(z) \mathcal{G}_{j;j}^\sigma(z) e^{z0^+}}_{\bar{n}_{j;\sigma}} - \frac{1}{2\pi i} \int_{\mathcal{C}_1^\circ + \mathcal{C}_2^\circ} dz n_F(z) \mathcal{G}_{j;j}^\sigma(z), \end{aligned} \quad (3.126)$$

where \mathcal{C}_1° and \mathcal{C}_2° denote the circular parts of \mathcal{C}_1 and \mathcal{C}_2 . The contribution of the second term can be determined easily using $n_F(z) \mathcal{G}(z) \rightarrow 1/z$ for $|z| \rightarrow \infty$ and $\text{Re}\{z\} < 0$

$$\int_{\mathcal{C}_1^\circ + \mathcal{C}_2^\circ} dz \frac{1}{z} = \left(\int_{\pi/2}^{\pi} + \int_{\pi}^{3\pi/2} \right) d\Theta e^{-i\Theta} i e^{i\Theta} = i\pi, \quad (3.127)$$

and we obtain

$$\bar{n}_{j;\sigma} = \frac{1}{\beta} \sum_{ik_n} \mathcal{G}_{j;j}^\sigma(ik_n) + \frac{1}{2} = \frac{1}{\beta} \sum_{\substack{ik_n \\ k_n > 0}} 2\text{Re}\{\mathcal{G}_{j;j}^\sigma(ik_n)\} + \frac{1}{2}, \quad (3.128)$$

where we used $\mathcal{G}(-iw_n) = \mathcal{G}(iw_n)^*$. In the limit $T = 0$ we finally get

$$\bar{n}_{j;\sigma} \stackrel{T=0}{=} \frac{1}{\pi} \int_{-\infty}^{\mu} dw \text{Re}\{\mathcal{G}_{j;j}^\sigma(w)\} + \frac{1}{2} \quad (3.129)$$

with the chemical potential μ of our system. This is the main result of this subsection and in the following, we will use this approach for calculating the spin-resolved local density.

Chapter 4

Quantum point contacts

In this chapter we want to discuss some general features of quantum point contacts and introduce a common experimental realization, the split gate geometry. This will be based on [14, chap. 5]. The most striking phenomena is the conductance quantization, that will be explained with the non-interacting adiabatic transport model. It shows a characteristic dependence on the constriction potential, we consider a saddle point potential, the magnetic field and the temperature. For interacting QPCs an abnormal and unexplained magnetic field and temperature behaviour of the conductance, including an additional step at around $0.7 \times G_0$ is observable. We introduce various experimental researches in this field, including studies of Thomas, Kirstensen, Cronenwett, Koop and Komijani et al. and discuss peculiarities of higher spin-degenerate subbands. At the end we introduce the Kondo-related model of Meir et al. and the model of Lunde et al., which is based on two-electron momentum-non-conserving scattering processes.

4.1 Introduction

One of the most striking transport phenomena in mesoscopic physics is the conductance quantization, meaning that the conductance of every perfect transmitting mode is $g_0 = e^2/h$, the spin-resolved conductance quantum. This quantization was predicted in 1957 by Landauer and his famous Landauer formalism [7, chap. 7.1 & 7.2]. The first experiments confirming the quantization were independently done by van Wees et al. [53] and Wharam et al. [54] in 1988. For their measurements, they used one of the simplest structures in nanophysics, a quantum point contact (QPC). This is a constriction between two extended electron reservoirs on the length scale of nanometers. Such a constriction can experimentally be realized by a split gate geometry, where a negative voltage is applied to two gates on top of a two-dimensional electron gas. The strong transversal confinement leads to a measurable energy splitting of the transmission modes. The lateral confinement and consequently the number of transversing electron modes can be controlled by the gate voltage. This leads to the observed staircase of conductance in units of $G_0 = 2g_0$ with respect to the gate voltage, see figure 4.2. An important requirement for this observation is that

the current flow of electrons between the reservoirs is ballistic, which demands that the extension of the constriction is smaller than the coherence length of the electrons. To fulfil this requirement for measurements in semiconductors, the temperature has to be adjusted in Kelvin regime ($T \lesssim 5K$).

Besides this fundamental phenomena of conductance quantization $G = N \times G_0$, which can be understood in a non-interacting model, additional unexplained features arise in experimental measurements. This includes an abnormal magnetic field dependence and an additional intermediate step at around $0.7 \times G_0$, which becomes stronger if the temperature increases. This shoulder like structure in the conductance trace is called *0.7 anomaly* and has already been observed in the experiments of van Wees et al. in 1988, see figure 4.2. But, they didn't comment on this feature and it took some time until the 0.7 anomaly was mentioned by Patel et al. [41] in 1991. The first detailed study was done in 1996 by Thomas et al. [49]. Many experimental measurements followed, showing that this non-integer conductance step is a generic effect. Since that time, experimental and theoretical physicists made a great effort to explain its physical origin. But, until now, there exists no microscopic model which can explain all phenomena. The difficulties to explain this anomaly is in clear contrast to its simplicity and its meaning as a key element for more involved nanostructures. Therefore it is adjusted to speak of a "Mesoscopic Mystery" [36]. At least, there is a scientific consensus that these conductance anomalies are caused by a many-body phenomena. And most of the theoretical approaches assume an enhanced role of the electron-electron interaction.

4.2 Experimental setup

One of the most common experimental manufacturing method of such quantum point contacts is the split gate technique [14]. The basis of this technique is a two dimensional electron gas (2DEG) created on the interface of two semiconductors, for example *GaAs/GaAlAs*. Such heterostructures can be fabricated with atomic precision using molecular beam epitaxy (MBE). The advantage of a 2DEG in a semiconductor is the long mean free path of the electrons ($< 10\mu m$). These are comparable to the extension of the created structures and therefore ballistic transport becomes possible. Two ohmic contacts are con-

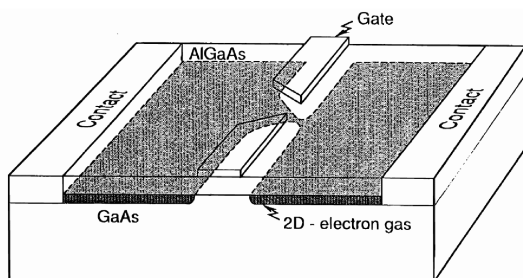


Figure 4.1: Schematic cross-section of a split gate geometry modelling a QPC, taken from [52]. Between the GaAs/AlGaAs semiconductor heterostructure a two-dimensional electron gas (2DEG) forms. By applying a negative voltage on the gates, the electrons are depleted and a quasi-one-dimensional gas forms between the gates. This is the operating point for QPC studies. Transport measurements are done by applying a bias voltage on the ohmic contacts.

nected on the left and right of the 2DEG, so that a voltage can be applied to it. To set a narrow constriction on the electron current flow, two metallic gate-electrodes are put on top. A schematic illustration of this setup can be seen in figure 4.1. By applying a negative voltage V_g to these gates, the 2DEG underneath and around the gates are depleted and a constriction potential develops. The width of this constriction can accurately be controlled via the gate voltage V_g . Also, its length is influenced by the voltage and becomes longer if V_g is more negative. For sufficient high values a quasi one-dimensional electron gas forms between the gates. Often, an additional gate, which spans over the whole 2DEG, is installed on top or back ¹. By the applied voltage on this top/back gate, the electron density of the electron gas is controlled.

4.3 Conductance quantization

In this experimental setup a staircase of the conductance in units of G_0 with respect to the applied gate voltage can be observed for sufficient low temperatures and sufficient negative gate voltages. In figure 4.2 we can see the experimental measurements of van Wees [53] revealing the staircase of G . The simplest theoretical model which inherits this phenomena is the non-interacting adiabatic transport model [7, 14, chap. 7.3.1, 5.1.1]. The general structure of the conductance steps can also be understood in this non-interacting model, under the assumption of a saddle point form of the constriction potential. And experiments with split gate geometries show good agreements for this potential form [14]. For a better understanding of the experimental observations in section 4.4, we will also discuss the magnetic field and temperature dependence in the non-interacting model.

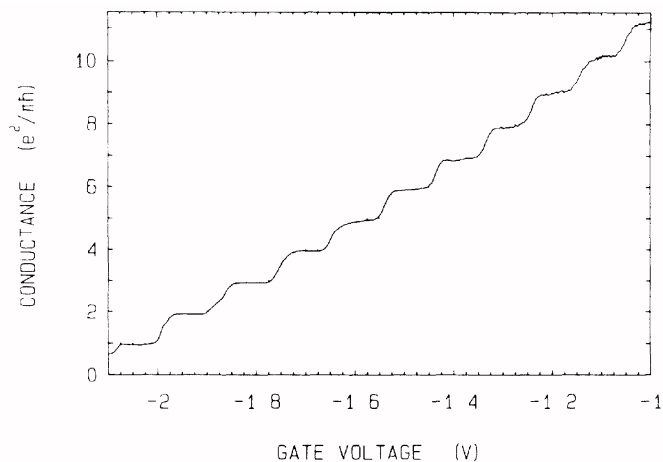


Figure 4.2: Point-contact conductance as a function of the gate voltage measured by van Wees et al. [53]. With increasing negative gate voltage and decreasing width of the constriction, the transmitting transversal eigenmodes are successively suppressed. For each suppressed transmission mode the conductance lowers by the conductance quantum G_0 .

¹The additional top/back gate isn't illustrated in figure 4.1.

4.3.1 Adiabatic transport model

We consider coherent non-interacting electrons in a two-dimensional space, propagating through a constriction described by the potential $V_{cstr}(x, y)$. The corresponding two-dimensional stationary Schrödinger equation is

$$\left[-\frac{1}{2m} (\partial_x^2 + \partial_y^2) + V_{cstr}(x, y) \right] \psi(x, y) = E \psi(x, y). \quad (4.1)$$

We assume that ψ can be expanded in longitudinal and transversal eigenfunctions, such that $\psi(x, y) = \sum_n \phi_n(x) \chi_{n,x}(y)$ holds, where the transversal eigenfunctions $\chi_{n,x}(y)$ and its eigenvalues $\epsilon_n(x)$ depend on the longitudinal position x . Inserting this expansion into the Schrödinger equation and using the completeness of $\chi_{n,x}$ provides

$$\int dy \chi_{n,x}^*(y) \left[-\frac{1}{2m} (\partial_x^2 + \partial_y^2) + V_{cstr}(x, y) \right] \sum_m \phi_m(x) \chi_{m,x}(y) = E \phi_n(x), \quad (4.2)$$

$$\iff \left[-\frac{1}{2m} \partial_x^2 + \epsilon_n(x) \right] \phi_n(x) + \sum_m B_{nm} \phi_m(x) = E \phi_n(x), \quad (4.3)$$

where the operator B_{nm} consists of two terms proportional to the first and second derivatives of $\chi_{m,x}(y)$ with respect to x . This operator induces intersubband transitions of the longitudinal modes. In this model the possible transitions are neglected and, hence, the operator is set to zero, $B_{nm} \equiv 0$, which reproduces good results if $\partial_x \chi_{m,x}(y) \approx 0$. Considering the example of a hard-wall potential in transversal direction, in explicit $V_{cstr}(x, y) = \lim_{V \rightarrow \infty} V \Theta(|y| - d(x)/2)$, the approximation is equivalent to $d'(x) \ll 1$. We conclude the underlying assumption of this approximation is an in longitudinal direction weak varying constriction potential V_{cstr} , such that the transversal eigenstates $\chi_{n,x}$ evolve smoothly into the eigenstates $\chi_{n,x'}$ without any transitions. With this, so called adiabatic approximation, we obtain an effective 1D problem of decoupled modes

$$\left[-\frac{1}{2m} \partial_x^2 + \epsilon_n(x) \right] \phi_n(x) = E \phi_n(x). \quad (4.4)$$

The influence of the transversal part of our system has been absorbed into an effective barrier $\epsilon_n(x)$. In our previous example of a hard-wall potential in transversal direction, this is [7, equ. 7.54]

$$\epsilon_n(x) = \frac{\hbar^2 \pi^2}{2m[d(x)]^2} n^2. \quad (4.5)$$

Assuming a smooth potential along the x -direction, so that a WKB-approximation for the longitudinal eigenstates of the form

$$\phi_n(x) \approx \phi_n^{WKB}(x) = \frac{1}{\sqrt{p(x)}} \exp\left(i \int_{-x}^x dx' k(x')\right) \text{ with } k(x) = \sqrt{2m(E_F - \epsilon_n(x))} \quad (4.6)$$

are possible. One can show that the transmission amplitude is one, if the Fermi energy E_F is greater than the maximal value ϵ_n^{max} of the effective potential barrier $\epsilon_n(x)$. Otherwise only tunneling processes are possible, and the transmission probability of this mode is strongly suppressed. If the energy difference is strongly negative, in explicit $E_F - \epsilon_n^{max} \ll 0$, the transmission probability of this mode is just zero and doesn't contribute any longer to the conductance. Neglecting tunneling processes, only subbands with an effective energy barrier smaller than E_F contribute with G_0 to the conductance. And we obtain the following formula

$$G = G_0 \sum_n \Theta(E_F - \epsilon_n^{max}). \quad (4.7)$$

The width of the constriction can be changed by the gate voltage V_g and, thereby, ϵ_n^{max} of every subband n . If V_g is made less negative, the width becomes larger and, hence, ϵ_n^{max} becomes smaller. At some point $\epsilon_n^{max} < E_F$ holds and this mode begins to transmit. This leads to the conductance staircase in units of G_0 with respect to the gate voltage.

The WKB-approximation breaks down when $E_F = \epsilon_n^{max}$ and a new channel opens. For higher gate voltages, tunneling through the constriction potential takes place and a smooth crossing from one conductance step to another is observed. The exact form of this transition is in contrast to the height of the step not universal and depends on the specific form of the constriction potential. In the following section, we will use a saddle point potential and discuss in which way the transition depends on the potential parameters.

4.3.2 Saddle point model of the constriction

To determine the exact potential form of the constriction V_{cstr} we would have to solve a complicated three-dimensional Poisson equation including electrostatic effects of the gates. This equation was solved, under the assumption of a dielectric material, and leads to a complicated functional dependence of V_{cstr} with respect to the width and gap of the electrodes and their vertical distance to the two dimensional electron gas. But its solution shows that for appropriate bias voltages the constriction has the form of a saddle point, compare [14, p. 251 ff.]. An alternative justification of such a model provides a Taylor expansion in the middle of the constriction. If we neglect higher orders, the expansion has a saddle-point form due to the symmetry of the QPC geometry. Therefore, we consider the constriction potential

$$V_{cstr}(x, y) = \tilde{V}_g + \frac{1}{2}mw_y^2y^2 - \frac{1}{2}mw_x^2x^2, \quad (4.8)$$

where \tilde{V}_g is the height of the potential at the center $(0, 0)$. The electrons are confined in transversal direction by a harmonic potential, and in longitudinal direction they have to pass a parabolic barrier. The potential V_{cstr} depends smoothly on \tilde{V}_g , which is related to the gate voltage via $\tilde{V}_g = -\gamma|e|V_g$, where γ is the capacitive coupling between the gates and the QPC. If we make the gate voltage more negative, the width of the constriction becomes smaller, the minimum of the saddle point potential raises and the whole constriction becomes longer. The subband energies in a non-interacting system with a saddle point

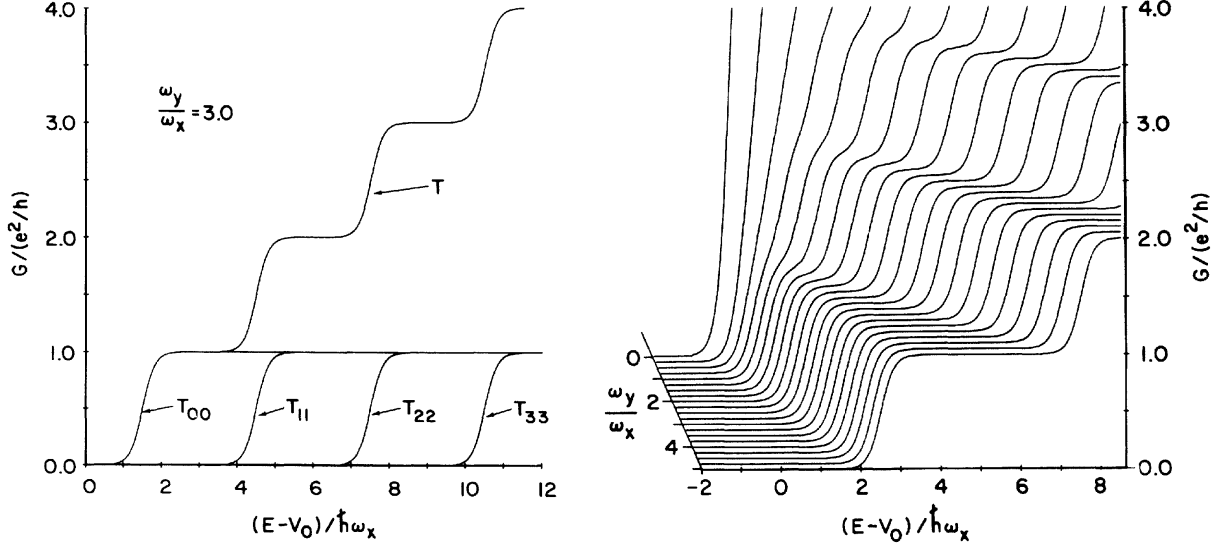


Figure 4.3: Influence of the ratio w_y/w_x on the linear conductance of a non-interacting saddle-point model, taken from [9]. In the figure is $V_0 = \tilde{V}_g$. Left panel: Single-channel transmission probabilities \mathcal{T}_{nn} and the conductance $G = \sum_n \mathcal{T}_{nn}$ as function of $(E - \tilde{V}_g)/\hbar\omega_x$ for a ratio of $w_y/w_x = 3$. Right panel: Conductance as a function of $(E - \tilde{V}_g)/\hbar\omega_x$ for different ratios w_y/w_x from 0 up to 5 in increments of 0.25.

potential are given by

$$E_n(x) = \left[n + \frac{1}{2} \right] \hbar\omega_y + \frac{\hbar^2 k(x)^2}{2m}. \quad (4.9)$$

The oscillator frequency ω_y determines the subband splitting and, hence, the averaged distance between two conductance steps, see the left panel of figure 4.10. The quantity ω_x determines the curvature of the parabolic barrier and the width for a fixed \tilde{V}_g . If ω_x is large, then the barrier is very narrow around the Fermi energy and tunneling processes have a great influence on the conductance. In this case the steps are greatly smeared out and the staircase may even become a straight line. Quantitatively, this behaviour can be seen by the calculated transmission probability of the saddle point model [9]

$$\mathcal{T}_{nn}(E) = \frac{1}{e^{-2\pi\tilde{E}_n/\hbar\omega_x} + 1} \quad \text{with} \quad \tilde{E}_n = E - \hbar\omega_y \left(n + \frac{1}{2} \right) - \tilde{V}_g, \quad (4.10)$$

which has the form of a Fermi function. The resulting conductance $G = G_0 \sum_n \mathcal{T}_{nn}$ is plotted in figure 4.10 versus $(E - \tilde{V}_g)/\hbar\omega_x$. In the right panel we can observe that the proportion between the width of a conductance plateau and the transition of the plateaus is determined by the ratio w_y/w_x . In these plots the transition width is fixed due to the energy scaling. Therefore, the basic structure of this conductance staircase is defined by this ratio.

4.3.3 Magnetic field dependence

In the following section we want to consider a magnetic field B applied in longitudinal direction, parallel to the current flow. Therefore, no orbital effects occur and the magnetic field shifts the energy of the electrons, due to Zeeman splitting. The spin-dependent Zeeman term reads

$$\Delta H = \sigma g \mu_B B / 2, \quad (4.11)$$

where $\mu_B = \hbar/2mc$ is the Bohr magneton and g the g-factor. Depending on the spin direction and the g-factor, the electron energy is either increased or lowered. For electrons in vacuum $g = 2$ holds. But the g-factor is not a universal constant, in fact, in semiconductor heterostructures, it varies widely, due to quantum mechanical addition of spin and angular momenta. The g-factor can also be negative, an example is $g = -0.44$ for bulk GaAs [14, p. 114]. In the following, we assume a negative factor. Therefore, the energy of electrons with parallel/antiparallel ($\sigma = \pm 1$) spin projection with respect to the magnetic field are shifted by $\mp |g| \mu_B B / 2$. Using the adiabatic non-interacting model, this means that the electrons in each transport channel feels a shifted effective potential, see (4.5),

$$\epsilon_{n,\sigma}(x) = \epsilon_n(x) - \sigma \frac{|g| \mu_B B}{2}. \quad (4.12)$$

Therefore, the spin-down electron of a certain transmission mode can pass the barrier before the spin-up electron. We conclude, every conductance plateau evolves into two spin-non-degenerate plateaus by applying a parallel magnetic field. Where the position of these spin-non-degenerate plateaus are symmetric around the pinch-off of the spin-degenerate plateau with an energy splitting of $\Delta V_g = \sigma |g| \mu_B B / 2$.

4.3.4 Temperature dependence

The last feature we want to discuss in the non-interacting model is the temperature dependence of the conductance quantization. The temperature behaviour can be understood by the well-known Landauer formula [11, equ. 2.5.7]

$$I = G_0 \int_{-\infty}^{\infty} dE \sum_n \mathcal{T}_{nn}(E) (f(E - \mu_1) - f(E - \mu_2)), \quad (4.13)$$

where f is the quasi-equilibrium distribution function. We assume that this function can be approximated by the Fermi function, $f \equiv n_F$. For calculating the conductance in linear response with $G = \lim_{\mu_1 \rightarrow \mu_2} I / (\mu_1 - \mu_2)$, we can use that

$$\lim_{\mu_1 \rightarrow \mu_2} \frac{n_F(E - \mu_1) - n_F(E - \mu_2)}{\mu_1 - \mu_2} = - \frac{dn_F(E)}{dE} \quad (4.14)$$

holds. And considering a transmission coefficient of the form $\mathcal{T}_{nn}(E) = \Theta(E - E_n^{min})$, where E_n^{min} is the minimum of the subband n , this provides

$$G = G_0 \sum_n \frac{1}{e^{-(E_F - E_n^{min})/k_B T} + 1} \Theta(E_F - E_n^{min}). \quad (4.15)$$

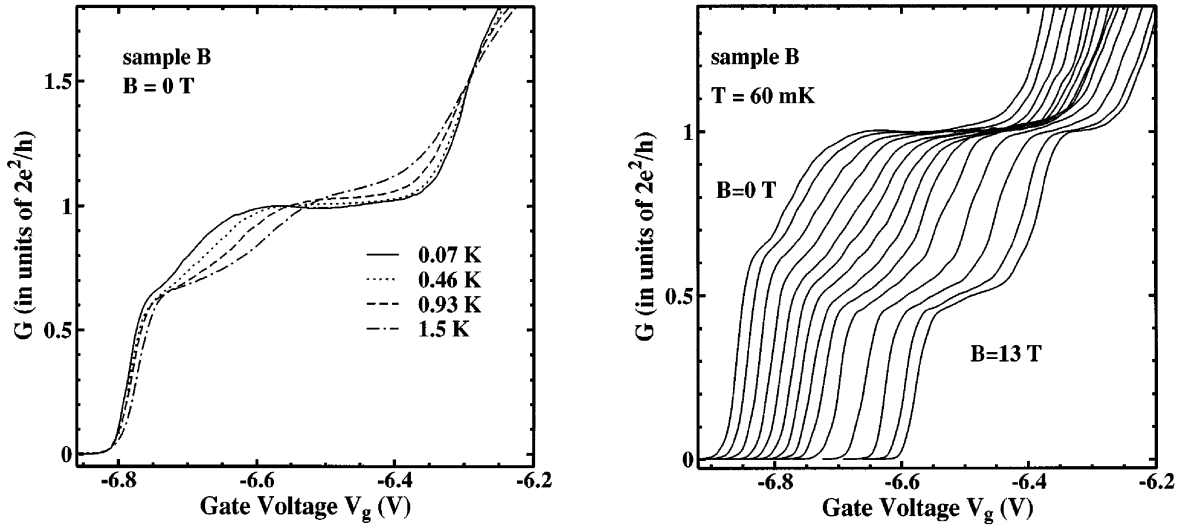


Figure 4.4: Temperature and magnetic field dependence of the 0.7 anomaly, taken from [49]. Left panel: Linear conductance as a function of the gate voltage for four temperatures in the range of $T = 0.07 - 1.5\text{K}$. Right panel: Linear conductance as a function of the gate voltage for $B = 0 - 13\text{T}$ in intermediate steps of 1T .

Therefore, the contribution of all modes to the conductance is just modified by the Fermi function $n_F(E_n^{min})$. The temperature leads to a smearing of the conductance steps and they disappear if the thermal energy $k_B T$ becomes equivalent to the subband splitting. Comparing (4.10) with (4.15) reveals the same functional structure of G , where $k_B T \hat{=} \hbar\omega_x/2\pi$ and $E_n^{min} \hat{=} \hbar\omega_y(n + 1/2) - \tilde{V}_g$. And we conclude that the effect of temperature is the same as the effect of tunneling processes through a saddle point potential.

4.4 Conductance Anomalies

Besides these fundamental non-interacting phenomena, we explained in the last section, additional unexplained features arise in experimental measurements. The most striking ones are an additional intermediate step at around $0.7 \times G_0$, which becomes more pronounced for evaluated temperatures, and an anomalous magnetic field dependence, where the spin-degenerate plateaus evolve from above into the spin-resolved plateaus for increasing magnetic fields. These experimentally observed phenomena are highly in contrast to the behaviour in a non-interacting system and, until now, they are not understood. Therefore, we call them conductance anomalies.

4.4.1 Experimental Observations

The assumption of an enhanced role of the electron-electron interaction in quantum point contact geometries is strengthened by the experiments of Thomas et al. [49, 48]. The au-

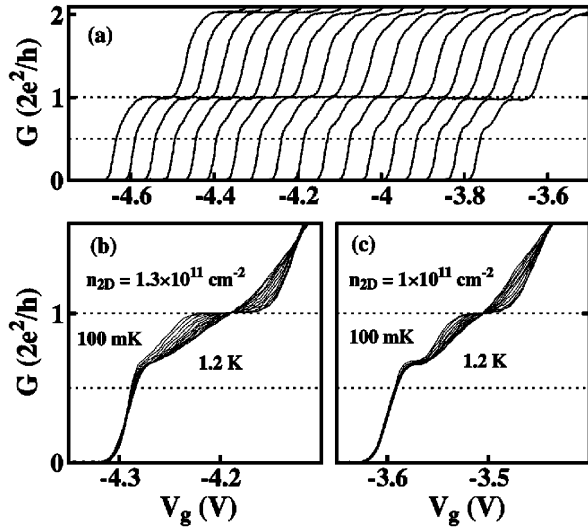


Figure 4.5: Influence of the electron density of the 2DEG on the 0.7 anomaly, taken from [48]. In the upper panel (a) the temperature is fixed $T = 60\text{mK}$ and the 2DEG density is reduced from left to right from $1.4 \times 10^{11}\text{cm}^{-2}$ to $1.1 \times 10^{11}\text{cm}^{-2}$ in steps of $1.8 \times 10^9\text{cm}^{-2}$. In the bottom panels (b) and (c) the 2DEG density is fixed and the temperature is varied from 100mK to 1.2K in steps of 0.1K .

thors showed that a decreasing electron density of the 2DEG strengthens the 0.7 anomaly, see figure 4.5. For a decreasing electron density the electron-electron interaction becomes stronger, due to a reduction of the screening. They also found that with increasing temperature the intermediate step becomes more pronounced, see left pattern of figure 4.4, which is in clear contrast to the non-interacting case and most mesoscopic phenomena, like Coulomb blockade or quantum interference [14]. They also investigated the influence of a large in-plane magnetic field. Their measurements shows that the 0.7 anomaly evolves smoothly from above into the first spin-resolved conductance plateau $0.5 \times G_0$, compare figure 4.4 right pattern. This behaviour stands highly in contrast to the non-interacting case we described in 4.3.3. Therefore, the authors suggested that the 0.7 anomaly may be induced by a symmetry breaking of spin-up and spin-down electrons persistent even for $B = 0$.

Numerous experiments on the physical origin of the conductance anomaly followed. Kirstensen et al. [21] investigated the anomalous temperature dependence in more details and obtained experimental evidence that the 0.7 anomaly is associated with an electron density-dependent energy difference between the chemical potential and an anomalous subband edge, which is of order of some Kelvin. The authors suggested that this energy gap may be the consequence of a possible breaking of spin degeneracy in the QPC. Based on this assumption, Reilly et al. introduced a phenomenological model that describes the detailed shape and position of the 0.7 anomaly by the rate at which this spin gap opens for decreasing gate voltage [44, 43]. This model is in striking agreement with the experimental dependence on temperature, magnetic field, source-drain bias and potential profile.

Graham et al. reported on experimental measurements of the QPC conductance in high in-plane magnetic fields, such that the Zeeman energy is equal to the 1D subband spacing [16]. This means the spin-split subbands of two neighbouring spin-degenerate subbands intersects, for example $1 \uparrow$ with $2 \downarrow$. In this intersection region they found a spontaneous spin splitting giving rise to an additional "0.7 anomaly"-like structure in the

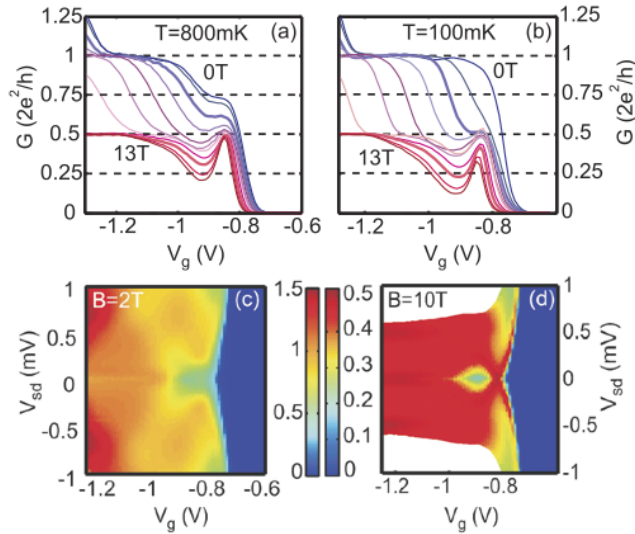


Figure 4.6: Influence of a perpendicular magnetic field on the conductance and differential conductance of a hole QPC, taken from [24]. Upper panel: Linear conductance G as a function of V_g for different perpendicular magnetic fields, from $B = 0T$ to $B = 13T$, for (a) $T = 800mK$ and (b) $T = 100mK$. Bottom panel: Differential conductance dI/dV_{sg} at $T = 100mK$ for (c) $B = 2T$ [third trace from the top of the panel (b)] and (d) $B = 10T$ [third trace from the bottom on the panel (b)]. Note the different color scales for the bottom panels.

conductance, which evolves from the $1.5G_0$ plateau. Hence, the authors suggested that such a spontaneous spin splitting occurs whenever two subbands of opposite spin cross.

The experimental work of Cronenwett et al. [10] gives a different viewpoint of the anomalous conductance behaviour. Their measurements exhibit several coinciding characteristics of the 0.7 anomaly and the Kondo effect in quantum dots. This includes a zero-bias peak in the differential conductance, which splits in an in-plane magnetic field equivalent to a Kondo system out of equilibrium [51]. The authors further demonstrated the possibility to scale the temperature dependence of the QPC to a modified Kondo form

$$G = G_0 \frac{1}{1/2 f(T/T_K) + 1/2} \quad \text{with} \quad f \sim \left[1 + (2^{1/s} - 1) (T/T_K)^2 \right]^{-0.22}, \quad (4.16)$$

by introducing an appropriate Kondo temperature T_K . This behaviour is surprising, because for Kondo-like physics one would expect some sort of localized magnetic moment in the QPC.

Recent experiments with QPCs have also been performed in two dimensional hole gases (2DHG). These p-doped systems have the advantage that the Coulomb interaction between the carriers are stronger compared to n-doped systems. The reason is the much higher effective mass of holes compared to electrons.

Komijani et al. performed experiments in such a hole QPC with a magnetic field applied *perpendicular* to the 2DHG [24]. There are only a few publications about QPC studies using a perpendicular magnetic field orientation. Besides the energy splitting of the spin subbands, the authors emphasize the effect of this field orientation by two processes. First, the orbital part of the resonant wavefunctions shrinks and, second, the amplitude of the carrier density around the bare QPC potential is largely enhanced in high fields. In their measurements, the authors found a "0.7 anomaly"-structure which evolves smoothly into a Coulomb resonance-like peak at high perpendicular magnetic fields, see figure 4.6 upper

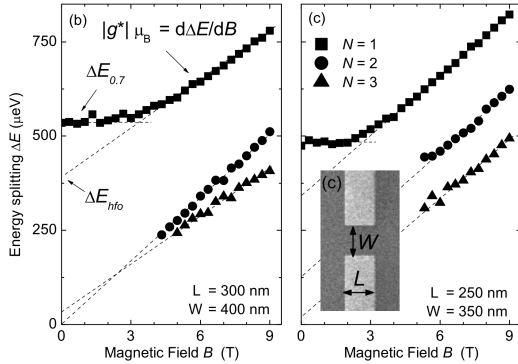


Figure 4.7: Energy splittings as a function of the magnetic field, taken from [26]. Left/right panel: Energy splittings ΔE versus magnetic field B at $T = 200 \text{ mK}$ for a QPC with length $L = 300/250 \text{ nm}$ and width $W = 400/350 \text{ nm}$ for subbands $N = 1, 2, 3$. Inset: Micrograph of one QPC out of a device containing 8. L is defined as the width of the gate electrodes and W as the space between them.

panel. This evolution is accompanied by a Coulomb blockade diamond² in the finite bias conductivity, see figure 4.6 bottom panel. These experimental observations are robust with respect to a lateral electric field and thermal cycling. Komijani et al. interpreted these results as an evidence of the importance of a quasi-localized state in the QPC and Coulomb blockade physics for the origin of the 0.7 anomaly.

4.4.2 Higher conductance plateaus

Up to now, we have concentrated on the 0.7 anomaly occurring at around $0.7 \times G_0$. In the following subsection, we want to rise our attention to higher spin-degenerate subbands $N > 1$, where N labels the subbands and starts with the lowest subband.

The presented results are based on the studies of Koop et al. [25, 26], who investigated the influence of device geometry on the many-body effects in quantum point contacts. Therefore, QPCs with different widths L and distances W of the split gates were used, see the inset of figure 4.7. Koop et al. studied among others the energy splitting ΔE between spin-up and spin-down levels, see figure 4.7, which can be determined by the gate voltage difference of the peaks in the transconductance traces dG/dV_g , where a peak indicates the onset of transport through a subband, compare figure 4.9 bottom panel. For the lowest subband $N = 1$ an energy offset $\Delta E_{0.7}$ ($\approx 0.5 \text{ meV}$) at zero-magnetic field is observable, which indicates the appearance of the 0.7 anomaly. This is in contrast to higher submodes. For $N = 2, 3$, no clear zero-field splitting occurs and only a slightly flatter conductance trace, compared to the expectations for a non-interacting model, is observable. Other researches report about an analogous *1.7 anomaly* around $1.7 \times G_0$ for certain QPCs devices [45], which are based on experimental measurements where a finite zero-field splitting was reported [48]. But also these measurements don't show a second peak in the transconductance trace of the second spin-degenerate subband for $B = 0T$, as can be seen in the right panel of figure 4.8. For the third subband $N = 3$ the zero-field splitting is strictly zero.

Another difference of the first and higher conductance plateaus is the temperature dependence. In figure 4.9, the linear conductance G and transconductance dG/dV_g versus V_g

²An introduction of Coulomb diamonds in a single-electron transistor can be found in [38] chapter 3.2.2.

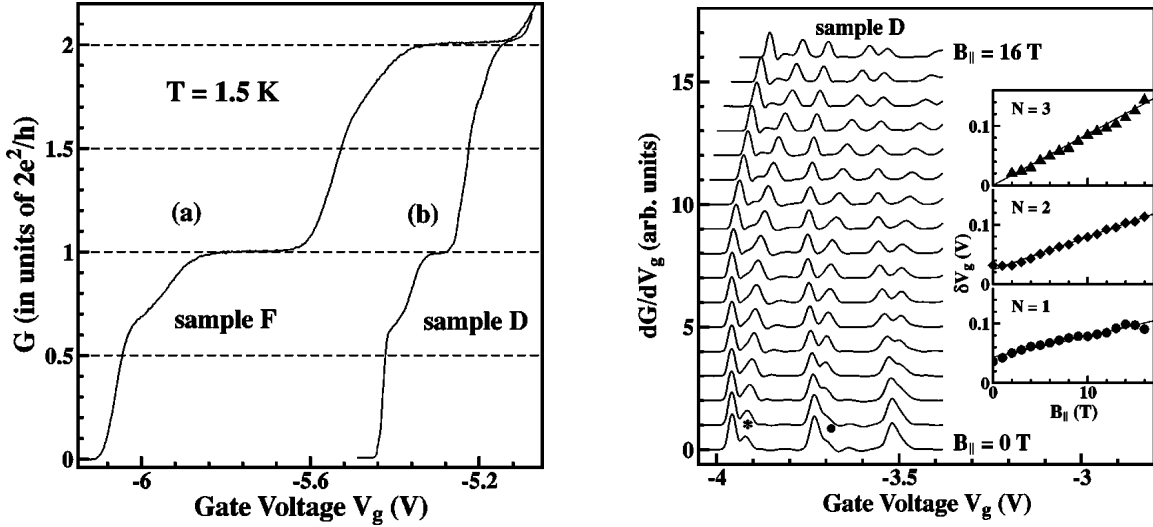


Figure 4.8: Transconductance traces and linear conductance as a function of the gate voltage, measured by Thomas et al. and taken from [48]. Left panel: the conductance trace defined in a quantum well (a) and a conventional heterostructure (b). Transconductance traces dG/dV for $N = 1, 2, 3$ and different in-plane magnetic fields from $B = 0T$ to $B = 16T$ in increments of $1T$, where the insets show the resulting energy splitting ΔE .

is plotted for different magnetic fields and different temperatures. For increasing temperatures, the structure of the spin-degenerate and spin-resolved plateaus weakens, because of thermal smearing, until they vanish almost completely at $T = 2.8$ K. The opposite behaviour holds for the intermediate step of the 0.7 anomaly, it strengthens and is the only surviving structure for $T = 2.8$ K.

The magnetic field behaviour of the different spin-degenerate subbands is quite the same, the conductance plateaus evolve smoothly from above into the corresponding spin-resolved plateaus. For higher magnetic fields, ΔE becomes linear in B , equivalent to the usual Zeeman effect, with the difference of a high-field offset ΔE_{hfo} if the linearization is extended to $B = 0T$. Therefore, an effective g -factor $|g^*|$ can be defined in the high-field regime via $\mu_B |g^*| = d\Delta E/dB$. This effective g -factor is strongly enhanced and has values up to three times the g -factor for bulk 2DEG material. This enhancement can be explained by an exchange interaction [19, 40]. Calculations and experiments, see [25] and references therein, show that the effective g -factor decreases, if the transverse confinement weakens. This implies that for a harmonic potential $|g^*|$ scales as the subband spacing $\hbar w_{12}$. For higher subband indexes N , the confinement weakens and, hence, the effective g -factor is supposed to decrease.

The authors also investigated the dependence of $\Delta E_{0.7}$ and ΔE_{hfo} on the QPC geometry parameters L and W . They understand the high-field offset ΔE_{hfo} as determinant of a "field-independent exchange effect that results from each subband being in a ferromagnetic spin-polarized state" [25]. They found that these splittings depend irregularly on the parameters L, W and show a striking correlation for $N = 1$. This correlation is said

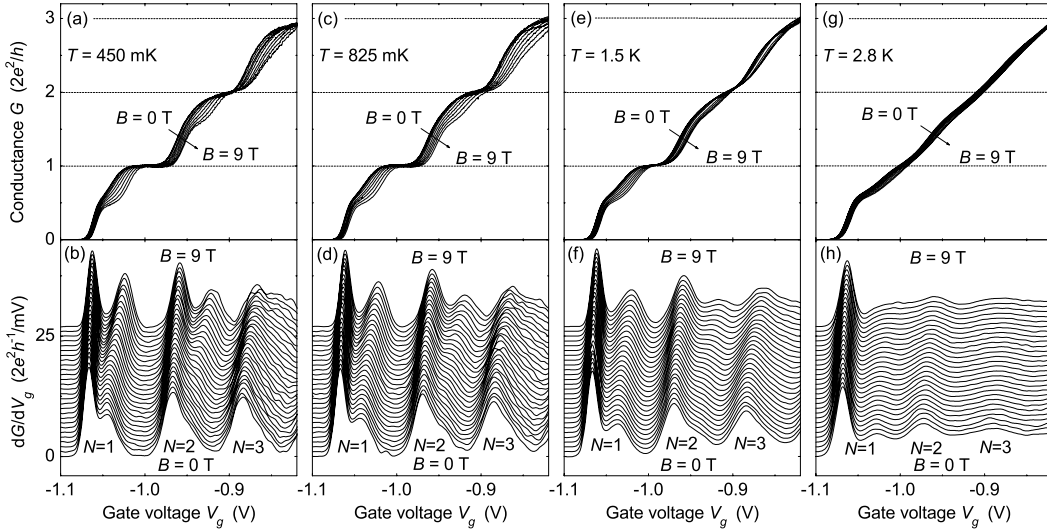


Figure 4.9: Linear conductance and transconductance traces as a function of the gate voltage, taken from [25]. Upper panels: Linear conductance G versus gate voltage V_g for different in-plane magnetic fields from $B = 0 T$ to $B = 9 T$, measured in a QPC with $L = 300 nm$ and $W = 400 nm$. Bottom panels: Transconductance dG/dV_g traces derived from the upper panels. The temperature is varied from the left panels (a), (b) to the right panels (g), (h), with $T = 0.45, 0.825, 1.5$ and $2.8 K$.

to provide evidence that the spontaneous splitting of the 0.7 anomaly is dominated by this exchange splitting, which causes the offset of ΔE_{hfo} . The same analysis for higher subbands $N = 2, 3$ provides a significantly smaller and often almost vanishing high-field splitting, that is in agreement with the almost completely vanishing zero-field splitting.

The correlation between $\Delta E_{0.7}$ and ΔE_{hfo} is persistent for higher temperatures and has a very different temperature behaviour compared to $|g^*|$. Therefore, the authors concluded, "this indicates that the g-factor enhancement and the 0.7 anomaly arise from different many-body effects" [25].

4.4.3 Microscopic models

There are numerous theoretical approaches to explain the physical origin of the anomalous conductance behaviour in QPC geometries. Most of them are based on the electron-electron interaction. Several authors suggested a spontaneous spin splitting, which is even persistent for zero magnetic field [49, 48, 21, 44, 43]. Other microscopic models are based on electron back-scattering from acoustic phonons [46], the formation of Wigner crystal formation [30] or a dynamical Coulomb blockade [8]. Just to name a few of them, compare the introduction of Koop [25]. In the following, we want to introduce two theoretical approaches more precisely, the Kondo related model of Meir et al. and the model of Lunde et al., which is based on momentum-non-conserving e-e scattering processes.

The Kondo related model of Meir et al. [34, 45, 33], which is motivated by the work of

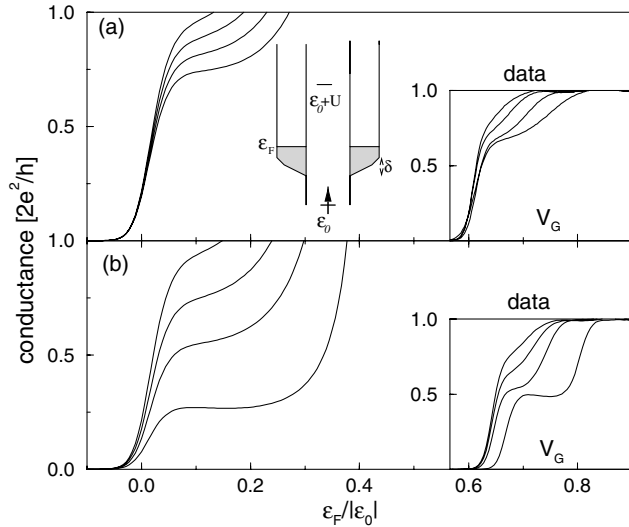


Figure 4.10: Results of the conductance for the Kondo-related model of Meir et al., taken from [34]. (a) Conductance versus Fermi energy ϵ_F for different temperatures, $T = 0.05, 0.1, 0.2, 0.6$ (from high to low). Right inset: experimental conductance for different temperatures [10]. Center inset: band structure for the Anderson model. (b) Conductance versus Fermi energy ϵ_F at $T = 0.06$ for different magnetic fields, Zeeman splitting $\Delta = 0, 0.07, 0.12, 0.4$ (from top to bottom). Inset: experimental conductance for different magnetic fields [21].

Cronenwett et al. [10], assumes the formation of a quasi-localized electron state near the pinch-off in the QPC. This assumption has been corroborated by spin-density functional theory (SDFT) calculations [33]. The spin-dependent transmission between this localized state and electrons in the reservoirs leads to a localized dynamic magnetic moment in the QPC. A configuration equivalent to a localized spin in a quantum dot or on an impurity develops, and Kondo physics comes into play. In the 0.7-anomaly regime, the conductance behaviour can be explained by a fully transmitting first subband and Kondo-like physics for the second subband. Hence, the conductance is mainly carried by one transmission channel and leads to a reduced shot noise³, which is in agreement with experiments [15]. In this approach the conductance decreases in the 0.7-anomaly regime, due to Coulomb blockade, and has a value between $0.5 - 1 \times G_0$. When the gate voltage becomes less negative, the Coulomb blockade can be overcome and the conductance reaches G_0 . Meir et al. explain the anomalous temperature behaviour with the Kondo effect of the quasi-bound electron state in the QPC. If the temperature is below the Kondo temperature, the local magnetic moment is screened and leads to an enhanced conductance compared to higher temperatures. This Kondo correlation is destroyed if the strength of an applied magnetic field reaches the order of the Kondo temperature. In figure 4.10 the results are presented that are obtained by a generalized Anderson model, describing the localized state, and perturbation theory. Another statement of the authors is that a quasi-localized state will also form if the magnetic field is so high that opposite spin-split subbands of two different neighbouring QPC modes intersect. But, due to the strength of the magnetic field they, assume that no Kondo physics will occur in this intersection region. The formation of a quasi-localized state for higher spin-degenerate subbands depends on the parameters of the QPC, which is in contrast to the first subband. They explain that phenomena as follows.

³A pedagogical introduction of the theory of quantum shot noise can be found in [5], for a brief introduction see [4].

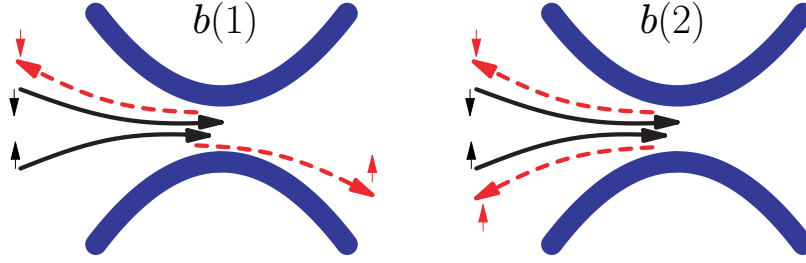


Figure 4.11: Illustration of the momentum-non-conserving e-e scattering processes $b(1)$ and $b(2)$, taken from Lunde et al. [29]. The full/dashed lines represent incoming/outgoing electrons. The thick blue lines represent the border of the QPC.

The polarization in the second mode induces a partial polarization in the first mode and leads to high energy costs.

The microscopic model of Lunde et al. [29] explains the conductance abnormality with electron-electron momentum-non-conserving scattering processes that change the number of left- and right-moving electrons, see figure 4.11. Such scattering processes are possible, because the translational invariance of QPC geometries are broken. The authors show, by computing the corresponding matrix elements with a WKB-ansatz in the regime of $\mathcal{T}_0 \approx 1$ ($\mathcal{T}_0 \hat{=}$ zero-temperature transmission probability) and low temperatures $T \ll T_F^l$ ($k_B T_F^l \hat{=}$ local Fermi energy), that this non-conserving scattering can lead to a significantly reduced conductance of the first quantized plateau for increasing temperatures. This temperature dependence can be understood by a growing phase space for inelastic scattering processes with temperature. These scattering processes are more relevant, if the Fermi wavelength is comparable to the extension of the QPC, due to a more dramatic breaking of the translational invariance. It follows that the momentum-non-conserving scattering processes and, hence, the conductance reduction is most prominent at the onset of the plateau and then decreases for larger electron densities. The authors were able to derive a functional dependence of the linear conductance for low temperatures and in the limit $\mathcal{T}_0 = 1$, which reads

$$G = G_0 \left(1 - A_b (\pi T / T_F^l)^2 \right). \quad (4.17)$$

Here, the dimensionless coefficients A_b are connected to the momentum-non-conserving scattering processes $b(1)$ and $b(2)$, which are said to cause the current reduction. The authors explain the experimentally not observed conductance reduction of the spin-split plateaus, that evolve in high magnetic fields, by the strong suppression of interaction effects due to the Pauli principle.

Chapter 5

fRG studies of quantum point contacts

In this chapter, we use the fRG approach of chapter 3 to study zero temperature linear conductance properties in quantum point contacts by applying a saddle point potential to the contact region. At first, we continue the work of Heyder [17] and extract an absolute energy scale h_ within an one-dimensional system. This will be done for data generated with the fRG approach of [3] (including nearest-neighbour vertex flow) and the fRG approach of section 3.3.1 (including on-site vertex flow) respectively. Furthermore, we present results of the magnetic field behaviour of higher conductance steps.*

5.1 Introduction

The functional renormalization group was the first time successfully used for studying zero temperature electron transport properties in quantum point contacts by Florian Bauer in 2008. In his master thesis [3], he set up a static fRG approach in the 1PI scheme which is able to deal with an extended one-dimensional interaction region and arbitrary static potentials applied to it. This was achieved by a parametrization of the self-energy and the effective interaction with respect to the site indices of the extended Hubbard model and by neglecting all elements without the same or at least neighbouring tensor indices. The validity of this approach was shown by using an extended quantum dot potential, where all important features of the Kondo resonance for zero bias voltage could be reproduced. For the study of quantum point contacts, a potential barrier was applied to the contact region, and the zero temperature linear conductance, electron g-factor, local density and shot-noise was investigated. Here, several striking agreements with experiments could be revealed which are the following ones, the spin-degenerate conductance plateau evolves from above into the spin-non-degenerate conductance plateaus for increasing magnetic fields, the pinch-off of this conductance plateau is hardly effected by the magnetic field, see figure 5.1, the effective g^* -factor is strongly enhanced and the shot-noise is reduced, see the inset of figure 5.1. These studies were proceeded by Jan Heyder within the scope

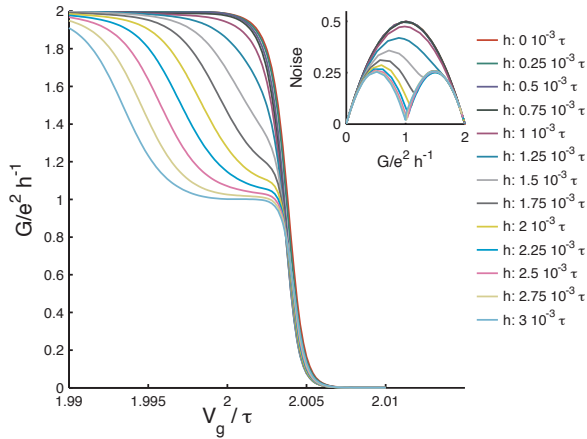


Figure 5.1: Linear conduction and shot noise for zero temperature obtained with the fRG approach, taken from [3]. Conduction as a function of the potential height, in the figure denoted with V_g , and shot noise as a function of the conductance (upper right inset), each for various magnetic fields from 0T to $3 \cdot 10^{-3}T$ in increments of $0.25 \cdot 10^{-3}T$.

of his master thesis [17]. He investigated the smooth crossover between a quantum dot (QD) and a quantum point contact (QPC), by modelling a continuous parametrization from a potential landscape with two barriers (QD regime) towards a potential with a single barrier (QPC regime). Within the crossover, he studied the development of the linear conductance, local charge n_n , local magnetization m_n , local zero-field susceptibility $\chi_n = \partial_h m_n|_{h=0}$ and the total susceptibility $\bar{\chi} = \sum_n \chi_n$. He found several signs that the anomalous magnetic field behaviour of the zero temperature conductance in QPCs is closely related to the Kondo effect. These indices are the following ones, the linear conductance evolves smoothly from an odd Kondo plateau, with an odd number of electrons occupying the QD, to the 0.7-like shoulder of the QPC for intermediate Zeeman energies, the local susceptibility is strongly enhanced in regions of low charge densities in both regimes and, furthermore, a low energy scale h_* with $\log h_* \propto (\tilde{V}_g - \tilde{V}_g^0)/w$ occurs, which is related to the total susceptibility during the whole crossover via $h_* = 1/(\bar{\chi} - \chi_0)$.

In this chapter, we apply the two-dimensional fRG approach of chapter 3 to study zero temperature zero bias voltage electron transport properties in quantum point contacts. Where the general theoretical background of quantum point contacts was given in the previous chapter. We proceed the studies of [17] and try to extract a functional dependence of the energy scale h_* with respect to the interaction strength, the height and curvature of the potential. Furthermore, we present first results of the magnetic field behaviour of higher conductance plateaus.

5.2 Modelling a quantum point contact

With the two-dimensional Hubbard model of section 3.2.2, which consists of a contact region coupled to two semi-infinite leads, we model a quantum point contact by applying an appropriate potential to the contact/interaction region. Here, a saddle-point model is most reasonable for two-dimensional systems, compare subsection 4.3.2.

In the following, we will restrict ourselves to rather narrow systems $M < 10$ due to

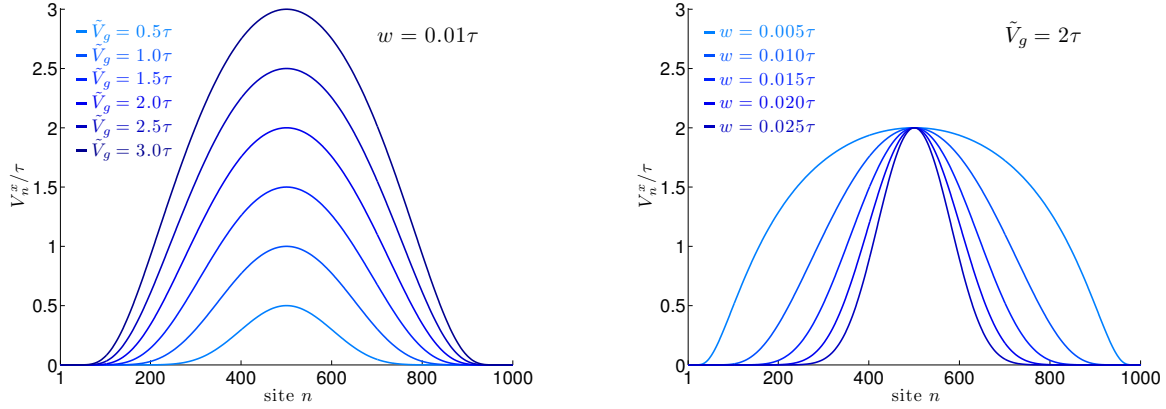


Figure 5.2: Illustration of the one-dimensional potential barrier V_n^x for various potential heights and curvatures. Left panel: the potential as a function of the site n with fixed $w = 0.01\tau$ and \tilde{V}_g ranging from 0.5τ to 3.0τ in increments of 0.5τ . Right panel: the potential as a function of the site n with constant $\tilde{V}_g = 2\tau$ and curvatures ranging from 0.005τ to 0.025τ in increments of 0.005τ . In each panel the length of the potential is $N = 1000$.

numerical costs and, therefore, we won't be able to model a realistic crossover from the extended two-dimensional electron gas to the narrow quasi one-dimensional constriction. Hence, our model neglects all physical effects due to this vast reduction of the transversal extension, for example transitions of the transversal eigenstates, and inherits only the constriction and pinch-off of the last remaining transmission modes at the center of the quantum point contact. Whether the physics of this crossover is considerable or not depends on the specific experimental setup, but it should be negligible if the potential at the beginning of the QPC varies slowly and an adiabatic approximation is valid.

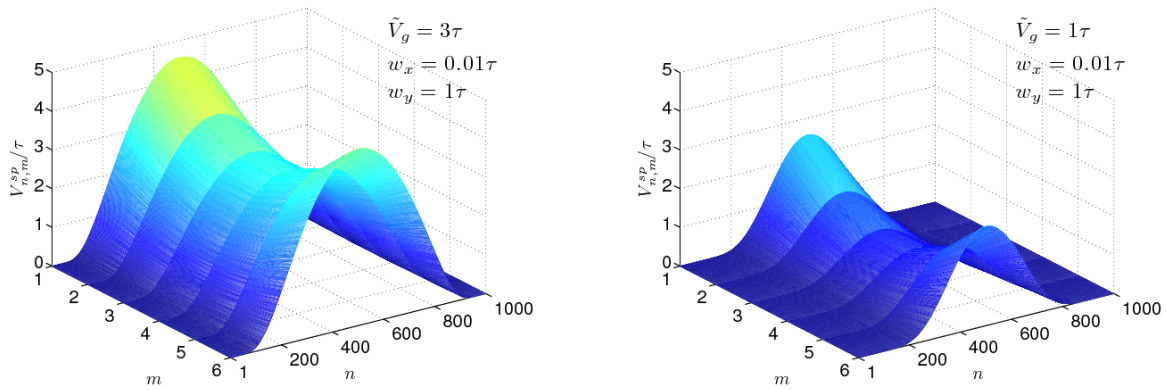


Figure 5.3: Illustration of the saddle point potential V_n^{sp} for different potential heights. The extension of the potential is $N = 1000$ times $M = 6$ and its curvature in longitudinal and transversal direction (at the center) are $w_x = 0.01\tau$ and $w_y = 1\tau$. In the left or right panel is the potential height (at the center) $\tilde{V}_g = 3\tau$ or $\tilde{V}_g = 1\tau$.

Although, the curvatures at the center of the saddle point potential change with the gate

voltage in real experiments, we implement a constriction potential where the curvatures are fixed for all potential heights¹, which enables us to extract the influence of these parameters on the conduction behaviour. For our proceeding numerical calculations, we use V^x for studies of one-dimensional systems and V^{sp} for studies of two-dimensional systems. In figure 5.2 and 5.3, these potentials are illustrated. The corresponding formulas are

$$V_{n,m}^{sp}(\kappa_x, \kappa_y, \tilde{V}_g) = V_n^x(\kappa_x, \tilde{V}_g) + V_n^x(\kappa_x, 1)V_m^y(\kappa_y), \quad (5.1)$$

where

$$V_m^y(\kappa_y) = 1/2 \kappa_y (m - m_0)^2 \quad (5.2)$$

and

$$V_n^x(\kappa, \tilde{V}_g) = \tilde{V}_g \exp\left(-\frac{(n - n_0)^2}{\alpha^2 - \beta^2(n - n_0)^2}\right) \quad \text{with} \quad \alpha^2 = \frac{2\tilde{V}_g}{\kappa}, \quad \beta^2 = \frac{\alpha^2}{(1 - n_0)^2}. \quad (5.3)$$

Here, \tilde{V}_g is the potential height and $\kappa_{x/y}$ the curvatures² in x/y -direction at the center (n_0, m_0) of the potential. In the following, we don't use κ as parameter for the curvature but rather $\hbar w$, the energy splitting in a harmonic potential with $\kappa = mw^2$. The connection between these parameters, in our discrete model, is

$$w = \sqrt{2\kappa\tau}, \quad (5.4)$$

which follows from the formula of τ given in equations (3.3). The units are chosen in such a way, that the lattice parameters and \hbar is one. Due to the narrow width M of our system, we obtain only a pseudo-harmonic potential in transversal direction, which is dominated by the fixed boundary conditions. Therefore, we can't expect an equidistant energy splitting w_y of the transmission modes.

For the site-dependent magnetic field $h_{n,m}$ and the on-site interaction $U_{n,m}$ of our two-dimensional Hubbard model of section 3.2.2, we use a constant field with value h and U respectively. To avoid oscillations, we implement these potentials in such a way, that they exponentially decrease at the boarder of the contact region.

In our model Hamiltonian, we set the g -factor equal minus one, compare 3.8.

5.3 Energy scale h_*

In his master thesis [17], Jan Heyder found a quadratic dependence of the linear conductance G and the magnetic field in the low-field regime for an one-dimensional extended Hubbard model, where the data were generated with the fRG approach of Bauer [3]. He showed that a low energy scale h_* can be defined by this quadratic dependence via

$$G(h) = G(h=0) [1 - (h/h_*)^2], \quad (5.5)$$

¹For the connection between the gate voltage and the height of the potential at the center we refer to section 4.3.2.

²The curvature is equivalent to the second derivative at critical points, compare [6, equ. 3.435].

where the magnetic field h must be small enough, see figure 5.5. This energy scale depends on the gate voltage \tilde{V}_g and changes in a characteristic way if the transmission channel opens, see figure 5.4. It is dominated by two areas with exponential growths

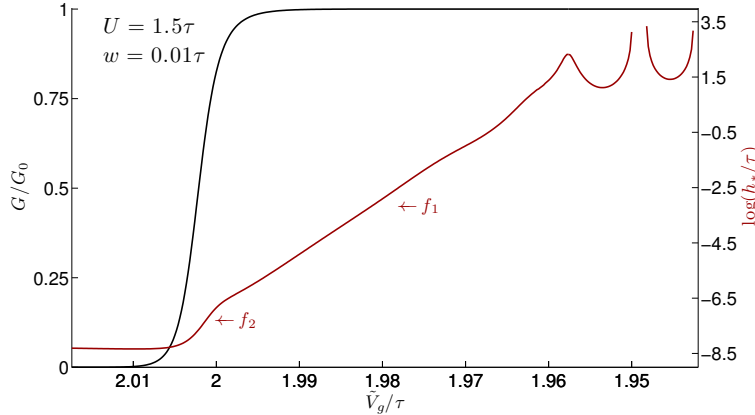


Figure 5.4: Energy scale h_* and conductance as a function of the potential height \tilde{V}_g . The data is generated for a potential barrier with $w = 0.01\tau$ and interaction strength $U = 1.5\tau$, $U' = U/10$, by using the fRG approach of Bauer [3].

$h_* \propto \exp(-f_{1/2}(w, U)\tilde{V}_g)$, which are indicated in the $\log(h_*/\tau)$ plot by two linear slopes. We call these slopes analogously to Heyder f_2 and f_1 . The exponential increase, corresponding to f_2 , starts when the transmission of the subband reaches a non-negligible value and ends if the transmission is almost one. This exponential behaviour crosses over to the exponential increase, corresponding to f_1 , which is persistent for a huge range of \tilde{V}_g , where the transmission is just one, and ends in some parabolic structures. These parabolic curves evolve for increasing U and have similarities to the T_K -curves in quantum dots [17]. The behaviour of f_1 is stable under the variation of the curvature w , the form of the potential barrier and the interaction strength U . The same holds for f_2 , with the difference, that its appearance depends on the interaction strength.

The definition of the low-energy scale h_* , see (5.5), was introduced within the scope of an one-dimensional system and a single transmission mode. The extension to higher spin-degenerate subbands is obvious, we define for each subband n an equivalent energy scale $h_*^{(n)}$ via

$$G_{nn}(h) = G_{nn}(h=0) \left[1 - (h/h_*^{(n)})^2 \right], \quad (5.6)$$

where $G_{nn} := G_0 \mathcal{T}_{nn}$ is the contribution to the conductance of the n th transmission mode.

In the following section, we continue the previous work of Heyder [17] and investigate the dependence of the energy scale h_* on the potential curvature w and the interaction strength U in an one-dimensional system. We will do this separately for data generated with two different fRG approaches. First, the fRG implementation introduced in [3] denoted by fRG approach including nearest neighbour vertex flow. This approach is also able to take nearest neighbour interactions U' into account. Second, the fRG implementation of section 3.3.1 denoted by fRG approach including on-site vertex flow. This approach is not able to take nearest neighbour interactions into account. To obtain comparable results with previous studies, we set analogously to [3, 17] $U' = U/10$. At the end we compare the energy scale for these two approaches and investigate the influence of the nearest neighbour interaction U' on the energy scale.

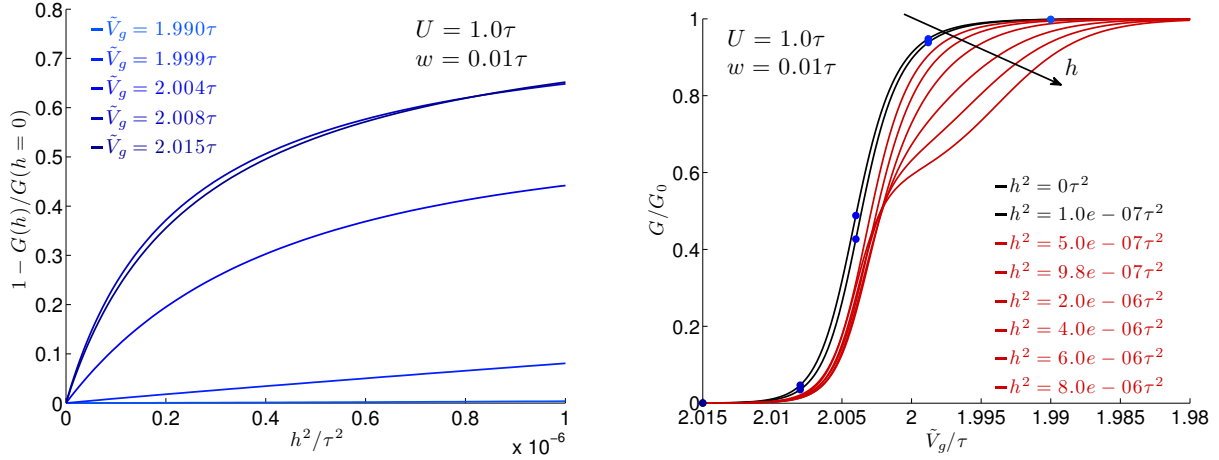


Figure 5.5: Magnetic field range of the well-definedness of the energy scale h_* . The parameters are $U = 1\tau$ with nearest-neighbour interaction $U' = U/10$ and $w = 0.01\tau$. Left panel: $1 - G(h)/G(h=0)$ as a function of h^2 for five gate voltages from 1.99τ to 2.015τ . Right panel: the conduction as a function of the potential height \tilde{V}_g for various magnetic fields. The black or red conductance traces correspond to magnetic fields for that the well-definedness of h_* holds or not holds. The blue dots represent the conductance values of the black traces for the potential heights of the left figure.

5.3.1 Non-interacting model

Before we extract an absolute energy scale for an interacting model, we discuss the non-interacting case. The purpose is to obtain reference values in the limit $U/\tau \rightarrow 0$ and to see which structures of h_* are already inherited in the non-interacting case. Using the transmission probability for the saddle-point constriction potential (4.10), which reads

$$\mathcal{T}_{nn}(E) = \frac{1}{e^{-2\pi\tilde{E}_n/w_x} + 1} \quad \text{with} \quad \tilde{E}_n = E - w_y\left(n + \frac{1}{2}\right) - \tilde{V}_g, \quad (5.7)$$

where $\hbar = 1$, we can easily calculate the corresponding energy scale $h_*^{(n)}$. After a short calculation, we obtain

$$h_*^{(n)} = \frac{\sqrt{2}}{\pi} \frac{1 + e^{2\pi\tilde{E}_n/w_x}}{\sqrt{-1 + e^{2\pi\tilde{E}_n/w_x}}}. \quad (5.8)$$

For high energies or low gate voltages \tilde{V}_g , in the sense of $\tilde{E} \gg w_x$, this leads to the exponential growth

$$h_*^{(n)} = \sqrt{2}/\pi \exp(\pi\tilde{E}_n/w_x) \quad (5.9)$$

and hence

$$\ln(h_*^{(n)}) \propto -\pi \frac{\tilde{V}_g}{w_x} \quad \text{for} \quad \tilde{E}_n \gg w_x. \quad (5.10)$$

The minimum of this scale is given for $\tilde{E}_n = \tilde{E}_n^{\min}$, where

$$\tilde{E}_n^{\min} = \frac{\ln(3)}{2\pi} \quad \text{and} \quad h_*^{(n)}(\tilde{E}_n^{\min}) = \frac{4}{\pi} \hbar w_x. \quad (5.11)$$

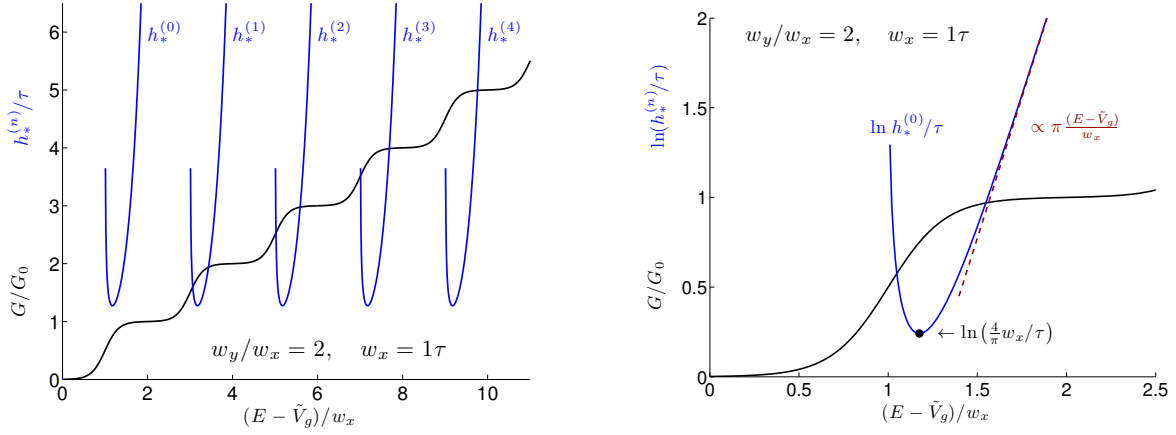


Figure 5.6: Energy scale h_* for a saddle-point constriction model in a non-interacting systems. The conductance (black lines) and the energy scales $h_*^{(n)}$ (blue lines in the left panel) and the logarithm $\log(h_*^{(0)}/\tau)$ (blue line in the right panel) are plotted as functions of the normalized energy $(\mu - \tilde{V}_g)/w_x$, where the curvature parameters are $w_x = 1$ and $w_y = 2$.

In figure 5.6, we illustrated h_* for a non-interacting system. The main difference, compared to an interacting system, is the boundedness of h_* to higher transmission probabilities $\mathcal{T}_{nn} > 1/2$. For $\mathcal{T}_{nn} < 1/2$, the conductance increases and, therefore, becomes imaginary, compare subsection 4.3.3. If the transmission probability is one half, which is equivalent to $\tilde{E}_n = 0$, the energy scale of the corresponding transmission mode diverges because the conductance is invariant with respect to the magnetic field at this point. For every subband n , the low-energy scale $h_*^{(n)}$ has the same form. They are shifted by w_y with respect to each other, similar to the conduction plateaus.

5.3.2 Nearest neighbour vertex flow

Before we extract a functional dependence of h_* on the curvature and the interaction strength, we want to discuss the general influence of these parameters on the low-energy scale. Therefore, we plotted its logarithm $\log(h_*/\tau)$ as a function of the potential height and the interaction or the curvature in figure 5.7 or 5.8, which was already partially done in [17].

In figure 5.7, we observe, that the logarithm develops smoothly for increasing interaction strengths from the hook-like structure of the non-interacting model to the typical structure of the interacting system, we described previously. This crossover takes place within a small region of $\Delta U < 0.4\tau$. Having a look on the linear slopes $f_{1/2}$, we see that f_1 already occurs in the non-interacting model and is persistent throughout the range of investigated interaction energies and curvatures, where its gradient decreases for increasing U . This is in contrast to the straight line f_2 which forms in the pinch-off region only for evaluated values, in our case approximately $U \gtrsim 0.5\tau$. The slope f_2 becomes steeper for increasing interaction strengths. The red traces 1), 2), 3) in figure 5.7, 5.8 denote $\log(h_*/\tau)$ at potential heights

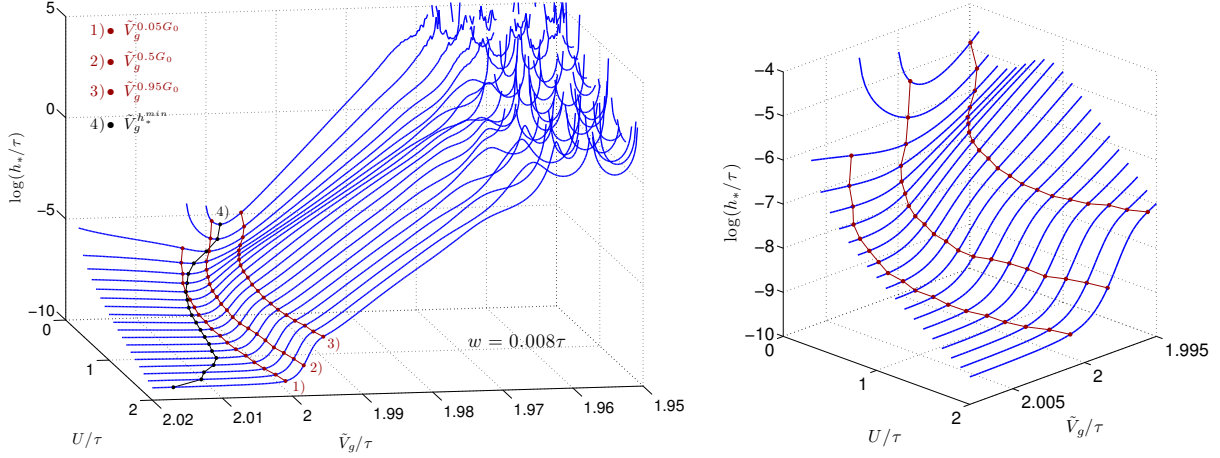


Figure 5.7: Three-dimensional graph of $\log(h_*/\tau)$ as a function of the potential height and the interaction for data generated with the fRG approach including nearest neighbour vertex flow [3] and $U' = U/10$. The curvature of the potential is $w = 0.08\tau$ and U varies from 0.1τ to 2.0τ increments of 0.1τ . The red traces 1), 2), 3) visualizes the logarithm of h_* for potential heights, where the conductance is 0.005, 0.5, 0.95 times G_0 . The black curve 4) follows the minimum of h_* and respectively of $\log(h_*/\tau)$. The right panel shows a close-up image of the pinch-off region obtained from the left panel, where we omitted the black curve \tilde{V}_g^{min} .

where the conductance is 0.05, 0.5 and 0.95 times the conductance quantum. Therefore, they are marking the pinch-off region.

For denoting potential heights relative to the conductance, we use the quantity $\tilde{V}_g^{xG_0}$ defined by

$$G(w, U, \tilde{V}_g^{xG_0}(w, U)) = x G_0, \quad (5.12)$$

where we understood the conductance as a function of w , U and \tilde{V}_g . To be consistent in the graphs, we also defined $\tilde{V}_g^{h_*^{min}}$ which is the value of \tilde{V}_g where h_* is its minimum.

Furthermore, we can see, that the area of the exponential growth is strongly correlated to the pinch-off region, which gives a hint how to obtain the desired functional dependence. The black trace 4) is the minimum of h_* and respectively $\log(h_*/\tau)$. Its behaviour, with respect to the interaction strength, seems not to be related with the conductance. The opposite holds for its behaviour with respect to w , as can be seen in figure 5.8. The position of the minimum only slightly changes with respect to $\tilde{V}_g^{0.05G_0}$. For increasing curvatures the pinch-off region broadens and, therefore, the $\log(h_*/\tau)$ curve also flattens.

Analysis of the exponential growth f_1

At first we want to investigate the most noticeable structure of this low energy scale, the exponential growth $h_* \propto \exp(-f_1 V_g)$ which starts when the transmission of the corresponding subband is approximately one. In section 5.3.1, we showed that this structure already occurs in the non-interacting case of a saddle point constriction model, with the

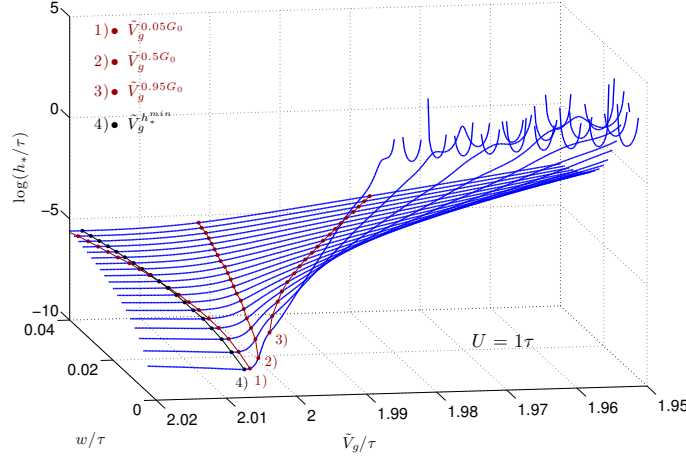


Figure 5.8: Three-dimensional graph of $\log(h_*/\tau)$ as a function of the potential height and the curvature for data generated with the fRG approach including nearest neighbour vertex flow [3] and $U' = U/10$. The interaction strength is $U = 1.0\tau$ and w varies from 0.004τ to 0.04τ in increments of 0.002τ . The red traces 1), 2), 3) visualizes the logarithm of h_* for potential heights, where the conductance is 0.005, 0.5, 0.95 times G_0 . The black trace 4) follows the minimum of h_* and respectively of $\log(h_*/\tau)$.

linear decrease

$$\log(h_*) \propto -\frac{\pi}{w} \tilde{V}_g \quad (5.13)$$

for the logarithm of the energy scale. For increasing U , it evolves continuously into f_1 of the interacting system. Therefore, we expect $f_1(w, U) \rightarrow \pi/w$ in the limit $U/\tau \rightarrow 0$. Jan Heyder already investigated f_1 for higher interaction strengths and found the functional dependence [17, equ. 5.18]

$$f_1(w, U) \sim 1.3 \frac{1}{w}, \quad (5.14)$$

where a distinct U -dependence couldn't be resolved and just an oscillatory behaviour around the value 1.3 is mentioned. In the following, we want to continue this work and try to obtain a functional dependence of f_1 on the interaction strength U .

We determine the gradient f_1 by performing the required linearisation $\log(h_*) = -f_1 \tilde{V}_g$ within an interval of range $\Delta \tilde{V}_g = 0.01\tau$ ($\hat{=}$ 50 data points), centered around a fixed \tilde{V}_g relative to the conduction trace. For the gradient f_1 , we find the expected linear dependence on the inverse of the curvature, see the left panel of figure 5.9, which was already reported in [17]. We define g_1 as the resulting gradient $f_1 \sim g_1/w$, and we plot this quantity as a function of the interaction U , see the right panel of figure 5.9. For small interaction strengths, the U -dependence can be linearized and we obtain $1/g_1(U) \sim \alpha U + \beta$, where β is in striking agreement with the expected value $1/\pi$ of the non-interacting model. This indicates the following functional dependence

$$f_1(U, w) \sim \frac{\pi}{(1 + \gamma U) w} \quad \text{with} \quad \gamma \sim 0.8 \quad (5.15)$$

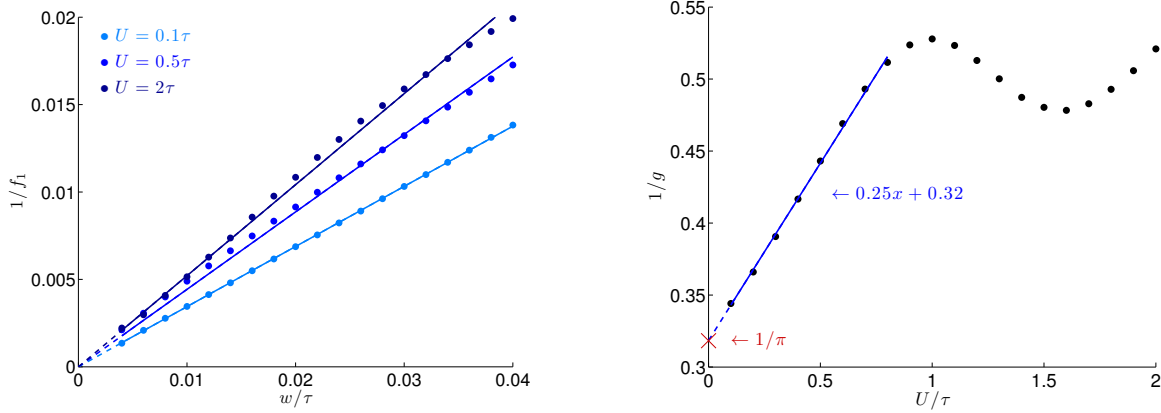


Figure 5.9: Analysis of the exponential growth $\exp(-f_1 V_g)$ for data generated with the fRG approach including nearest neighbour vertex flow [3] and $U' = U/10$. Left panel: linearisation of the inverse slope $1/f_1$ with respect to the curvature w , exemplarily illustrated for $U = 0.1, 0.5\tau$ and 2τ . Right panel: the resulting gradients of this linearisation $1/g_1 \sim 1/(f_1 w)$ as a function of the interaction. The blue line represents the linearisation for small U and the red cross corresponds to the theoretical prediction for the non-interacting model, see equation (5.9).

for small U , in explicit terms $U \lesssim 0.9\tau$. Therefore, the linear slope f_1 becomes flatter for increasing interaction strengths, and the proportionality factor of $f_1 \propto 1/w$ ranges from approximately 3.1 to 1.8 in the interaction regime where (5.15) is valid. For higher values, $U \gtrsim 0.9\tau$, we can confirm an oscillatory behaviour around the value of 2 with an amplitude of about 0.2

$$f_1(U, w) \sim (2 \pm 0.2) \frac{1}{w}, \quad (5.16)$$

which corresponds to an oscillation around $2/\sqrt{2} \approx 1.4$ in units of [17]. Therefore, the exponential growth f_1 seems to be approximately U -independent for higher interaction strengths $U \gtrsim 1\tau$, at least in the regime we investigated.

Analysis of the exponential growth f_2

Now, we want to study the second exponential growth $h_* \propto \exp(-f_2 V_g)$ of the energy scale which evolves for higher interaction strengths within the pinch-off region and, hence, it seems to be a special feature of the interacting system. This exponential behaviour was discovered by Jan Heyder [17, chap. 5.3.5], but he no functional dependence on the parameters w, U was stated and, therefore, we want to make up for that.

We determine the gradient f_2 of the corresponding straight line as follows. We observe, that this linear increase always forms for evaluated interaction strengths in a regime of \tilde{V}_g , where the conductance increases from 0.5 to 0.75 times the conductance quantum, compare the upper panels of figure 5.10. For very small values, the logarithm of the energy scale has a hook-like structure and no exponential growth f_2 can be observed. Therefore, we have to distinguish between parameters (w, U) , for that a linearisation is possible or not.

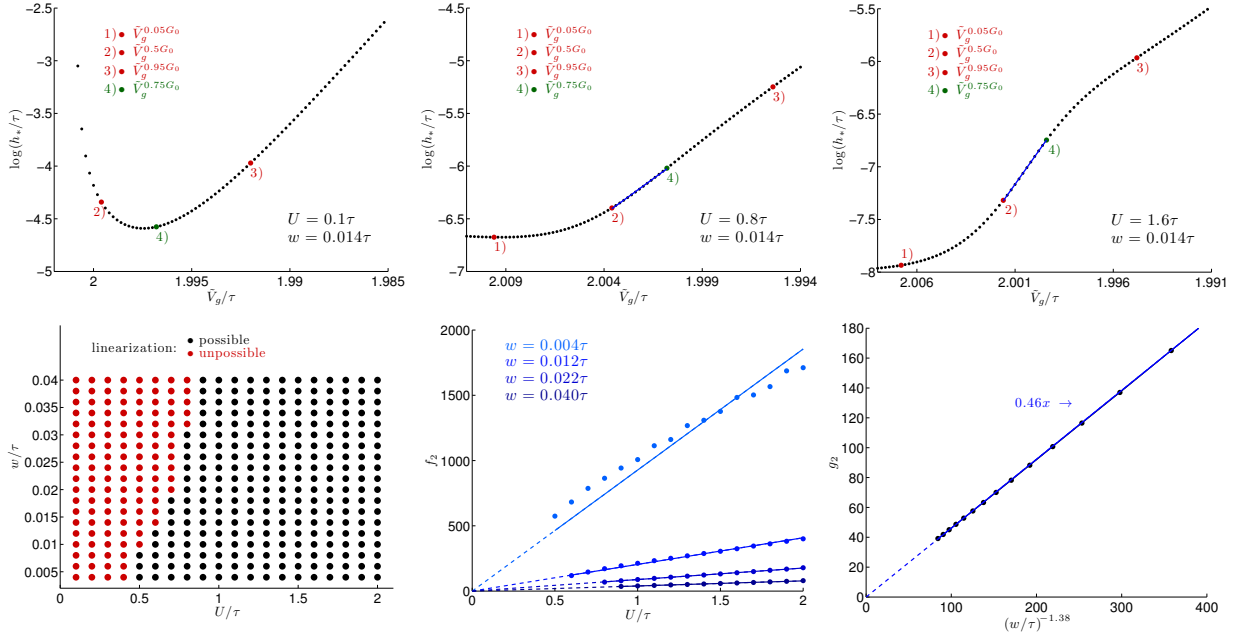


Figure 5.10: Analysis of the exponential growth $\exp(-f_2\tilde{V}_g)$ for data generated with the fRG approach including nearest neighbour vertex flow [3] and $U' = U/10$. Upper panels: the logarithm $\log(h_*/\tau)$ as a function of the potential height for fixed $w = 0.014\tau$ and $U = 0.1, 0.8, 1.6\tau$. The points 1) to 4) represent characteristic values regarding the conductance. Bottom left panel: the black/red dots represent parameters (w, U) for that a linearisation between 2) and 4) is possible/not possible. Bottom middle panel: linearisation of f_2 as a function of U exemplary for $w = 0.004, 0.012, 0.022\tau$ and 0.04τ . Bottom right panel: linearisation of the resulting gradients $g_2 \sim f_2/U$ with respect to $w^{-1.38}$.

This was done in the bottom left panel of figure 5.10, where we call a linearisation possible whenever the coefficient of determination fulfils $R^2 > 0.998$. In the bottom middle panel of the last-named figure, the corresponding gradients f_2 of the linear increase are plotted as a function of the interaction, where a linear dependence $f_2 \sim g_2 U$ is observable. And the right panel of figure 5.10 shows a linear dependence of g_2 on the curvature. This indicates the following functional dependence

$$f_2(w, U) \sim \alpha \frac{U}{w^\beta} \quad \text{with} \quad \alpha \sim 0.46, \beta \sim 1.38. \quad (5.17)$$

We conclude, the slope f_2 always forms between $\tilde{V}_g^{0.75G_0}$ and $\tilde{V}_g^{0.5G_0}$, increases linearly in the interaction U and is suppressed for evaluated values of w , in the sense of a flatter slope and the need of higher interaction strengths for its appearance.

Analysis of $h_*^{0.5G_0}$

Up to now, we have analysed the characteristic exponential growths $\exp(-f_{1/2}\tilde{V}_g)$ of the low energy scale. In the following, we want to investigate $h_*^{0.5G_0}$, which is equivalent to

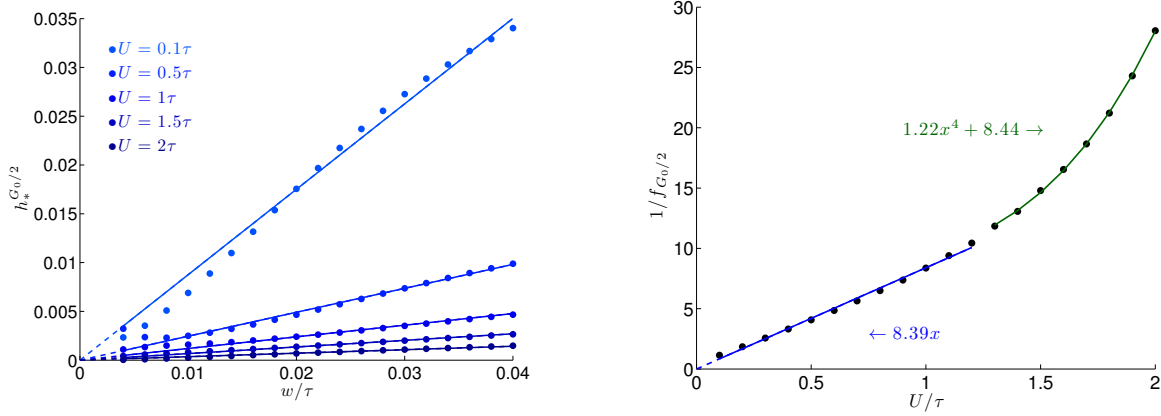


Figure 5.11: Analysis of the absolute value $h_*^{0.5G_0}$ for data generated with the fRG approach including nearest neighbour vertex flow [3] and $U' = U/10$. Left panel: linearisation with respect to w , exemplarily illustrated for $U = 0.1, 0.5, 1, 1.5\tau$ and 2τ . Right panel: the inverse of the resulting gradients $f_{0.5G_0} \sim h_*^{0.5G_0}/w$ as a function of U , where the blue or green lines are fittings in the low or high interaction regime.

h_* evaluated at the potential height where the conductance is one-half of the conductance quantum, in explicit terms

$$h_*^{0.5G_0}(w, U) := h_*(w, U, \tilde{V}_g^{0.5G_0}(w, U)), \quad (5.18)$$

where we understood h_* as a function of w , U and \tilde{V}_g . The evaluation of this quantity will enable us to set up a formula for the absolute value of the exponential growth $h_* \propto \exp(-f_2 \tilde{V}_g)$.

In the left panel of figure 5.11, we plotted this quantity as a function of the interaction strength U , which reveals an approximate linear dependence on w , $h_*^{G_0} \sim f_{0.5G_0} w$. The validity of this linearisation becomes worse for decreasing U . In the right panel of the last-named figure, we visualized the inverse of the corresponding constant of proportionality as a function of the interaction strength. We can observe a linear increase for small U , which evolves into a quartic behaviour for evaluated values of the interaction. This indicates the following dependence

$$h_*^{0.5G_0} \sim \alpha \frac{w}{U} \quad \text{with} \quad \alpha \sim 0.12 \quad (5.19)$$

for small interaction strengths $U \lesssim 1.3\tau$ and

$$h_*^{0.5G_0} \sim \alpha \frac{w}{1 + \beta U^4} \quad \text{with} \quad \alpha \sim 0.12, \beta \sim 0.14 \quad (5.20)$$

for higher values, in explicit terms $U \gtrsim 1.3\tau$. The number one in the denominator can't be neglected, at least in the interaction regime we studied. A divergence in U of the form (5.19) was to be expected, because h_* evolves into the hook-like structure for decreasing U , with a clear divergence at \tilde{V}_g where the conductance is one half of G_0 in the non-interacting model. The derived functional dependencies of $h_*^{0.5G_0}$ are in agreement with the observation, that

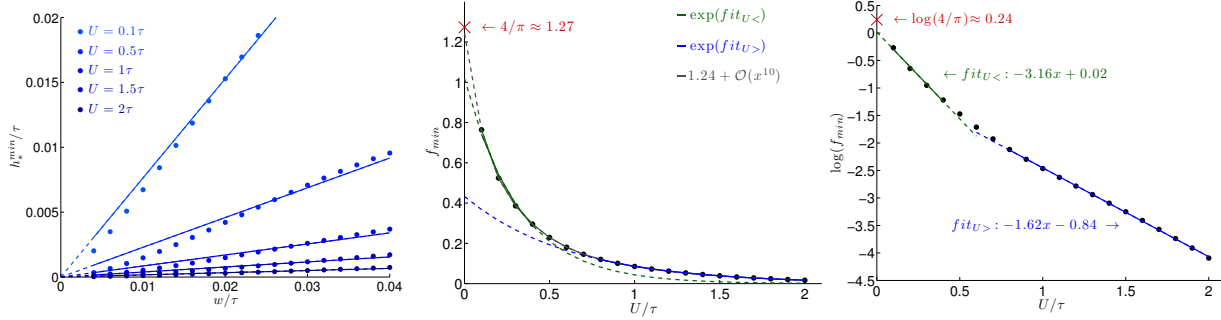


Figure 5.12: Analysis of the minimum h_*^{min} for data generated with the fRG approach including nearest neighbour vertex flow [3] and $U' = U/10$. Left panel: linearisation with respect to w exemplary for $U = 0.1, 0.5, 1, 1.5, 2\tau$. Middle panel: the resulting gradients $f_{min} \sim h_*^{min}/w$ as a function of U . The grey line shows the fitting using a high-ordered polynomial and the green or blue line represent the results for the fittings of $\log(f_{min})$ using $fit_{U<}$ or $fit_{U>}$. Right panel: the logarithm $\log(f_{min})$ versus the interaction strength U , where the green or blue line illustrates the linearisation within a low ($fit_{U<}$) or high ($fit_{U>}$) interaction regime. The red cross corresponds to the theoretical prediction for the non-interacting model, compare equation (5.11).

$\log(h_*/\tau)$ increases or decreases in the regime $\tilde{V}_g \lesssim \tilde{V}_g^{0.5G_0}$ with respect to the curvature or the interaction strength.

Analysis of h_*^{min}

The second absolute value of the low energy scale, we are going to investigate, is its minimum h_*^{min} . In our studies, it turned out that this quantity isn't useful for setting up an absolute functional dependence of the energy scale, but it provides us with useful information about the influence of the interaction on our system.

In section 5.3.1, we calculated this quantity in the non-interacting model and discovered a linear dependence on the frequency w , which reads

$$h_*^{min} = \frac{4}{\pi}w. \quad (5.21)$$

This dependence also holds in the interacting case, as can be seen in figure 5.12, where we illustrated the linearisation for some interaction values. But against our initial expectations, this linearisation is more valid for higher interaction strengths than for smaller ones. The resulting gradients $f_{min} \sim h_*^{min}/w$ have a complicated dependence on the interaction, as the middle panel of figure 5.12 shows. But for evaluated values of U an exponential dependence can be identified from the right panel of the last-named figure which indicates the following relation

$$h_*^{min} \sim \alpha w e^{-\beta U} \quad \text{with} \quad \alpha \sim 0.4, \beta \sim 1.6 \quad (5.22)$$

for $U \gtrsim 0.8\tau$. The analogue attempt for the low interaction regime doesn't provide adequate results. But a fit with a high-ordered polynomial provides good results with striking

agreement with the theoretical prediction for $U/\tau \rightarrow 0$. The first term provide the following relation

$$h_*^{min} \sim \frac{4}{\pi} (1 + \alpha U) w \quad \text{with} \quad \alpha \sim -5.3 \quad (5.23)$$

for $U < 0.2\tau$. Another promising approach, for deriving a more accurate dependence, is to fit $\log(f_{min})$ using a low-ordered polynomial.

Conclusion

In this subsection, we analysed various quantities which enable us to set up an absolute functional dependence of the exponential growth $\exp(-f_2 \tilde{V}_g)$ of the form

$$h_*(w, U, \tilde{V}_g) = \alpha(w, U) \times \exp\left(-f_2(w, U) \cdot \tilde{V}_g + \beta(w, U)\right). \quad (5.24)$$

The corresponding linear slope of $\log(h_*/\tau)$, f_2 , is given by its starting point $h_*^{0.5G_0}(w, U)$ and its gradient $f_2(w, U)$. This allows us to derive the following formula

$$h_*(w, U, \tilde{V}_g) = h_*^{0.5G_0}(w, U) \times \exp\left(-f_2(w, U) \left(\tilde{V}_g - \tilde{V}_g^{0.5G_0}(w, U)\right)\right) \quad (5.25)$$

which is valid for w and U , where the linearisation of f_2 is possible at all, and values of \tilde{V}_g which fulfil

$$\tilde{V}_g^{0.75G_0}(w, U) \lesssim \tilde{V}_g \lesssim \tilde{V}_g^{0.5G_0}(w, U). \quad (5.26)$$

Because this exponential growth forms for elevated interaction strengths, the choice of equation (5.20) for $h_*^{0.5G_0}(w, U)$ is most reasonable. Equation (5.25) is the main result of this subsection.

Since we determined the gradient f_1 analogously to f_2 - by performing the needed linearisation within an interval centered around a fixed \tilde{V}_g relative to the conductance - we could easily give an absolute functional dependence for this exponential scale, too. Because this exponential scale seems to be an artefact of the non-interacting system, and this scale is only modified for $U \neq 0$, and it occurs in a region where the transmission is one, we waive this analysis.

5.3.3 On-site vertex flow

In the last subsection, we performed a minute analysis of the functional dependence of the low-energy scale h_* on the interaction strength and the potential curvature, where the data was generated with the fRG approach including nearest neighbour vertex flow. Furthermore, we set the nearest neighbour interaction $U' = U/10$. Our method of section 3.3.1 is different and takes only on-site interaction into account. Therefore, we perform the same analysis using the fRG approach including on-site vertex flow. This is considerable, because we used $U' = U/10$ for nearest neighbour interaction in the last subsection, but this choice is rather arbitrarily. Furthermore, it is desirable to have a functional dependence of h_* for the proceeding studies of two dimensional systems, too. Because the following

proceeding is analogously to the last subsection, we will only briefly comment on the differences.

In figure 5.13 and 5.14, we illustrated the general dependence of the logarithm $\log(h_*/\tau)$ on the interaction and the curvature. For changing on-site interaction U , the hook-like structure of the non-interacting model evolves slower towards the typical structure of the interacting case and the gradient f_2 decreases slower. It is clearly noticeable that the minimum of the low-energy scale is now correlated with the conductance and is almost equivalent to the logarithm of h_* evaluated at $\tilde{V}_g^{0.05G_0}$. This holds for all curvatures and almost all interaction energies.

In figure 5.14, we chose a different illustration of the three-dimensional graph, which illustrates the w -dependence, compared to figure 5.13. By plotting $\log(h_*/\tau)$ as a function of $\Delta\tilde{V}_g/w$, the width of the pinch-off remains constant and the change of the structure of the low energy scale becomes observable. The gradients of the straight line f_1 are constant and only the structure in the region of the pinch-off seems to change. The additional exponential growth f_2 vanishes.

Analysis of the exponential growth f_1

In the case of the onsite vertex flow, the gradient shows also a linear dependence on the inverse of the curvature, $f_1 \sim g_1/w$, where the linear dependence of $1/g_1$ on the interaction strength holds for a slightly wider range of about $U \lesssim 1\tau$ and indicates

$$f_1(U, w) \sim \frac{\pi}{(1 + \gamma U)w} \quad \text{with} \quad \gamma \sim 0.6 \quad (5.27)$$

for this interaction regime, compare figure 5.15. The parameter γ is smaller and, therefore, the influence of the interaction on f_1 is weaker. For higher U , the oscillation in the case of nearest neighbour vertex flow vanishes, instead the influence of U on f_1 saturates around $U \sim 1.2\tau$ and afterwards begins to decrease linearly.

Analysis of the exponential growth f_2

The strict correlation between the exponential growth $\exp(-f_2V_g)$ and the transmission of the first spin-degenerate subband weakens. This holds especially for the lowest curvatures, as can be seen in the upper panels and the bottom left panel of figure 5.16. Nevertheless, we can perform the same analysis as before. Now we neglect the data for curvatures $w < 0.014\tau$, which leads to

$$f_2(w, U) \sim \alpha \frac{U}{w^\beta} \quad \text{with} \quad \alpha \sim 0.5, \beta \sim 1.3. \quad (5.28)$$

This dependence is almost identical to the corresponding results for data generated with the fRG approach including nearest neighbour vertex flow.

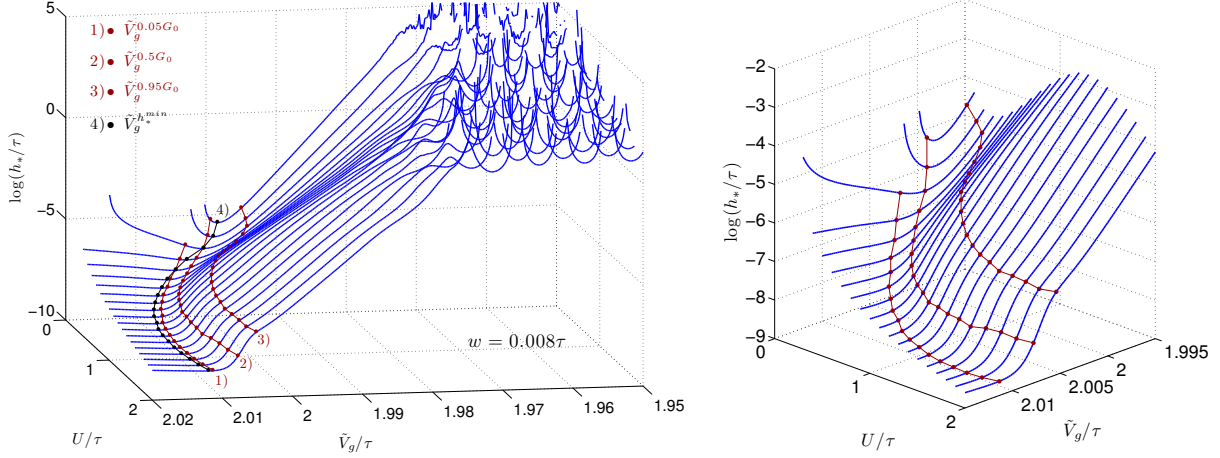


Figure 5.13: Three-dimensional graph of $\log(h_*/\tau)$ as a function of the potential height and the interaction for data generated with the fRG approach including only on-site vertex flow. The curvature of the potential is $w = 0.008\tau$ and U varies from 0.1τ to 2.0τ in increments of 0.1τ . The red curves 1), 2), 3) visualizes the logarithm of h_* for potential heights, where the conductance is 0.005, 0.5, 0.95 times G_0 . The black curve 4) follows the minimum of h_* and respectively of $\log(h_*/\tau)$. The right panel shows a close-up image of the pinch-off region obtained from the left panel, where we omitted the black curve \tilde{V}_g^{min} .

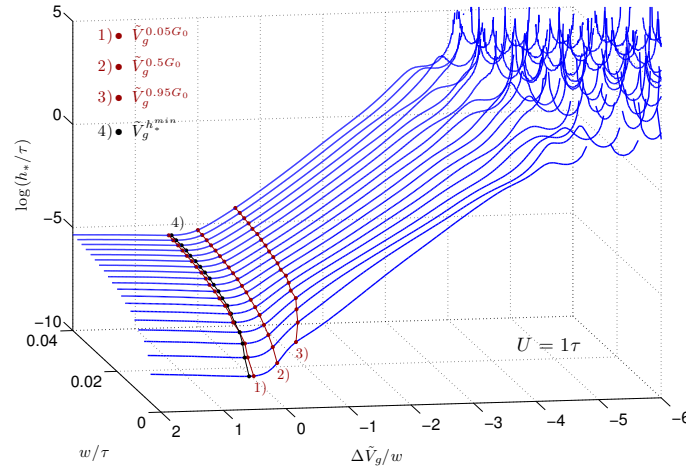


Figure 5.14: Three-dimensional graph of $\log(h_*/\tau)$ as a function of $\Delta\tilde{V}_g/w = (\tilde{V}_g - \tilde{V}_g^{0.5G_0})/w$ and curvature for data generated with the fRG approach including on-site vertex flow. The interaction strength is $U = 1.0\tau$ and w varies from 0.004τ to 0.04τ in increments of 0.002τ . The red curves 1), 2), 3) visualizes the logarithm of h_* for potential heights, where the conductance is 0.005, 0.5, 0.95 times G_0 . The black curve 4) follows the minimum of h_* and respectively of $\log(h_*/\tau)$.

Analysis of $h_*^{0.5G_0}$

In the case of on-site vertex flow, the range of proportionality $f_{0.5G_0} \sim h_*^{0.5G_0}/w$ is larger, in explicit terms $U \lesssim 1.5\tau$. Compare figure 5.17. This indicates the functional dependence

$$h_*^{G_0/2} \sim \alpha \frac{w}{U} \quad \text{with} \quad \alpha \sim 0.13 \quad (5.29)$$

for small interaction strengths. For higher U no quartic behaviour occurs, which is in contrast to the data generated with the other fRG implementation.

Analysis of h_*^{min}

Considering nearest neighbour vertex flow, we derive the same functional dependence of h_{min}^* on the curvature and the interaction, see figure 5.18. Only the parameters are slightly different. We obtain

$$h_*^{min} \sim \alpha w e^{-\beta U} \quad \text{with} \quad \alpha \sim 0.3, \beta \sim 1.1 \quad (5.30)$$

for $U \gtrsim 0.6\tau$. Furthermore, we can extract by fitting a high-ordered polynomial

$$h_*^{min} \sim \frac{4}{\pi} (1 + \alpha U) w \quad \text{with} \quad \alpha = -5.4, \quad (5.31)$$

which is the dominant term for $U < 0.2\tau$. The agreement of this results with the last subsection 5.3.2, especially for higher interaction energies, is surprising. Because the position of h_*^{min} with respect to the pinch-off region strongly differ for the fRG approaches.

Conclusion

Analogously to section 5.3.3, formula 5.25 is valid to describe the absolute dependence of f_2 with the corresponding quantities $h_*^{0.5G_0}(w, U)$ and $f_2(w, U)$ of this subsection. The parameter regime for this formula changes, see bottom left panel of figure 5.16.

Comparing between the resulting quantities of the two different fRG approaches, we studied in the last two subsections, we conclude, the majority of quantities don't change too much in the low interaction regime of U smaller than approximately 1τ . For higher interaction energies there are major changes. For example, the oscillation of f_1 disappear and a linear decrease is observable. Hence, the low energy scale h_* seems to be more sensitive to the absolute value of the nearest neighbour interaction rather than the ration.

5.3.4 Comparison on-site/nearest neighbour vertex flow

In the last two subsections, we analysed the functional dependence of the low energy scale h_* on the interaction strength and the potential curvature for data generated with the two different fRG approach. Within these studies, we revealed some minor differences between

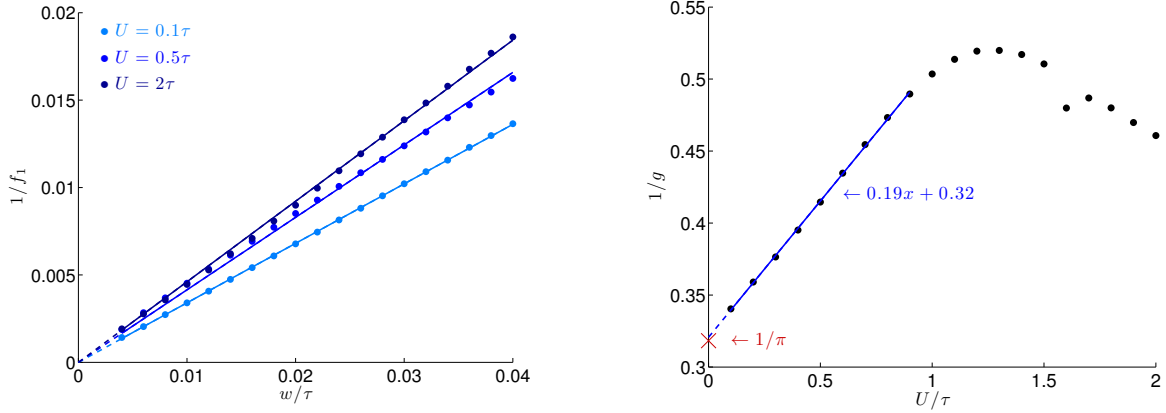


Figure 5.15: Analysis of the exponential growth $\exp(-f_1 \tilde{V}_g)$ for data generated with the fRG approach including on-site vertex flow. Left panel: linearisation of the inverse slope $1/f_1$ with respect to the curvature w , exemplarily illustrated for $U = 0.1, 0.5\tau$ and 2τ . Right panel: the resulting gradients of this linearisation $1/g_1 \sim 1/(f_1 w)$ as a function of the interaction. The blue line represents the linearisation for small U and the red cross corresponds to the theoretical prediction for the non-interacting model, see equation (5.9).

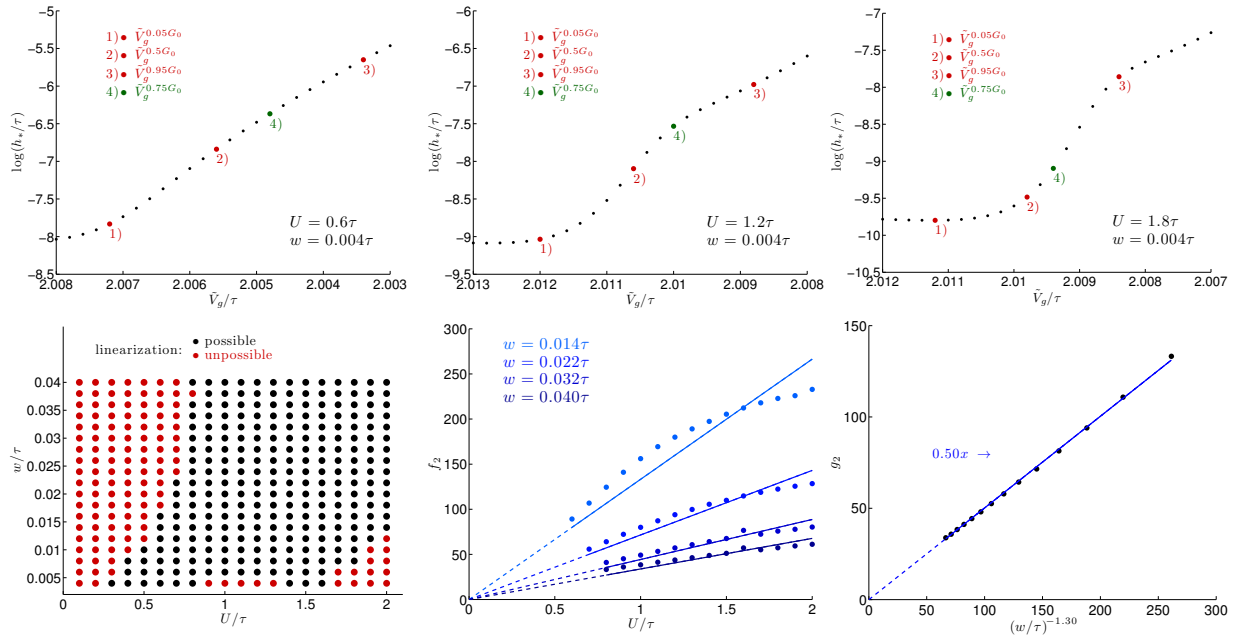


Figure 5.16: Analysis of the exponential growth $\exp(-f_2 V_g)$ for data generated with the fRG approach including on-site vertex flow. Upper panels: the logarithm $\log(h_*/\tau)$ as a function of the potential height for fixed $w = 0.014\tau$ and $U = 0.1, 0.8, 1.6\tau$. The points 1) to 4) represent characteristic values regarding the conductance. Bottom left panel: the black/red dots represent parameters (w, U) for that a linearisation between 2) and 4) is possible/not possible. Bottom middle panel: linearisation of f_2 as a function of U exemplarily for $w = 0.004, 0.012, 0.022\tau$ and 0.04τ . Bottom right panel: linearisation of the resulting gradients $g_2 \sim f_2/U$ with respect to $w^{-1.30}$.

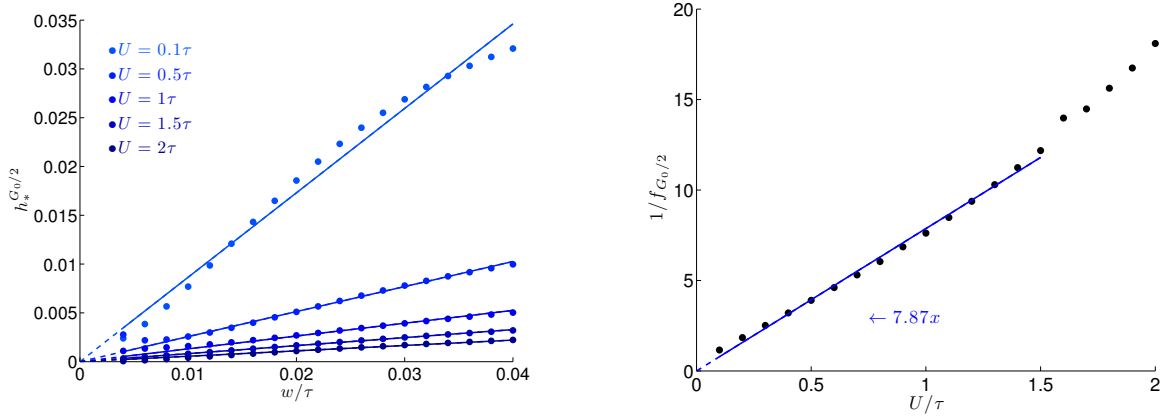


Figure 5.17: Analysis of the absolute value $h_*^{0.5G_0}$ for data generated with the fRG approach including on-site vertex flow. Left panel: linearisation with respect to w , exemplarily illustrated for $U = 0.1, 0.5, 1, 1.5\tau$ and 2τ . Right panel: the inverse of the resulting gradients $f_{0.5G_0} \sim h_*^{0.5G_0}/w$ as a function of U , where the blue line illustrates the linear fitting for $U \leq 1.5\tau$.

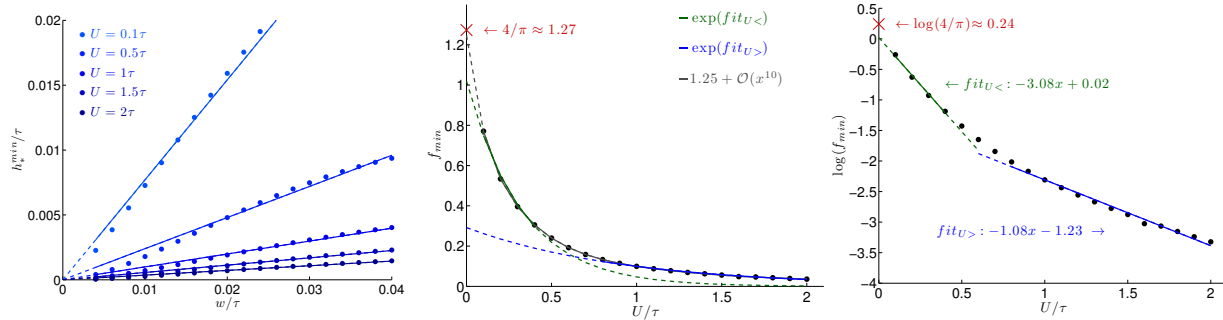


Figure 5.18: Analysis of the minimum h_*^{min} for data generated with the fRG approach including on-site vertex flow. Left panel: linearisation with respect to w exemplarily for $U = 0.1, 0.5, 1, 1.5\tau$ and 2τ . Middle panel: the resulting gradients $f_{min} \sim h_*^{min}/w$ as a function of U . The grey line shows the fitting using a high-ordered polynomial and the green or blue line represent the results for the fittings of $\log(f_{min})$ using $fit_{U<}$ or $fit_{U>}$. Right panel: the logarithm $\log(f_{min})$ versus the interaction strength U , where the green or blue line illustrates the linearisation within a low ($fit_{U<}$) or high ($fit_{U>}$) interaction regime. The red cross corresponds to the theoretical prediction for the non-interacting model, compare equation (5.11).

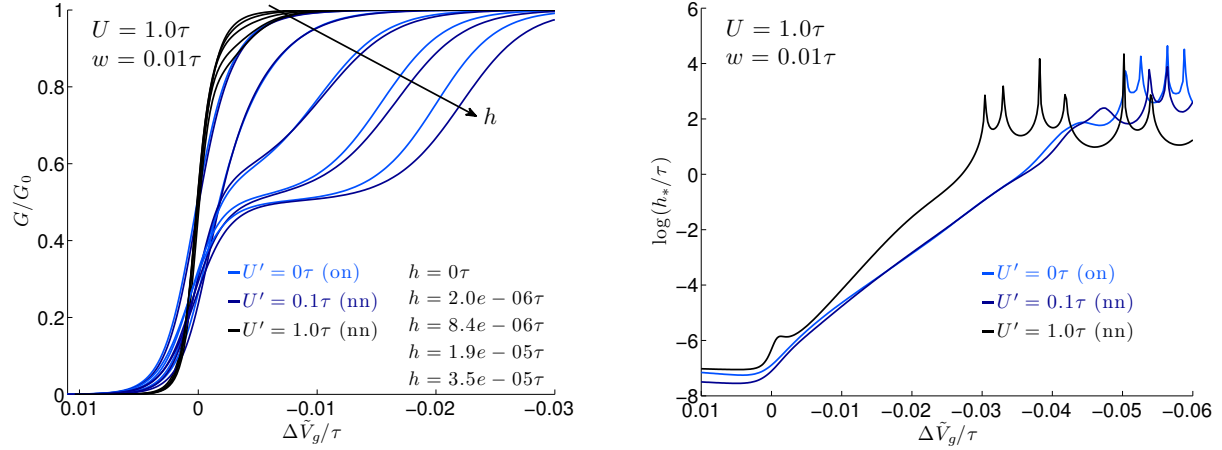


Figure 5.19: Comparison of the conductance and energy scale h_* between data generated with fRG including on-site (on) and nearest neighbour (nn) vertex flow. Left panel: conductance as a function of $\Delta\tilde{V}_g = \tilde{V}_g - \tilde{V}_g^{0.5}G_0$ for various magnetic fields. Right panel: the logarithm $\log(h_*/\tau)$ as a function of $\Delta\tilde{V}_g$. For each panel, data generated with the fRG approach including nearest neighbour, with $U' = U$ (black) and $U' = U/10$ (dark blue), and including on-site (light blue) are visualized. The remaining parameters are $U = 1\tau$ and $w = 0.01\tau$.

these two approaches, which isn't surprising because the nearest-neighbour interaction U' was chosen to be only one-tenth of the on-site interaction energy. Now, we want to have a closer look on the different results emerging from these approaches. Furthermore, we study the influence of the nearest neighbour interaction on the energy scale, conductance by considering elevated values U' .

In the left panel of figure 5.19, we illustrate the conductance resulting from these two approaches, where we set the nearest neighbour interaction $U' = 0.1\tau$ (dark blue) and $U' = 1\tau$ (black) respectively, for the fRG approach including the nearest neighbour vertex flow. Here, we can observe, that the on-site approach (on) produces almost the same low field behaviour of the conductance as the nearest neighbour approach (nn) with $U' = U/10$. Only for Zeeman energies where the spin-resolved plateaus are clearly visible, the conductance of the spin-up transmission mode is considerably reduced in the pinch-off region for the nearest neighbour approach. The similar low field behaviour also reflects in an almost identical energy scale h_* , which can be seen in the right panel of the last-named figure. Within the pinch-off region a slightly smaller value of h_* for the nearest neighbour approach can be found. For higher values of the nearest neighbour interaction, the conductance and hence the scale h_* changes dramatically, see the black curves in figure 5.19. The conductance pinch-off becomes steeper, and the whole influence of the magnetic field is strongly reduced. This includes a fixed position of the pinch-off and only a tiny reduction of the conductance for evaluated Zeeman energies at the beginning of the pinch-off. The graph illustrating the logarithm of h_* shows, that the gradient of the straight line f_2 increases and a plateau-like structure arises in the pinch-off region. In figure 5.20, the evolution of this plateau for increasing nearest neighbour interaction energies is illustrated.

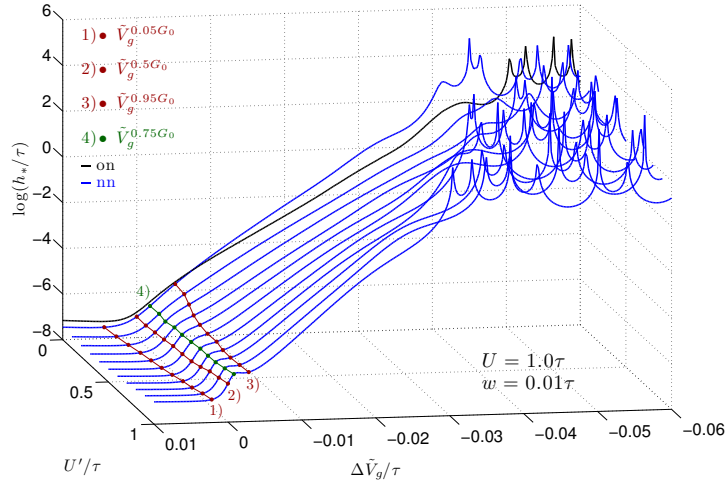


Figure 5.20: Three-dimensional graph of $\log(h_*/\tau)$ as a function of the potential height relative to $\tilde{V}_g^{0.5G_0}$ and the nearest-neighbour interaction U' . The curvature of the potential is $w = 0.01\tau$, the on-site interaction $U = 1.0\tau$ and the nearest-neighbour interaction varies from 0τ to 1.0τ in increments of 0.1τ . The blue/black curves of $\log(h_*/\tau)$ are produce with data generated with the fRG approach including nearest neighbour/on-site vertex flow. The red traces 1), 2), 3), 4) visualizes the logarithm of h_* for potential heights, where the conductance is 0.005, 0.5, 0.95 and 0.75 times G_0 .

Here, we can observe, that the straight line f_2 strictly builds for $U' \neq 0$ within the transition region of the conductance from ~ 0.5 to 0.75 times the conductance quantum and is part and parcel of this plateau-like structure. This plateau seems to be solely induced by the nearest neighbour interaction.

We conclude that the nearest neighbour interaction seems to influence the exponential growth $\exp(-f_2\tilde{V}_g)$ strongly and fixes its appearance between the conductance region of 0.5 to 0.75 times the conductance quantum. In the previous analysis in 5.3.2 and 5.3.3, we saw that this influence is already recognizable for $U' = U/10$ and seems to hold for arbitrary interaction energies.

5.4 Two-dimensional system

In this subsection, we use the fRG approach of section 3.3.1 to extend the previous studies of the influence of interaction on the zero temperature linear conductance of one-dimensional systems towards two-dimensional systems. In this fRG implementation, we consider only on-site interaction. Besides the transmission of the first submode, this extension enables us to investigate the transmission of additional modes with higher energies. They are of interest, because higher conductance plateaus reveal quite a different behaviour with respect to several conductance anomalies in experiments, like the zero field splitting, temperature dependence, magnetic field dependence and effective g-factor, see section 4.4.2. Our hope is not only to find a reason of these deviations, but in fact to get useful hints of the physical

$w_y = 0.0\tau$						
E_α/τ	-3.80	-3.25	-2.45	-1.55	-0.75	-0.2
$ \Psi_\alpha^2 ^2$	0.21	0.21	0.21	0.21	0.21	0.21

$w_y = 0.5\tau$						
E_α/τ	-3.71	-3.04	-2.21	-1.32	-0.53	-0.09
$ \Psi_\alpha^2 ^2$	0.24	0.22	0.19	0.23	0.22	0.19

$w_y = 1.0\tau$						
E_α/τ	-3.51	-2.54	-1.58	-0.71	0.28	0.44
$ \Psi_\alpha^2 ^2$	0.30	0.23	0.18	0.24	0.26	0.19

Table 5.1: Eigenenergies in terms of our energy scale (energy offset -2τ) and the scalar product of the component-wise squared eigenstates of the transversal confinement potential (5.2) at the center of the potential barrier for $w_y = 0.0, 0.5$ and 1.0τ .

background of the conductance anomalies. Of course, we won't be able to reproduce any zero field splitting or temperature dependence in our static fRG approach and, hence, we will concentrate on the anomalous magnetic field behaviour and the effective g-factor.

Since we use a two-dimensional system with finite width $M > 1$, we are forced to extend our considered interaction regime to much higher values to obtain a conductance behaviour comparable to one-dimensional systems that we investigated up to now. This can be understood as follows. By increasing the width, the averaged probability of presence for an electron localized at a certain site becomes smaller and hence the interaction between two electrons propagating through the constriction decreases. Since we consider interaction energies of order of ten times τ , the question arises, whether fRG still provides reliable results or not, because in this regime we are clearly no longer able to argue with a small interaction strength. If the results are comparable to the one-dimensional case, there is no reason for us to be suspicious. However, we can't exclude that the fRG approximations strongly bias the results within this interaction regime. Therefore, further studies of the validity of the truncation approach are required. At any rate, we should apply our fRG method to a reference system, for example a quantum dot implemented within a 2D model, and compare the obtained results with well-known results of the system.

In the following, we use a quasi-one-dimensional system consisting of six sites in transversal and 500 sites in longitudinal direction. For this system, we study three different transversal confinements, a hard-wall potential ($w_y = 0\tau$) and a harmonic-like potential of the form (5.2), with two different curvatures $w_y = 0.5\tau$ and $w_y = 1.0\tau$. In table 5.1, we stated the corresponding eigenenergies E_α and scalar products of the component-wise squared eigenstates. Since we are considering an on-site density-density interaction, the quantity $|\Psi_\alpha^2|^2$ is the conversion factor of U for mapping the transversal eigenstate α onto an effective one-dimensional system. Therefore, table 5.1 indicates, that we require roughly five times higher interaction strengths for the 2D model compared to the 1D model

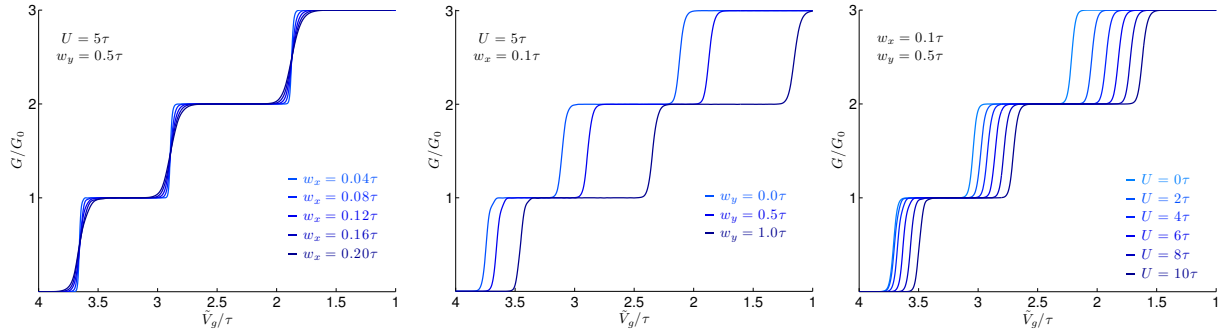


Figure 5.21: Influence of the potential curvatures and interaction strength on the first three conductance steps. In all panels the conductance is plotted as a function of the potential height, where one parameter is varied and the others are fixed with values $w_x = 0.1\tau$, $w_y = 0.5\tau$ and $U = 5\tau$. In the left or middle panel the longitudinal or transversal curvature is varied and in the right panel the interaction energy changes.

to obtain comparable interactions between the modes.

The eigenenergies of the transversal confinement potential at the center of the barrier determine the position of the pinch-off. Therefore, the energies of the latter table are equivalent up to sign to the pinch-off values in the non-interacting case. In the case of a hard-wall potential $w_y = 0\tau$, the values in 5.1 are in agreement with equation (3.60).

Before we study the magnetic field behaviour of the conductance, we discuss the influence of the interaction and curvatures on the zero-field conductance steps. These effects are summarized in figure 5.21. As we already stated, the curvature w_x determines the width of the transition from one plateau to another which is also valid in a 2D interacting model, see left panel of figure 5.21. The transversal curvature w_y determines the position of the pinch-off. Since we are dealing with a pseudo-harmonic confinement, the energy splitting of the submodes is not equidistant w_y and varies for every plateau. With increasing transversal curvatures, the eigenenergies of the transversal modes increase and the pinch-off values shift to smaller values of \tilde{V}_g , compare middle panel of figure 5.21. Increasing interaction values enhance the electron repulsion at the center of the potential barrier and leads to a suppression of the conductance. This induces a shift of the pinch-off which becomes larger for higher submodes, due to an increased electron density at the center of the barrier, as can be seen in right panel of figure 5.21.

We shall now continue with the magnetic field behaviour of the conductance plateaus. In the following, we focus on the first three plateaus. The other conductance steps are not observable for all transversal confinements and interaction energies, we are considering.

In figure 5.22, we visualized the conductance and the corresponding differential conductance $dG/d\tilde{V}_g$ as a function of \tilde{V}_g . The differential conductance evolution of the first submode reveal numerical problems. This is connected with the choice of the curvatures and the interaction. The longitudinal curvature w_x is very high and, hence, the potential rather angular. Although, we wanted to present this data because of its similarities to the experimental measurements. For smaller value of w_x the slope of the pinch-off

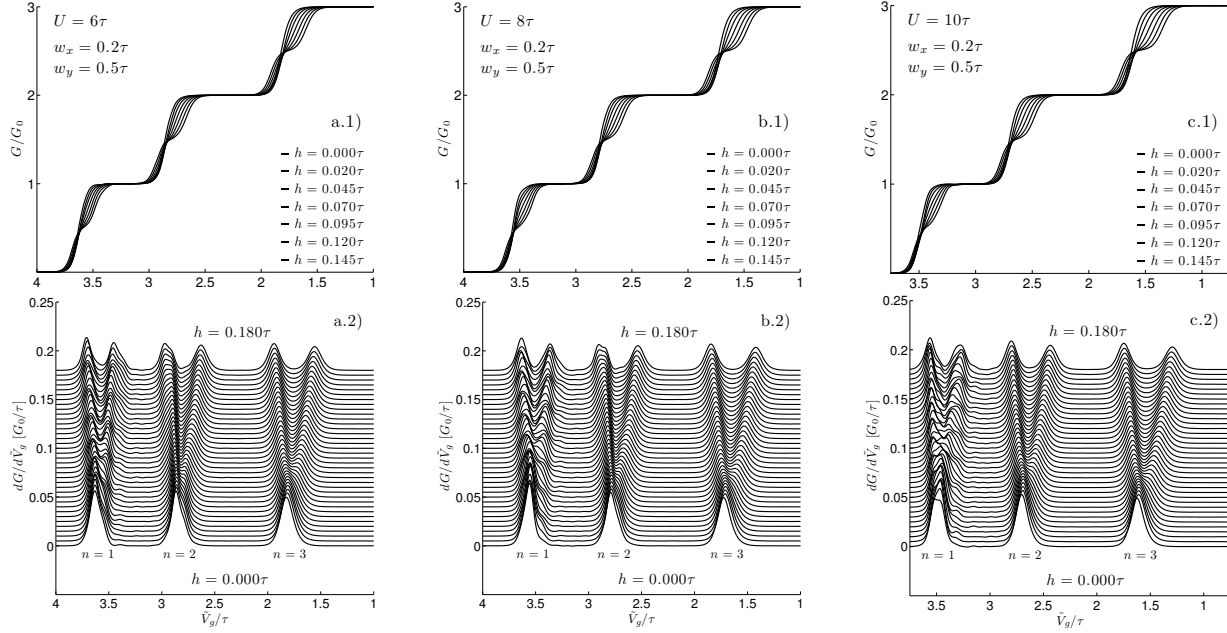


Figure 5.22: Influence of the interaction on the conductance and differential conductance $dG/d\tilde{V}_g$ for the first three conductance plateaus. Upper panel: conductance as a function of the potential height for magnetic fields, including $h = 0\tau$, ranging from $h = 0.2\tau$ to $h = 0.145\tau$ in increments of 0.25τ . Bottom panels: differential conductance as a function of potential height ranging from $h = 0\tau$ to $h = 0.18\tau$ in increments of 0.005τ . The traces are shifted for a better overview. The interaction changes from the panels a) to c), where $U = 6, 8, 10\tau$. The curvature parameters $w_x = 0.2\tau$ and $w_y = 0.5\tau$ are fixed. Notice the difference of magnetic field interval within the upper and bottom panels.

becomes much steeper. Despite these numerical issues, we can observe the fundamental differences within the first three conduction steps. At first, the qualitative dependence of the conductance on the magnetic field is the same for every submode. The conductance evolves from above towards the spin-resolved plateaus and the spin-up pinch-off is almost constant. This holds only within limits. The effective g -factor g^* , characterizing the Zeeman splitting of the spin-up and spin-down modes³, is considerably increasing with the conductance plateaus. Furthermore, the spin-up pinch-off moves to larger \tilde{V}_g values for higher conductance plateaus and elevated magnetic fields. Whether, this is caused by the increasing g -factor or might be interpreted as, a reduction of the anomalous magnetic field behaviour, can't be read off this figure. A comparison of the conductance traces with equivalent Zeeman splittings could provide clarity.

We already mentioned the differences of the g -factor with respect to the different submodes. In the following, we want to analyse this quantity in more details. In figure 5.23, we visualized the effective g -factors for three different transversal confinements each for the

³For a detailed introduction and experimental results of the effective g -factor, we refer to the subsection 4.4.2.

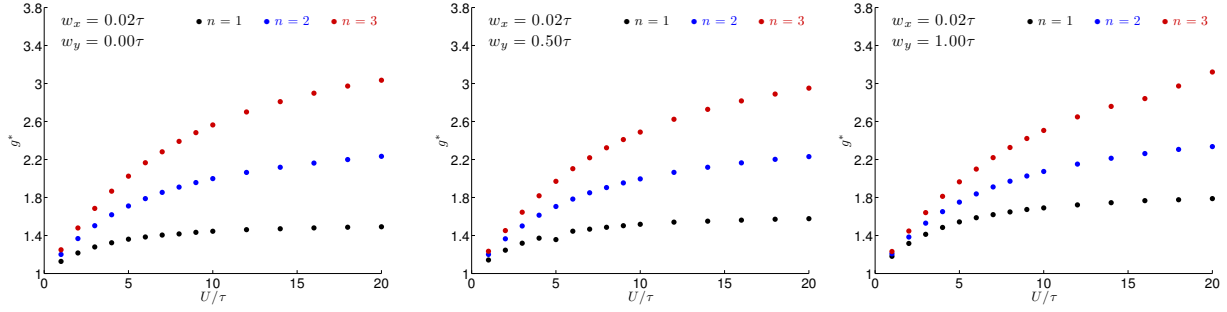


Figure 5.23: Effective g -factor for the first three submodes as a function of the interaction U and three different transversal confinements. In the left, middle, right panel is the transversal curvature $w_y = 0, 0.5\tau$ and 1.0τ . The longitudinal curvature is for each panel fixed $w_x = 0.02\tau$.

first three submodes. The g -factor g^* starts to increase linearly from the number one and seems to saturate for very high interaction strengths between 1 and 3.4. The enhancement of the g -factor is in agreement with experiments of Koop et al. [25]. The linear behaviour for small interaction values was already observed in one-dimensional models by Bauer and Heyder [3, 17]. We can also observe, that the effective g -factor g^* strongly increases for higher submodes where its difference becomes almost equidistant for higher U . This is contrary to the publication [25] of Kopp et al. and the references in it, compare section 4.4.2. They predict a decreasing effective g -factor for increasing subband index. But, the observed increasement of g^* in our model for higher submodes seems not to be related with the transversal confinement. Because, if the confinement strengthens by increasing w_y , then the g -factor slightly increases for all submodes, as expected. At this point, we can't explain this contrary behaviour and further investigations are necessary.

In the following, we compare directly the magnetic field behaviour of the first three conductance steps. Therefore, we illustrated $G_{nn} = G_0 \mathcal{T}_{nn}$ (\mathcal{T}_{nn} is the transmission probability of the n th transmission mode) of the first three conductance steps for different Zeeman energies. See figure 5.24. Here, the conductance is plotted as a function of

$$\Delta \tilde{V}_g^{(n)} = \tilde{V}_g - \tilde{V}_g^{(n+0.5)G_0} \quad (5.32)$$

which is the distance from \tilde{V}_g to the potential height where $\mathcal{T}_{nn} = 1/2$. We can observe, that the magnetic field dependence is qualitatively the same. The conductance step evolves from above into the spin-resolved conductance plateaus where the position of the spin-up pinch-off hardly changes. For increasing submode index, the conductance trace seems to be more sensitive to the magnetic field which corresponds to a higher effective g -factor. For transversal curvature $w_y = 1\tau$, the zero-field conductance pinch-off becomes flatter for increasing submode index. But, it is questionable, whether this is caused by the elevated transversal confinement. The comparison between the evolution of zero-field conductance pinch-off gradients for the panels b), c), h), k) with c), f), i) l) reveals a different behaviour with respect to the pinch-off gradient. Therefore, we assume, the strongly changing slope is most likely induced by the changing form of the potential. A more precise analysis is difficult using this illustration because of the changing gradients of the conductance traces.

In figure 5.25, we plotted the same conductance traces as we did in figure 5.24, but now we rescaled the x-axis by the width $W_{po}^{(n)}$ of the nth submode pinch-off region which is defined by

$$W_{po}^{(n)} := \tilde{V}_g^{0.05G_0} - \tilde{V}_g^{0.95G_0}. \quad (5.33)$$

This approach fixes the zero field conductance slope of every submode and excludes the effect, that every transmission mode feels another effective potential curvature due to the repulsive interaction with other modes. Therefore, the zero field conductance traces have the same form and only small deviations are noticeable. For stronger transversal confinements, the spin-down conductance become less suppressed for all submodes. And this decreasing of the conductance suppression is stronger for higher submodes, as can be seen for example in the panels g), h) and i). For the first mode is almost no change noticeable. So that for $w_y = 1\tau$, the magnetic field behaviour for all submodes is almost the same and almost identical to the conductance behaviour of the first mode. And this evolution to an overall combined magnetic field behaviour of all submodes takes place for all investigated interaction energies and is only slightly sensitive with respect to the interaction. Even though, we vary the interaction about 12τ . This can be seen by the panel c), f), i) and l). Therefore, the first submode also seems to be distinguished in our model. For the confirmation of the generic nature of this phenomena and an explanation, further research is necessary.

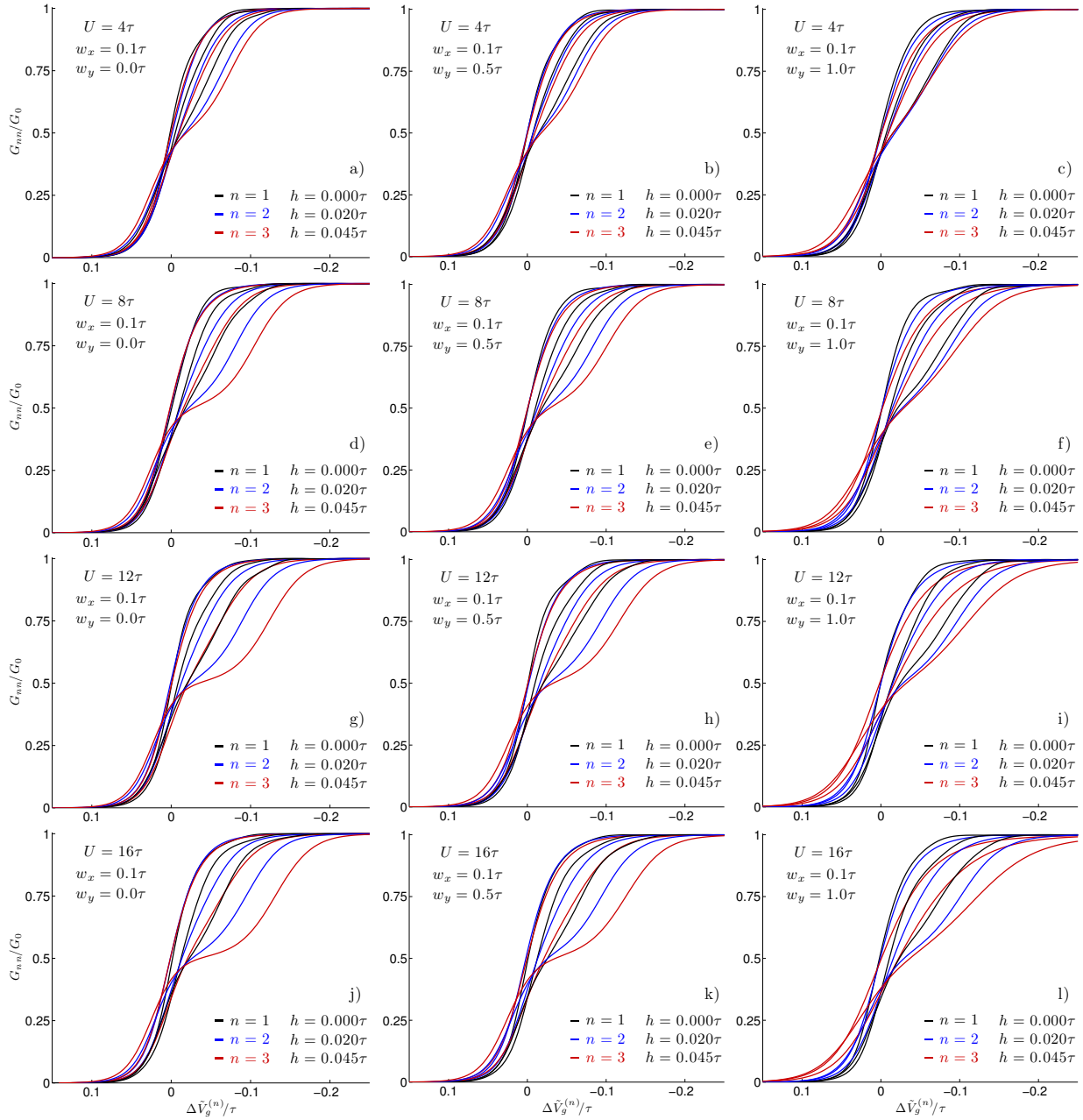


Figure 5.24: Comparison of the magnetic field behaviour of the conductance for the first three conductance plateaus. The conductance G_{nn} of each transmission mode is illustrated as a function of the potential height measured relatively to \tilde{V}_g where G_{nn} is one-half of the conductance quantum. The transversal potential curvature w_y is increased from the left to the right panels, where $w_y = 0.0, 0.5, 1.0\tau$, and the interaction strength is increased from the top to the bottom panels, where $U = 4, 8, 12, 16\tau$. The longitudinal curvature w_x is always fixed at 0.5τ . With increasing Zeeman energy the spin-resolved plateaus develops for each mode.

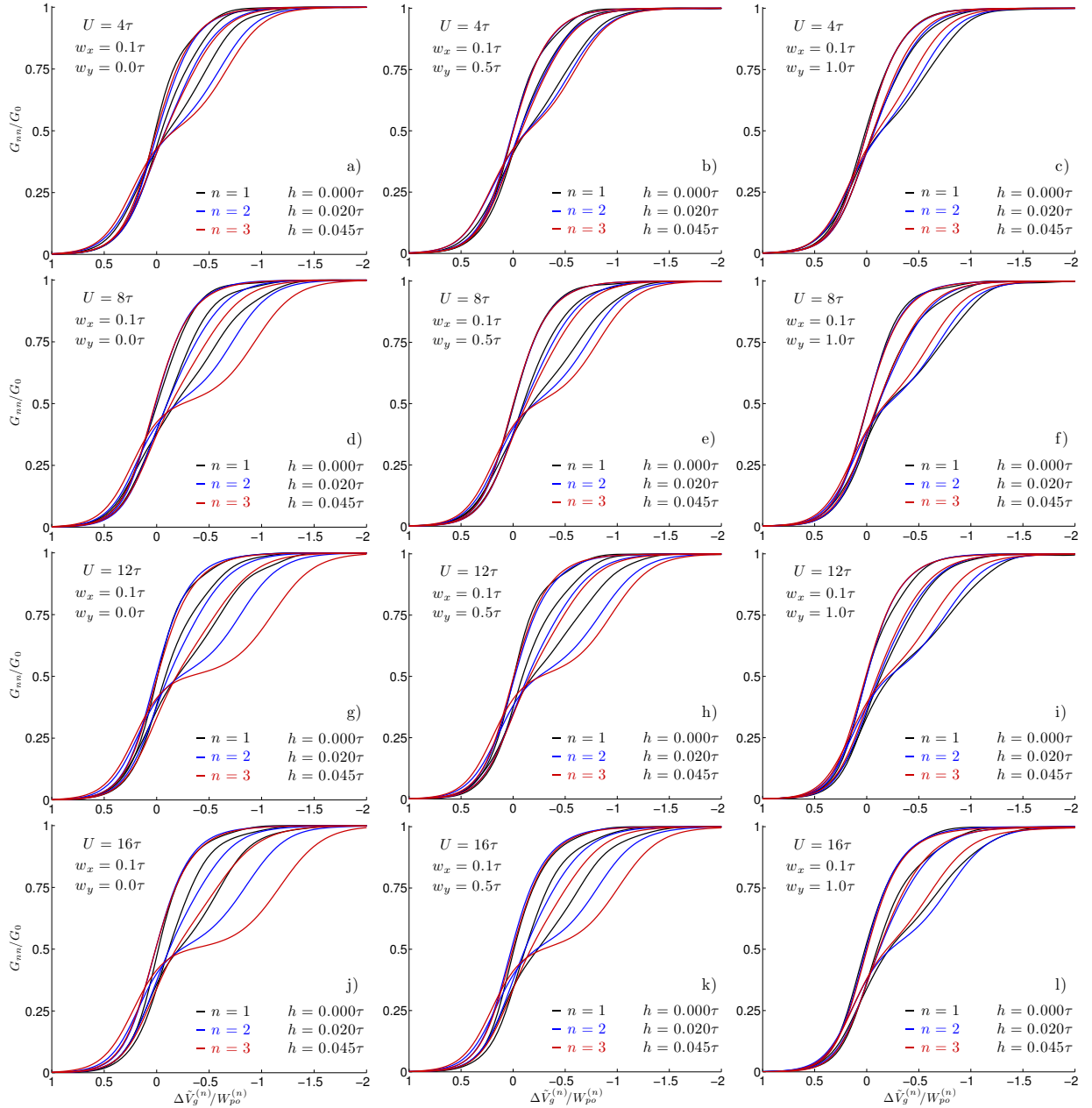


Figure 5.25: Comparison of the magnetic field behaviour of the conductance for the first three conductance plateaus where the pinch-off region is rescaled for each mode. The conductance G_{nn} of each transmission mode is illustrated as a function of $\Delta\tilde{V}_g^{(n)}/W_{po}^{(n)}$ the potential height measured relatively to \tilde{V}_g where G_{nn} is half the conductance quantum. The potential curvature w_y is increased from the left to the right panels, $w_y = 0.0, 0.5, 1.0\tau$, and the interaction strength from the top to the bottom panels, $U = 4, 8, 12, 16\tau$, where w_x is always fixed at 0.5τ . With increasing Zeeman energy the spin-resolved plateaus develops for each mode.

Chapter 6

Conclusion and outlook

In quantum point contacts occurs besides the well-known conductance quantization additional unexpected conductance anomalies. This includes an anomalous magnetic field behaviour which is assumed to be persistent in the limit of vanishing temperature. Florian Bauer successfully managed to set up a static fRG approach to study zero temperature linear conductance in an one-dimensional extended interaction region, with a potential barrier modelling the QPC. This approach was able to reveal the anomalous magnetic field dependence. The main purpose of this thesis was to extend this successful method to two-dimensional systems, and thereby to study higher conductance steps.

For this purpose, we introduced fRG in chapter 2. We sketched the derivation of the fRG flow equations which are a hierarchy of infinitely many coupled differential equations in the vertex functions and describe the flow from a static to the fully interacting system. To solve this hierarchy, we introduced a perturbative truncation by neglecting all vertex functions, that are high-ordered in the interaction. In addition, we considered only the static case by restricting ourselves to zero Matsubara frequency. Due, to this static approximation, we were only able to calculate $T = 0K$ observables. Solving the resulting flow equations leads to an effective non-interacting model which takes the interaction into account.

In chapter 3, we applied this static renormalization group enhanced perturbative method to a 2D Hubbard model. To be able to deal with a translational non-invariant system with a vast extension, we considered only the on-site vertex flow and set almost all elements of the remaining vertex functions to zero. To solve the resulting differential equations and to compute the required Green functions, we introduced the RGF algorithm which calculates elements of a sparse inverse matrix.

In chapter 4, we gave background knowledge for quantum point contacts. We discussed several experimental researches in this field and peculiarities of higher spin-degenerated subbands. Furthermore, we introduced the microscopic models of Meir et al. and Lunde et al.

In chapter 5, we used the derived fRG approach to study zero temperature linear conductance in our Hubbard model, where a saddle point potential models the QPC.

Before we studied two dimensional systems, we performed a minute analysis of the low energy scale h_* for two different fRG approaches (including nearest neighbour vertex flow,

with $U' = U/10$, and on-site vertex flow) in an one-dimensional system. We could show, that the exponential growth, corresponding to f_1 , is already existent in the non-interaction system and smoothly evolves to the corresponding structure of the interacting system. By this transition, the gradient f_1 changes only slightly. For many parameters w , U , this exponential dependence occurs only in a regime where the transmission is one. We conclude, f_1 seems to be an artefact of the non-interacting system rather than a characteristic feature of the anomalous magnetic field behaviour in the interacting system. This slope also depends on the specific values of the on-site interaction and nearest neighbour interaction. The second exponential growth, corresponding to f_2 , seems to be related with the nearest-neighbour interaction. Since, the nearest-neighbour interaction seems to fix the appearance of f_2 between $\tilde{V}_g^{0.75G_0}$ and $\tilde{V}_g^{0.5G_0}$. Furthermore, it is questionable, how precise the low energy scale h_* can characterise the anomalous magnetic field behaviour. Because, it is only defined within a magnetic field area where the whole pinch-off only shifts to smaller \tilde{V}_g .

Besides the analysis of h_* , we managed to state first results for the magnetic field behaviour of higher conductance steps. The magnetic field behaviour depends on the transversal confinement and differs for every submode. In contrast to experiments, the effective g-factor increases with the submode index. But for increasing transversal confinements, the effective g-factor gains. Therefore, this increasing effective g-factor must be caused by another process. The use of different potentials could give more insight into this behaviour. Furthermore, we found an indication, that the first conductance plateau is also distinguished in our model. For a high transversal confinements, the magnetic field behaviour of the higher submodes become equivalent to the first one. Here, the conductance was scaled with the width of the pinch-off region. To confirm this phenomena, the investigation of different transversal confinements and potentials are necessary.

The data seems to be strongly dependent on the specific form of the potential and not only on the parameters w_x and w_y . Therefore, we suggest to include the transversal confinement into the leads. Thereby, a specific implementation of the crossover from the harmonic-like potential of the constriction to the hard-wall potential of the leads is no longer necessary. The transversal confinement becomes decoupled of the x -direction and an isolated investigation of the dependence of the conductance on the submode energysplitting becomes possible. To identify a "weakening" of the anomalous magnetic field behaviour in our presented data is hardly possible. It's not clear, whether the differences of the conductance traces are induced by differing g -factors or not. Furthermore, it's not clear, how the enhanced g -factor and the anomalous evolution of the conductance for increasing magnetic fields are correlated. For trying to separate these two phenomena, we suggest to investigate the position and form of the spin-resolved conductance plateaus for fixed spin-splitting energies.

We are dealing for two-dimensional models with huge interaction energies. It is questionable whether the perturbative fRG truncation still provides reliable results or not. Therefore, further studies are necessary to check its validity. We propose a comparison with results of a well-known reference system, for example a quantum dot.

A further possibility of application within the field of QPCs is the investigation of the intersection of two spin-split subbands of two neighbouring spin-degenerate subbands. Graham et al. performed such QPC measurement and reported an additional "0.7 anomaly"-like structure. Therefore, the question arises if our model shows an anomalous conductance behaviour within such an intersection region.

Appendix A

Calculation details to the projected Green functions

In the following we want to proof the equations (3.25) and (3.26) from section 3.2.3, which express the projected Green functions G_{PQ} and G_Q in terms of G_P . The Green function G_P was already calculated in the mentioned section using the projection method and the surface Green function of the leads. Our starting point is the matrix equation (3.19), that includes

$$(zP - H_P)\mathcal{G}_{PQ}(z) - H_{PQ}\mathcal{G}_Q(z) = 0, \quad (\text{A.1})$$

and

$$-H_{QP}\mathcal{G}_{PQ}(z) + (zQ - H_Q)\mathcal{G}_Q(z) = \mathbb{1}. \quad (\text{A.2})$$

Details to the calculation of \mathbf{G}_{PQ}

We multiply equation (A.1) from left by $(zQ - H_Q)$

$$(zP - H_P)\mathcal{G}_{PQ}(z)(zQ - H_Q) - H_{PQ}\mathcal{G}_Q(z)(zQ - H_Q) = 0, \quad (\text{A.3})$$

and add the zero matrix $0 = H_{PQ} - H_{PQ}$

$$(zP - H_P)\mathcal{G}_{PQ}(z)(zQ - H_Q) - H_{PQ} + H_{PQ} - H_{PQ}\mathcal{G}_Q(z)(zQ - H_Q) = 0. \quad (\text{A.4})$$

Now we can rearrange the second part of the latter equation in the following way

$$\begin{aligned} H_{PQ} - H_{PQ}\mathcal{G}_Q(z)(zQ - H_Q) &= H_{PQ}(1 - \mathcal{G}_Q(z)(zQ - H_Q)) \\ &= H_{PQ}(zQ - H_Q)^{-1}(1 - (zQ - H_Q)\mathcal{G}_Q(z))(zQ - H_Q) \\ &= -H_{PQ}(zQ - H_Q)^{-1}H_{QP}\mathcal{G}_{PQ}(z)(zQ - H_Q), \end{aligned} \quad (\text{A.5})$$

where we used equation (A.2)

$$\mathbb{1} - (zQ - H_Q)\mathcal{G}_Q(z) = -H_{QP}\mathcal{G}_{PQ}(z). \quad (\text{A.6})$$

Therefore, equation (A.4) becomes

$$(zP - H_P)\mathcal{G}_{PQ}(z)(zQ - H_Q) - H_{PQ} - H_{PQ}(zQ - H_Q)^{-1}H_{QP}\mathcal{G}_{PQ}(z)(zQ - H_Q) = 0. \quad (\text{A.7})$$

Now we can exclude $\mathcal{G}_{PQ}(zQ - H_Q)$

$$((zP - H_P) - H_{PQ}(zQ - H_Q)^{-1}H_{QP})\mathcal{G}_{PQ}(zQ - H_Q) = H_{PQ}, \quad (\text{A.8})$$

and using the result of \mathcal{G}_P from section 3.23, we finally obtain

$$\mathcal{G}_{PQ}(z) = \mathcal{G}_P(z)H_{PQ}(zQ - H_Q)^{-1}, \quad (\text{A.9})$$

which we wanted to proof.

Details to the calculation of \mathbf{G}_Q

To show that equation (3.26) holds, we just have to multiply the latter expression for \mathcal{G}_{PQ} from left by H_{QP} , that provides

$$H_{QP}\mathcal{G}_{PQ}(z) - H_{QP}\mathcal{G}_P(z)H_{PQ}(zQ - H_Q)^{-1} = 0. \quad (\text{A.10})$$

Now we add the unit matrix on both sides and use (A.2)

$$(zQ - H_Q)\mathcal{G}_Q(z) - H_{QP}\mathcal{G}_P(z)H_{PQ}(zQ - H_Q)^{-1} = \mathbb{1}, \quad (\text{A.11})$$

which is equivalent to

$$\mathcal{G}_Q(z) = (zQ - H_Q)^{-1} + (zQ - H_Q)^{-1}H_{QP}\mathcal{G}_P(z)H_{PQ}(zQ - H_Q)^{-1}, \quad (\text{A.12})$$

the expression we wanted to proof.

Appendix B

Calculation details to the surface Green function \tilde{g}

In the following section we want to proof that for $\text{Im}\{\chi\} \neq 0$ the inequalities $|v_1| < 1$ and $|v_2| > 1$ hold, and only v_1 is enclosed by the unit circle \mathcal{S}_1 in the contour integral (3.37). In addition, we want to proof that the widely used form (3.41), here (B.1),

$$\tilde{g}(z) = \begin{cases} \frac{1}{\tau} \left(\chi - i\sqrt{1 - \chi^2} \right) & \text{if } \text{Im}\{\chi\} > 0 \\ \frac{1}{\tau} \left(\chi + i\sqrt{1 - \chi^2} \right) & \text{if } \text{Im}\{\chi\} < 0 \end{cases}, \quad (\text{B.1})$$

where $\sqrt{}$ denotes the positive square root, is equivalent to equation (3.39), here (B.2),

$$\tilde{g}(z) = \frac{1}{\tau} \left(\chi - \sqrt{\chi^2 - 1} \right), \quad (\text{B.2})$$

where $\text{Im}\{\chi\} \neq 0$ and the sign of the square root is chosen so that the sign of $\sqrt{\chi^2 - 1}$ is equivalent to the sign of $\text{Im}\{\chi\}$. For these proofs we use the cartesian representation of the two possible square roots w_{\pm} of $z = x + iy$, where $x, y \in \mathbb{R}$ and $y \neq 0$, [50, ch. 1.2.3 equ. 9]

$$w_{\pm} = \pm \left(\sqrt{1/2(x + |z|)} + i \frac{y}{|y|} \sqrt{1/2(-x + |z|)} \right) \quad (\text{B.3})$$

and especially

$$\sqrt{z} = -i \frac{y}{|y|} \sqrt{-z}. \quad (\text{B.4})$$

Unit circle \mathcal{S}_1 encloses only the pole v_1

In this subsection $\sqrt{}$ always denotes the positive square root. We define the quantities $x_1, x_2, s_1, s_2 \in \mathbb{R}$ by

$$\chi =: x_1 + ix_2 \quad \text{and} \quad \sqrt{\chi^2 - 1} =: s_1 + is_2. \quad (\text{B.5})$$

Under the assumption of $\text{Im}\{z\} = x_2 \neq 0$, we want to show that $|v_1| < 1 < |v_2|$ and that this is equivalent to $|v_1| < |v_2|$ because of $v_1 \cdot v_2 = 1$. Now we can use

$$\text{Im} \left\{ \sqrt{\chi^2 - 1} \right\} = 2 \text{Re}\{\chi\} \text{Im}\{\chi\}, \quad (\text{B.6})$$

which is equivalent to $s_2 = 2x_1x_2$, and equation (B.3) to rewrite $v_{1/2}$ into the following form

$$v_1 = \chi - \left(\frac{x_1}{|x_1|} \sqrt{1/2(s_1 + |\chi|)} + i \frac{x_2}{|x_2|} \sqrt{1/2(-s_1 + |\chi|)} \right) \quad (\text{B.7})$$

$$v_2 = \chi + \left(\frac{x_1}{|x_1|} \sqrt{1/2(s_1 + |\chi|)} + i \frac{x_2}{|x_2|} \sqrt{1/2(-s_1 + |\chi|)} \right) \quad (\text{B.8})$$

and obtain

$$\begin{aligned} |v_1|^2 &= \left(|x_1| - \sqrt{1/2(s_1 + |\chi|)} \right)^2 + \left(|x_2| - \sqrt{1/2(-s_1 + |\chi|)} \right)^2 \\ &< \left(|x_1| + \sqrt{1/2(s_1 + |\chi|)} \right)^2 + \left(|x_2| + \sqrt{1/2(-s_1 + |\chi|)} \right)^2 = |v_2|^2, \end{aligned} \quad (\text{B.9})$$

where the strict lesser sign holds because $\text{Im}\{\chi\} = x_2 \neq 0$ and hence $\chi \neq 0$. And this proves the claim.

Equality between $\tilde{\mathbf{g}}$ and $\tilde{\tilde{\mathbf{g}}}$

In this subsection $\sqrt{\quad}$ always denotes the positive square root. We define the quantities $x_1, x_2, s_1, s_2 \in \mathbb{R}$ by

$$\chi =: x_1 + ix_2 \quad \text{and} \quad \sqrt{\chi^2 - 1} =: s_1 + is_2. \quad (\text{B.10})$$

Under the assumption of $\text{Im}\{z\} = x_2 \neq 0$, we can rewrite $\tilde{\tilde{\mathbf{g}}}$ the following way

$$\tau \tilde{\tilde{\mathbf{g}}}(z) = \chi - i \frac{x_2}{|x_2|} \sqrt{1 - \chi^2}. \quad (\text{B.11})$$

And using equations (B.3), (B.4) and $s_2 = 2x_1x_2$, we obtain

$$\begin{aligned} \tau \tilde{\tilde{\mathbf{g}}}(z) &= \chi - i \frac{x_2}{|x_2|} \sqrt{1 - \chi^2} = \chi - i \frac{x_2}{|x_2|} \left(-i \frac{s_2}{|s_2|} \right) \sqrt{\chi^2 - 1} \\ &= \chi - \left(\frac{x_1}{|x_1|} \sqrt{1/2(s_1 + |\chi|)} + i \frac{x_2}{|x_2|} \sqrt{1/2(-s_1 + |\chi|)} \right) \\ &= \tau \tilde{\mathbf{g}}(z), \end{aligned} \quad (\text{B.12})$$

what we wanted to prove.

Appendix C

Calculation details to the spectral function of a 2D tight-binding chain

In section 3.2.4 we calculated the spectral function \mathcal{A}^{1D} of an one-dimensional infinite translational invariant tight-binding chain using the surface Green function of an one-dimensional semi-infinite lead (3.43). With this result the spectral function of the two-dimensional infinite tight-binding chain is easily attainable by a basis transformation to the transversal eigenfunction.

We assume a finite effective width M and use the following abbreviation for the transversal eigenstates (3.35)

$$s_\beta(m) := \psi_{k_\beta}(m) = \sqrt{\frac{2}{M+1}} \sin\left(m \frac{\beta\pi}{M+1}\right), \quad (\text{C.1})$$

with

$$m \in \{0, \dots, M+1\} \quad \text{and} \quad \beta \in \{1, \dots, M\}. \quad (\text{C.2})$$

But in the following, we restrict ourselves to $m \in \{1, \dots, M\}$ and therefore the indices m and β commute

$$s_\beta(m) = s_m(\beta). \quad (\text{C.3})$$

The eigenfunctions $\{s_\beta | \beta \in \{1, \dots, M\}\}$ are an orthonormal basis and we can define the orthogonal matrix ¹

$$U_{i,j} := s_j(i) \quad \text{with} \quad [U^T]_{i,j} = s_i(j) = U_{i,j}. \quad (\text{C.4})$$

With this basis transformation we can easily perform the inversion of (3.57)

$$G^{2D,ret}(w) = \frac{1}{(w + i0^+) \mathbb{1} - H^{stripe} - \Sigma_{leads}^{2D}(w + i0^+)} \quad (\text{C.5})$$

¹If you explicitly want to revise the orthogonality, relation (C.3) is very useful.

112 C. Calculation details to the spectral function of a 2D tight-binding chain

because the matrices H^{stripe} and Σ_{leads}^{2D} become diagonal, especially

$$g_{1,m;1,m'}^{ret}(w) = \sum_{l=1}^M U_{m,l} g_{l,l}(w) [U^T]_{l,m'} \quad \text{with} \quad g_{l,l}(w) = \tilde{g}^{ret}(w + 2\tau_y \cos(k_l)) \quad (\text{C.6})$$

holds. Therefore, the Green function becomes

$$G_{i,j}^{2D,ret}(w) = \sum_{l=1}^M U_{i,l} \frac{1}{w + i0^+ + \mu + 2\tau_y \cos(k_l) - \Sigma_{leads}^{1D}(w + 2\tau_y \cos(k_l))} [U^T]_{l,j} \quad (\text{C.7})$$

and the spectral function

$$\mathcal{A}_{i,j}^{2D}(w) = [-2 \text{Im}\{G_{i,j}^{2D,ret}(w)\}]_{i,j} = \sum_{l=1}^M U_{i,l} \mathcal{A}^{1D}(w + 2\tau_y \cos(k_l)) [U^T]_{l,j}, \quad (\text{C.8})$$

which is equivalent to equation (3.58).

Appendix D

Recursive Green function algorithm

In the proceeding text we want to show how the forward and backward recursion relations (3.72) and (3.74), the cornerstone of the RGF algorithm, can be derived. Furthermore, we want to proof equation (3.75) for calculating off-diagonal elements. We will derive these recursion relations not only for the left connecting scheme but also derive the corresponding relations for the right connecting scheme. The following derivations are based on the notation and final equations of [23] and [35, chap. 4.3].

At first, we introduce the Dyson equations, which is the basis of RGF, and define the left- and right-connected matrices/inverses belonging to the left and right connecting scheme. With these definitions, we can proof the recursion relations in a very elegant way.

Dyson equation

The recursive Green function algorithm is based on dividing the matrix which we want to invert into smaller parts whose inverses are easily computed. The inverse of the whole system D is then obtained by the inverse of these unconnected parts d and the so called Dyson equations

$$D = d - dBD, \quad (\text{D.1})$$

$$D = d - DBd, \quad (\text{D.2})$$

where B connects the submatrices. In the following we want to proof these equations for a simple system. We consider the matrix A consisting of a diagonal part A_0 and an off-diagonal part B

$$A = \begin{pmatrix} A_1 & B_{1,2} \\ B_{2,1} & A_2 \end{pmatrix}, \quad A_0 = \begin{pmatrix} A_1 & 0 \\ 0 & A_2 \end{pmatrix}, \quad B = \begin{pmatrix} 0 & B_{1,2} \\ B_{2,1} & 0 \end{pmatrix}, \quad (\text{D.3})$$

where the entries A_1 , A_2 , $B_{1,2}$ and $B_{2,1}$ may be complex matrices itself. By the unconnected system we mean A_0 and by the connected system we mean the matrix A . Later we will illustrate how this approach can be interpreted in a physical context. We use the following

hold. And with the connection matrices $C^{L,i}$, $i \in \{1, \dots, N-1\}$, and $C^{R,i}$, $i \in \{2, \dots, N\}$, defined via

$$[C^{L,i}]_{j,k} := \delta_{j,i} \delta_{k,i+1} B_{i,i+1} + \delta_{j,i+1} \delta_{k,i} B_{i+1,i}, \quad (\text{D.10})$$

$$[C^{R,i}]_{j,k} := \delta_{j,i-1} \delta_{k,i} B_{i-1,i} + \delta_{j,i} \delta_{k,i-1} B_{i,i-1}, \quad (\text{D.11})$$

we can successively connect the diagonal elements/blocks from left or right via

$$A^{L,i+1} = A^{L,i} + C^{L,i} \quad \text{or} \quad A^{R,i-1} = A^{R,i} + C^{R,i}. \quad (\text{D.12})$$

We define the left- and right-connected inverses as the inverse of the left- and right-connected matrices

$$d^{L,i} := (A^{L,i})^{-1} \quad \text{and} \quad d^{R,i} := (A^{R,i})^{-1}, \quad (\text{D.13})$$

where $i \in \{1, \dots, N-1\}$ and $i \in \{2, \dots, N\}$. These inverse of these matrices fulfil the very useful relations

$$[d^{L,i}]_{j,k} = \delta_{j,k} (A_j)^{-1} \quad \text{for } j > i \text{ or } k > i, \quad (\text{D.14})$$

$$[d^{R,i}]_{j,k} = \delta_{j,k} (A_j)^{-1} \quad \text{for } j < i \text{ or } k < i, \quad (\text{D.15})$$

and for the special case $i = 1, N$

$$[d^{L,1}]_{j,k} = \delta_{j,k} (A_j)^{-1} = [d^{R,N}]_{j,k}. \quad (\text{D.16})$$

With the definition of left- and right-connected matrices and inverses, we can derive the forward and backward recursion in a very elegant way.

Forward recursion

We choose an arbitrary $i \in \{1, \dots, N-1\}$ and express $d^{L,i+1}$ in terms of $d^{L,i}$. This can be done by using the Dyson equations. From

$$d^{L,i+1} = (A^{L,i} + C^{L,i})^{-1} \quad (\text{D.17})$$

follows with equation (D.1)

$$d^{L,i+1} = d^{L,i} - d^{L,i} C^{L,i} d^{L,i+1}. \quad (\text{D.18})$$

Now we determine the element $(i+1, i+1)$ with (D.10) and (D.14), we obtain

$$[d^{L,i+1}]_{i+1,i+1} = [d^{L,i}]_{i+1,i+1} - [d^{L,i}]_{i+1,i+1} B_{i+1,i} [d^{L,i+1}]_{i,i+1}, \quad (\text{D.19})$$

and the element $(i, i+1)$ becomes

$$[d^{L,i+1}]_{i,i+1} = \underbrace{[d^{L,i}]_{i,i+1}}_{=0} - [d^{L,i}]_{i,i} B_{i,i+1} [d^{L,i+1}]_{i+1,i+1}. \quad (\text{D.20})$$

We insert the latter equation into (D.19) and rewrite the equation into the following form

$$[d^{L,i+1}]_{i+1,i+1} = \left[\underbrace{\left([d^{L,i}]_{i+1,i+1} \right)^{-1}}_{=A_{i+1,i+1}} - B_{i+1,i} [d^{L,i}]_{i,i} B_{i,i+1} \right]^{-1}. \quad (\text{D.21})$$

And with the abbreviation $[d^{L,i}]_{i,i} =: d_{i,i}^L$, we obtain the final form (3.72), here (D.22), of the forward recursion for the left connecting scheme

$$d_{i+1,i+1}^L = \left(A_{i+1,i+1} - B_{i+1,i} d_{i,i}^L B_{i,i+1} \right)^{-1} \quad \text{with} \quad d_{1,1}^L = (A_1)^{-1}. \quad (\text{D.22})$$

The last element of this recursion is special, because it's the (N, N) element/block of the connected inverse because $d_{N,N}^L = [d^{L,N}]_{N,N} = [A^{-1}]_{N,N}$.

The forward recursion relation for the right-connected inverses $d^{R,i}$ can analogously to (D.22) be derived, which becomes

$$d_{i,i}^R = \left(A_{i,i} - B_{i,i+1} d_{i+1,i+1}^R B_{i+1,i} \right)^{-1} \quad \text{with} \quad d_{N,N}^R = (A_N)^{-1}, \quad (\text{D.23})$$

where we defined $[d^{R,i}]_{i,i} =: d_{i,i}^R$. This recursion of the right connecting scheme starts at $i = N$ and ends for $i = 1$ with the $(1,1)$ element/block of the connected inverse $d_{1,1}^R = [A^{-1}]_{1,1}$.

Backward recursion

To proof the backward recursion relation (3.74), we choose an arbitrary $i \in \{1, \dots, N-1\}$ and express $D_{i,i}$ in terms of $D_{i+1,i+1}$ by using the Dyson equations. Our starting point is formula

$$D = d - dBd + dBDBd, \quad (\text{D.24})$$

which can be derived by inserting (D.1) into (D.2). We want to apply this formula to the identity

$$A = \left(A - C^{L,i+1} \right) + C^{L,i+1}, \quad (\text{D.25})$$

with $D = A^{-1}$, $B = C^{L,i+1}$ and $d = \left(A - C^{L,i+1} \right)^{-1}$. To get (D.25) for $i = N-1$ well-defined, we set $C^{L,N} := 0$. For evaluating (D.24), the following properties for the inverse of the unconnected system are very useful. First we can express d in terms of left- and right-connected inverses as follows

$$d = \left(A^{L,i} + A^{R,i+1} - A^{L,1} \right)^{-1} = d^{L,i} + d^{R,i+1} - d^{L,1} \quad (\text{D.26})$$

and with (D.14) and (D.16), we conclude that

$$[d]_{i,i} = [d^{L,i}]_{i,i} = d_{i,i}^L, \quad (\text{D.27})$$

$$[d]_{j,k} = 0 \quad \text{for} \quad j > i, \quad k \leq i \quad \text{or} \quad j \leq i, \quad k > i \quad (\text{D.28})$$

hold. Now we can calculate the element $D_{i,i}$ in equation (D.24) and obtain

$$D_{i,i} = [d^{L,i}]_{i,i} + [d^{L,i}]_{i,i} B_{i,i+1} D_{i+1,i+1} B_{i+1,i} [d^{L,i}]_{i,i}, \quad (\text{D.29})$$

which is equivalent to the desired backward recursion formula (3.74), here (D.30),

$$D_{i,i} = d_{i,i}^L + d_{i,i}^L B_{i,i+1} D_{i+1,i+1} B_{i+1,i} d_{i,i}^L \quad \text{with} \quad D_{N,N} = d^{L,N}. \quad (\text{D.30})$$

For deriving the backward recursion relation of the right connecting scheme, we apply equation (D.24) to

$$A = (A - C^{R,i}) + C^{R,i}, \quad (\text{D.31})$$

with $D = A^{-1}$, $B = C^{R,i}$ and $d = A - C^{R,i}$. For $d = d^{R,i} + d^{L,i} - d^{R,N}$ the relations

$$[d]_{i,i} = [d^{R,i}]_{i,i} = d_{i,i}^R \quad (\text{D.32})$$

$$[d]_{j,k} = 0 \quad \text{for} \quad j < i, \quad k \geq i \quad \text{or} \quad j \geq i, \quad k < i \quad (\text{D.33})$$

hold. And we can analogously to (D.29) derive the element (i, i) of the connected inverse, which becomes

$$D_{i,i} = d_{i,i}^R + d_{i,i}^R b_{i,i-1} B_{i,i-1} D_{i-1,i-1} B_{i-1,i} d_{i,i}^R \quad \text{with} \quad D_{1,1} = d^{R,1}. \quad (\text{D.34})$$

The backward recursion of the left/right connecting scheme calculates with the quantities $d_{i,i}^L/d_{i,i}^R$ derived from the forward recursion of the left/right connecting scheme the diagonal elements of a matrix inverse A^{-1} . For the computation of the diagonal elements the two different schemes are equivalent. This changes if we want to compute off-diagonal elements as we will see in the following.

Off-diagonal elements

The RGF algorithm can also be used to compute off-diagonal elements of an inverse. The required equations for the left connecting scheme can be derived as follows. We apply Dyson equation (D.1) to (D.25) with $i \in \{1, \dots, N-1\}$ arbitrary, and with (D.28) follows

$$D_{i,j} \Big|_{i < j} = -d_{i,i}^L B_{i,i+1} D_{i+1,j}. \quad (\text{D.35})$$

The same proceeding with Dyson equation (D.2) provides

$$D_{j,i} \Big|_{i < j} = -D_{j,i+1} B_{i+1,i} d_{i,i}^L. \quad (\text{D.36})$$

The corresponding relation for the right connecting scheme can be derived analogously. We apply (D.1) to the identity (D.31) and with (D.33) we obtain

$$D_{i,j} \Big|_{i > j} = -d_{i,i}^R B_{i,i-1} D_{i-1,j} \quad (\text{D.37})$$

The same proceeding with Dyson equation (D.2) provides

$$D_{j,i} \Big|_{i > j} = -D_{j,i-1} B_{i-1,i} d_{i,i}^R. \quad (\text{D.38})$$

With those equations and the forward recursion and parts of the backward recursion, we can compute every off-diagonal element of the inverse. Considering we want to calculate a single off-diagonal element $D_{i,j}$ of the inverse with $i < j$, we can apply equation (D.35) and (D.38) $(j-i)$ -times and obtain

$$D_{i,j} = (-1)^{j-i} \left(\prod_{k=i}^{j-1} B_{k,k+1} d_{k,k}^L \right) D_{j,j} \quad (\text{D.39})$$

for the left connecting scheme and

$$D_{i,j} = (-1)^{j-i} \left(\prod_{k=i+1}^j B_{k-1,k} d_{k,k}^R \right) D_{i,i}. \quad (\text{D.40})$$

for the right connecting scheme. In the other case, where $j < i$, we can apply equation (D.36) and (D.37) $(j-i)$ -times and obtain

$$D_{i,j} = (-1)^{i-j} \left(\prod_{k=j}^{i-1} B_{k+1,k} d_{k,k}^L \right) D_{i,i} \quad (\text{D.41})$$

for the left connecting scheme and

$$D_{i,j} = (-1)^{i-j} \left(\prod_{k=j+1}^i B_{k,k-1} d_{k,k}^R \right) D_{j,j}. \quad (\text{D.42})$$

for the right connecting scheme. And with (D.39) follows equation (3.77) with $i = 1$ and $j = N$. Whether the left or right connecting scheme is more efficient depends on the desired element of the inverse. Because with the right choice of the scheme the steps of the backward recursion can be minimized. For our application in section 3.3.2 this consideration is irrelevant because the Green function is symmetric. For computing several off-diagonal elements might the equations (D.39), (D.41) or (D.40), (D.42) be unwieldy and the specific way through the elements of the inverse with equations (D.35) - (D.38) must be adapted for the calculation.

Bibliography

- [1] S. Andergassen. *Functional Renormalization-Group Analysis of Luttinger Liquids with Impurities*. PhD thesis, University of Stuttgart, 2006.
- [2] S. Andergassen, T. Enss, C. Karrasch, and V. Meden. *Quantum Magnetism*, chapter A gentle introduction to the functional renormalization group: the Kondo effect in quantum dots. Springer, New York, 2008.
- [3] F. Bauer. 0.7 anomaly of quantum point contacts. treatment of interaction with functional renormalization group. Master's thesis, LMU Munich, 2008.
- [4] C. W. J. Beenakker and C. Schönberger. Quantum shot noise. *Physics Today*, 56:37–42, 2003.
- [5] Y. M. Blanter and M. Büttiker. Shot noise in mesoscopic conductors. *Physics Reports*, 336:1–166, 2000.
- [6] I. N. Bronstein and K. A. Semendjajew, editors. *Taschenbuch der Mathematik*. Deutsch, Thun, 5. edition, 2001.
- [7] H. Bruus and K. Flensberg. *Many-body quantum theory in condensed matter physics*. Oxford graduate texts. Oxford Univ. Press, Oxford, 2009.
- [8] B. R. Bulka, T. Kostyrko, M. Tolea, and I. V. Dinu. Correlated electrons and transport in a quantum point contact and in a double-quantum-dot system. *Journal of Physics: Condensed Matter*, 19:255211(16), 2007.
- [9] M. Büttiker. Quantized transmission of a saddle-point constriction. *Physical Review B*, 41(11):7906–7909, 1990.
- [10] S. M. Cronenwett, H. J. Lynch, D. Goldhaber-Gordon, L. P. Kouwenhoven, C. M. Marcus, K. Hirose, N. S. Wingreen, and V. Umansky. Low-temperature fate of the 0.7 structure in a point contact: A kondo-like correlated state in an open system. *Physical Review Letters*, 88(22):226805(4), 2002.
- [11] S. Datta. *Electronic transport in mesoscopic systems*. Number 3 in Cambridge studies in semiconductor physics and microelectronic engineering. Cambridge Univ. Press, Cambridge, 6. edition, 2005.

-
- [12] E. N. Economou. *Green's functions in quantum physics*. Number 7 in Springer series in solid-state sciences. Springer, Berlin, 1979.
- [13] T. Enss. *Renormalization, Conservation Laws and Transport in Correlated Electron Systems*. PhD thesis, Max Planck Institute for Solid State Research, 2005.
- [14] D. K. Ferry, S. M. Goodnick, and J. P. Bird. *Transport in nanostructures*. Cambridge Univ. Press, Cambridge, 2. edition, 2009.
- [15] A. Golub, T. Anono, and Y. Meir. Suppression of shot noise in quantum point contacts in the 0.7 regime. *Physical Review Letters*, 97(18):186801(4), 2006.
- [16] A. C. Graham, K. J. Thomas, M. Pepper, N. R. Cooper, M.Y. Simmons, and D. A. Ritchie. Interaction effects at crossings of spin-polarized one-dimensional subbands. *Physical Review Letters*, 91(13):136404(4), 2003.
- [17] J. Heyder. Der Übergang vom Kondoeffekt im Quantendot zur 0.7 Leitwert-Anomalie im Quantenpunktkontakt. Master's thesis, LMU Munich, 2009.
- [18] S. Hunklinger. *Festkörperphysik. Skript zur Vorlesung*. University of Heidelberg, 2002.
- [19] J. F. Janak. g factor of the two-dimensional interacting electron gas. *Physical Review*, 178(3):1416–1418, 1969.
- [20] C. Karrasch. Transport through correlated quantum dots. a functional renormalization group approach. Master's thesis, University of Göttingen, 2006.
- [21] A. Kirstensen, H. Bruus, A. E. Hansen, J. B. Jensen, P. E. Lindelof, C. J. Marckmann, J. Nygard, C. B. Sorensen, F. Beuscher, A. Forchel, and M. Michel. Bias and temperature dependence of the 0.7 conductance anomaly in quantum point contacts. *Physical Review B*, 62(16):10950–10957, 2000.
- [22] C. Kittel. *Einführung in die Festkörperphysik*. Oldenbourg, Munich, 13. edition, 2002.
- [23] G. Klimeck. Nanoelectronic modeling lecture 21: Recursive green function algorithm, 2010.
- [24] Y. Komijani, M. Csontos, I. Shorubalko, T. Ihn, K. Ensslin, Y. Meir, D. Reuter, and A. D. Wieck. Evidence for localization and 0.7 anomaly in hole quantum point contacts. *Europhysics Letters*, 91(6):67010(6), 2010.
- [25] E. J. Koop, A. I. Lerescu, J. Liu, B. J. van Wees, D. Reuter, A. D. Wieck, and C. H. van der Wal. The influence of device geometry on many-body effects in quantum point contacts: Signatures of the 0.7 anomaly, exchange and kondo. *Journal of Superconductivity and Novel Magnetism*, 20(6):433–441, 2007.

- [26] E. J. Koop, A. I. Lerescu, J. Liu, B. J. van Wees, D. Reuter, A. D. Wieck, and C. H. van der Wal. Persistence of the 0.7 anomaly of quantum point contacts in high magnetic fields. *ArXiv e-prints*, 2007.
- [27] S. Li, S. Ahmed, G. Klimeck, and E. Darve. Computing entries of the inverse of a sparse matrix using the FIND algorithm. *Journal of Computational Physics*, 227(22):9408–9427, 2008.
- [28] Song Li. *Fast Algorithms For Sparse Matrix Inverse Computations*. PhD thesis, Stanford University, 2009.
- [29] A. M. Lunde, A. D. Martino, A. Schulz, R. Egger, and K. Flensberg. Electronelectron interaction effects in quantum point contacts. *New Journal of Physics*, 11(2):023031, 2009.
- [30] K. A. Matveev. Conductance of a quantum wire in the wigner-crystal regime. *Physical Review Letters*, 92(10):106801(4), 2004.
- [31] M. J. McLennan, Y. Lee, and S. Datta. Voltage drop in mesoscopic systems: A numerical study using a quantum kinetic equation. *Physical Review B*, 43(17):13846–13880, 1991.
- [32] V. Meden. Funktionale renormierungsgruppe. Technical report, University of Göttingen, 2002.
- [33] Y. Meir. The theory of the "0.7 anomaly" in quantum point contacts. *Journal of Physics: Condensed Matter*, 20(16):164208(7), 2008.
- [34] Y. Meir, K. Hirose, and N. S. Wingreen. Kondo model for the 0.7 anomaly in transport through a quantum point contact. *Physical Review Letters*, 89(19):196802(4), 2002.
- [35] G. Metalidis. *Electronic Transport in Mesoscopic System*. PhD thesis, University of Halle-Wittenberg, 2007.
- [36] J. R. Minkel. A mesoscopic mystery. *Physical Review Focus*, 10(24), 2002.
- [37] T. R. Morris. The exact renormalization group and approximate solutions. *International Journal of Modern Physics A*, 9:2411–2450, 1994.
- [38] Y. V. Nazarov and Y. M. Blanter. *Quantum transport*. Cambridge Univ. Press, Cambridge, 2009.
- [39] J. W. Negele. *Quantum many-particle systems*. Advanced Book Classics. Perseus Books, Reading, MA, 1998.

- [40] I. Pallecchi, Ch. Heyn, J. Lohse, B. Kramer, and W. Hansen. Magnetocapacitance of quantum wires: Effect of confining potential on one-dimensional subbands and suppression of exchange enhanced g factor. *Physical Review B*, 65(12):125303(8), 2002.
- [41] N. K. Patel, J. T. Nicholls, L. Martin-Moreno, M. Pepper, J. E. F. Frost, D. A. Ritchie, and G. A. C. Jones. Evolution of half plateaus as a function of electric field in a ballistic quasi-one-dimensional constriction. *Physical Review B*, 44(24):13549–13555, 1991.
- [42] W. H. Press, S. A. Teukolsky, W. T. Vetterling, and B. P. Flannery. *Numerical recipes*. Cambridge Univ. Press, Cambridge, 3. edition, 2007.
- [43] D. J. Reilly. Phenomenological model for the 0.7 conductance feature in quantum wires. *Physical Review B*, 72(3):033309, 2005.
- [44] D. J. Reilly, T. M. Buehler, J. L. O'Brien, A. R. Hamilton, A. S. Dzurak, R. G. Clark, B. E. Kane, L. N. Pfeiffer, and K.W. West. Density-dependent spin polarization in ultra-low-disorder quantum wires. *Physical Review Letters*, 89(24):246801, 2002.
- [45] T. Rejec and Y. Meir. Magnetic impurity formation in quantum point contacts. *Nature*, 442:900–903, 2006.
- [46] G. Seelig and K. A. Matveev. Electron-phonon scattering in quantum point contacts. *Physical Review Letters*, 90(17):176804(4), 2002.
- [47] A. Svinzhenko, M. P. Anantram, T. R. Govindan, B. Biegel, and R. Venungopal. Two dimensional quantum mechanical modeling of nanotransistors. *Journal of Applied Physics*, 91(4):2343–2354, 2002.
- [48] K. J. Thomas, J. T. Nicholls, N. J. Appleyard, M. Y. Simmons, M. Pepper, D. R. Mace, W. R. Tribe, and D. A. Ritchie. Interaction effects in a one-dimensional constriction. *Physical Review B*, 58(8):4846–4852, 1998.
- [49] K. J. Thomas, J. T. Nicholls, M. Y. Simmons, M. Pepper, D. R. Mace, and D. A. Ritchie. Possible spin polarization in a one-dimensional electron gas. *Physical Review Letters*, 77(1):135–138, 1996.
- [50] S. Timmann. *Repetitorium der Funktionentheorie*. Binomi, Springe, 2003.
- [51] W. G. van der Wiel, S. De Franceschi, T. Fujisawa, J. M. Elzerman, S. Tarucha, and L. P. Kouwenhoven. The kondo effect in the unitary limit. *Science*, 289(5487):2105–2108, 2002.
- [52] H. van Houten and C. W. J. Beenakker. Quantum point contacts. *Physics today*, 49(7):22–27, 1996.

-
- [53] B. J. van Wees, H. van Houten, C. W. J. Beenakker, J. G. Williamson, L. P. Kouwenhoven, D. van der Marel, and C. T. Foxon. Quantized conduction of point contacts in a two-dimensional electron gas. *Physical Review Letters*, 60(9):848–850, 1988.
- [54] D. A. Wharam, T. J. Thornton, R. Newbury, M. Pepper, H. Ahmed, J. E. F. Frost, D. G. Hasko, D. C. Peacock, D. A. Ritchie, and G. A. C. Jones. One-dimensional transport and the quantisation of the ballistic resistance. *Journal of Physics C (Solid State Physics)*, 21(8):L209–14, 1988.

Acknowledgements

Last but not least, I would like to thank all the people who made this thesis possible.

Prof. Dr. Jan von Delft for giving me the opportunity to work in his group and for his support and advice. Florian Bauer, who had always an open door for me and my various questions. I learned a lot from him. Furthermore, he left his fRG program to me, which was a great starting point. Jan Heyder for helping me with my various computer problems and for explaining their previous and proceeding work to me. All the members of the Chair for Theoretical Condensed Matter Physics who made a nurturing and pleasant work environment possible.

My girlfriend Stephanie who was very helpful and understanding during this year. My parents Ingeborg and Heinz Ufer and my siblings for their financial and emotional support.

Statement of authorship

This thesis is the result of my own work. It contains nothing which is the outcome of work done in collaboration, except where stated. Reference is made throughout the text to the sources which I have availed myself of the work of others.

Mit der Abgabe der Diplomarbeit versichere ich, dass ich die Arbeit selbständig verfasst und keine anderen als die angegebenen Quellen und Hilfsmittel benutzt habe.

Munich, May 16, 2011